Nonlinear diffusion-limited two-dimensional colliding-plume simulations with very high-order numerical approximations

Article

Accepted Version

Straka, J. M. ORCID: https://orcid.org/0000-0003-3672-5858, Williams, P. D. ORCID: https://orcid.org/0000-0002-9713-9820 and Kanak, K. M. ORCID: https://orcid.org/0000-0003-3479-9669 (2024) Nonlinear diffusion-limited two-dimensional colliding-plume simulations with very high-order numerical approximations. Quarterly Journal of the Royal Meteorological Society, 150 (759). pp. 663-705. ISSN 1477-870X doi: 10.1002/qj.4616 Available at https://centaur.reading.ac.uk/114145/

www.reading.ac.uk/centaur

CentAUR

Central Archive at the University of Reading

Reading's research outputs online

Straka Jerry M (Orcid ID: 0000-0003-3672-5858)
Williams Paul D. (Orcid ID: 0000-0002-9713-9820)
Kanak Katharine M. (Orcid ID: 0000-0003-3479-9669)

Nonlinear diffusion-limited 2D colliding plume simulations

with very high order numerical approximations

Jerry M. Straka
Norman, Oklahoma, USA
ORCID: https://orcid.org/0000-0003–3672-5858

Paul D. Williams
Department of Meteorology, University of Reading
Reading, UK
ORCID: https://orcid.org/0000-0002-9713-9820

Katharine M. Kanak
Norman, Oklahoma, USA
ORCID: https://orcid.org/0000-0003–3479-9669

REVISED

Quarterly Journal of the Royal Meteorological Society

16 September 2023

Corresponding Author:
Jerry M. Straka
Norman, Oklahoma, USA 73072
Phone; 405-664–3907
email: jerrystraka@gmail.com
Prof. Emeritus School of Meteorology
University of Oklahoma, Norman, Oklahoma 73072

ABSTRACT

Atmospheric numerical models play a crucial role in operational weather forecasting, as well as improving our understanding of atmospheric dynamics via research studies. Maximising their accuracy is of paramount importance. Use of >O7 flux schemes in atmospheric models is largely undocumented, with no studies considering O3–17 fluxes with formal accuracy-preserving high order interpolation, pressure gradient / divergence, and subgrid-scale (SGS) turbulent fluxes. Higher order numerical approximations can reduce truncation, amplitude and phase errors, and potentially improve model accuracy and effective resolution.

Here, simulations are presented using very high order O3–17 fluxes, with / without high order O2–18 Lagrangian interpolations, pressure gradient / divergence approximations, and SGS turbulent fluxes for a 2D, highly-viscous (Re~100) diffusion-limited, nonlinear colliding plumes problem using 25–200 m spatial resolutions. The highest order flux schemes coupled with higher order interpolations, pressure gradient / divergence and SGS flux approximations produced the best solutions, with higher-order fluxes and interpolations being most important. Overall solution convergence of ~O1–2 with mode-split (fast sound / slow advective waves) O3 Runge-Kutta temporal schemes was negatively impacted by ≤O1 temporal convergence with SGS fluxes, divergence damping, and especially spatial filters, compared to ~O3 convergence with these inactivated.

While very high order schemes were shown to improve solution accuracy, few cost-effective higher order highly-viscous test problem solutions (higher order versus finer resolution) were found using theoretical floating-point operations (FPO) with CFL-limited or constant stable Courant number-based time steps. However, employing CPU time, rather than FPOs, demonstrated there was reduced computational burden using higher order approximations. We conclude that O9–17 flux schemes with or without high-order ≥O4 interpolations, pressure gradient / divergence approximations, and SGS fluxes can improve atmospheric model solution accuracy, without prohibitive computation costs, compared to O3–7 flux with O2 interpolations, pressure gradient / divergence approximations, and SGS fluxes.

1 | INTRODUCTION

An important aspect of developing numerical models of physical phenomena in the atmosphere, ocean, or any fluid is to improve numerical accuracy of solutions and better simulate important features that are marginally resolved in space and/or time. This can be achieved, at least in part, by developing and using more accurate physical representations, finer grid resolution and/or more accurate numerical techniques. High order numerical approximations can increase accuracy and effective resolution for complex fluid flows with multiple sharp gradients, although if care is not taken, such techniques can sometimes be detrimental to solution accuracy. One of the greatest foci concerning numerical techniques in the reviewed literature, has been on improving the accuracy of advection / flux terms by employing schemes with higher order approximations (high order is defined as ≥O3 according to Wang et al. 2013), along with improving their conservation and monotonic properties. One driving motivation for more accurate advection schemes is that higher order numerical approximations are often more cost effective in producing accurate solutions compared to lower order numerical approximations with comparable and/or finer resolution (e.g., Kreiss and Oliger 1972; Haltiner and Williams 1980; Jameson 2000; Shi et al. 2003 SZS03; Latini et al. 2007). While higher order numerical approximations generally can improve solutions for complex nonlinear fluid flows, they might not be needed as much (or improvements are not as readily seen) for some very smooth, more linear flows.

In contrast to the significant efforts to improve advection approximations, little effort in the atmospheric sciences has been made (at least in the reviewed literature) to examine the effect of high order accurate pressure-gradient-acceleration approximations in the velocity equations and high order divergence approximations in the pressure equation (e.g., Straka and Anderson 1993; Klemp 2007 in the atmospheric sciences; and Desjardins et al. 2008 and numerous others in other areas of fluid flows). Additionally, high order approximations for the mass divergence term, which is subtracted from the flux divergence to obtain the advection term to improve mass and energy conservation [e.g., Tripoli and Cotton 1980 (CSU-RAMS model) and Bryan 2021 (CM1 model)] is not traditionally computed with velocities and density with high order interpolation. Higher order approximations also can be made for the advection velocities in the velocity equation on a staggered grid (Pressel et al. 2015) and all variables for unstaggered grids. Likewise, there has been little effort to examine the impact of higher order interpolations (besides in the computation

of fluxes in the advection term) for state and other quantities not available at necessary locations (e.g., density at velocity points, buoyancy in the equation for vertical motion, etc., on a staggered grid), which occurs with staggered, unstaggered, and unstructured grids.

Finally, the authors know of only a few attempts to use high order approximations for subgrid-scale (SGS) turbulent flux parameterizations in atmospheric models. For example, Anderson (1989) and Straka and Anderson (1993) used constant eddy mixing coefficients and Pressel et al. (2015) used turbulence kinetic energy-based eddy mixing coefficients. A few examples in other fluid flow studies include those by Zhang et al. 2003, SZS03, Desjardins et al. (2008), Sari et al. (2010), and Shen and Zha (2010). Given the generally diffusive nature of turbulence, the impact of the high order approximations SGS turbulent fluxes could be minimised and errors with these approximations could be damped more than errors with advective approximations (e.g., personal communication B. Fornberg). However, SGS turbulent flux closures that permit nonlinear kinetic energy backscatter (e.g., Kosović 1997 and Mirocha et al 2010; backscatter causes an upscale transfer of unresolved kinetic energy to resolved-scale kinetic energy) may not have damped numerical approximation errors at small scales.

The lowest order of accuracy for any numerical approximation used in a model limits the model's overall formal accuracy. For example, use of an O6 advection scheme that requires some information that is computed with an O2 approximation is limited to O2 overall accuracy. Kalnay and Hoitsma (1979), Purser and Leslie (1988; PL88), Xue and Lin (2001), and others discussed the loss of any improved accuracy using fourth order advection on staggered grids by putting them on unstaggered grids by the use of midpoint interpolation (averaging) of gradient and fluxes to grid points where they are needed. Additionally, many researchers use implicit solvers for the vertical pressure gradient and vertical component of divergence associated with fast modes (e.g., sound waves) using O2 spatial differencing for efficiency and O1 or O2 (e.g., Crank-Nicholson) temporal accuracy.

The behaviours of advection schemes have been thoroughly discussed in the literature for O1–7, with a few up to O17, for many linear and some nonlinear problems (e.g., Crowley 1968; O4 Gerrity 1976; O4 Klemp and Wilhelmson 1978; O6 Kaplan et al. 1982; O3 Schlesinger 1985; O4

Gadd 1980; O2–10 Tremback et al. 1987 T87; O2–06 PL88; O2–10 Anderson 1989; O1–9 Leonard 1991; O2–6 Tripoli 1992; O2–10 Straka et al. 1993 S93; O2–10 Straka and Anderson 1993; ≤O8 Costa and Sampio 1997; O3–11 Shu 1997; O3–11 Balsara and Shu 2000 BS00; O4 Xue and Lin 2001, O4–6 Wicker and Skamarock 2002 WS02; O3–9 Shu 2003 S03; O5 and O9 SZS03; O7 Kusaka et al. 2005; O3–9 Latini et al. 2007; O5–17 Gerolymos et al. 2009 G09; O4–11 Pressel et al. 2015 P15; O3–9 Norman 2021 N21; 05–17 Wu et al. 2021 W21; O2–10 Williams et al. 2022 WSK22; etc.). Only a few studies have examined the use of >O9 schemes, with results including improvement from O5–17 by both G09 and W21 for a number of linear and nonlinear problems, and improved results by using O5 and O11 weighted essentially non-oscillatory (WENO) compared to O4 and O6 constant grid flux by P15 for both the S93 2D density current problem and the Brian and Fritsch (2002; BF02) saturated 2D plume problem, although P15 did not compare their O11 WENO solutions with >O6 odd order, high order constant grid flux solutions.

Importantly, the highest order of accuracy for advection / flux reported for many atmospheric models is O3–7 approximations for horizontal advection / flux, sometimes without an increase in the order of accuracy for vertical advection / flux (presumably the vertical resolution is finer than in the horizontal). Also, very few, if any, use higher order interpolations, and/or pressure gradient / divergence approximations (exceptions are PL88 and Kaplan et al. 1982). Interpolation accuracy that does not match advection order can lead to errors in overall accuracy and convergence rates (e.g., Kalnay and Hoitsma 1979; PL88; Xue and Lin 2001; Desjardins et al. 2008; WSK22; etc.). High order interpolation for necessary off-grid point information was recently demonstrated to be essential for attaining theoretical convergence rates by WSK22 in simulations of the 2D linear rotating cone problem, although they did not look at this for the nonlinear problems they included in their study. However, Desjardins et al. (2008) examined the importance of high order interpolation for nonlinear Rayleigh-Taylor instability simulations. Virtually all atmospheric models known to the authors use O2 numerical approximations for pressure gradient acceleration in the velocity equations and divergence in pressure equations except for Klemp et al. (2003), who showed that higher order pressure gradient terms and grid staggering for higher order advection and metric terms for sloping surfaces in mountain wave simulations did not always produce better

solutions. Additionally, almost all atmospheric models use second order numerical approximations for SGS turbulent flux parameterizations.

Even though solutions may look rather similar, visual similarity does not guarantee that mass and energy conservation are better preserved, or measures associated with mean and fluctuations of velocities in large eddy simulation are better represented, when comparing lower versus higher numerical temporal or spatial accuracy or finer versus coarser resolution for advective and SGS-scale turbulent fluxes, pressure gradients, and interpolations (e.g., Desjardins et al. 2008). Moreover, simplifications to the Navier-Stokes equations may result in very similar looking solutions, compared to more complete equations sets for shorter integrations, while having significant mass and energy conservation errors (e.g., Bryan and Fritsch 2002).

Solutions with higher order temporal or spatial accuracy or those with finer spatial resolution may look similar visually to those with less accuracy or spatial resolution, but this does not guarantee better mass or energy conservation (e.g., Desjardins et al. 2008) or more accurate large eddy simulation statistics (mean and fluctuation velocity measures). Moreover, solutions using forms of the Navier-Stokes equations with simplifications may also look visually similar to those without such simplifications for shorter integrations, while having significant mass and energy conservation errors (e.g., Bryan and Fritsch 2002).

Higher order schemes can sometimes cause undesirable effects. For example, in trying to preserve relationships of tracers; two or more passive tracers generally will not be advected individually as accurately compared to advection of their sum in the absence of interactions (e.g., cloud aerosol number concentration maybe be reduced from sticking upon collision; Pardo et al. 2022). In this case, Pardo et al. (2002) recommended corrective normalisation procedures with high order schemes (Ovtchinniov and Easter 2009) with acceptable results. Pardo et al. also comment that smoothing from diffusiveness with lower order advection can generate other undesirable side-effects, especially when the tracers are physically-dynamically relevant (e.g., with cloud microphysics variables). Additionally, as summarised by Wu et al. (2021), high order schemes a) require a more restrictive CFL for stability, b) tend to produce weaker dissipation, that can damp

numerical errors, c) may lose accuracy when long stencils include two or more marginally resolved waves or gradients, and d) can be subject to well-known Runge phenomena with Lagrangian-based interpolation / reconstruction polynomials, including those in flux calculations. Durran (2010) commented that high order Lagrangian-based schemes (up to O16) have smaller weight solutions at remote stencil locations than comparable remote locations for 17-point spectral method schemes, based on results from Merilees and Orzag (1979), and noted that larger weights at remote grid locations in spectral schemes might be of concern for linear problems, but did not seem to be problematic for more practical problems. If significant remote location influence is not much of a practical issue for spectral method schemes (Durran 2010) with nonlinear problems, it seems plausible that excessive influence and resulting problems from remote stencil locations for long stencil finite difference schemes, as described by point c), might be less for high order Lagrangian schemes than with spectral methods.

As SZS03 astutely state, *"a natural question is whether it is worthwhile to use such high order methods."* They also note that in many situations, the cost-effectiveness of high order methods depends on whether the problem is complex enough, with perhaps multiple sharp gradients, to warrant higher order numerical approximations. For example, some studies (e.g., T87) have suggested that O6 flux / advection is a good compromise between accuracy and computational cost based on a 2D linear cone advection problem and a 2D cone in a constant-in-time deformation flow problem. Norman (2021), however, states, in the context of atmospheric science related problems, *"why one should bother with higher order accuracy… is that even though high order convergence is not observed, the constant on the error term still goes down with higher order accuracy, particularly if suitable limiting is used."* These statements made by SZS03 and N21 are relevant to the current study, as dependent variable fields can be either weakly or highly complex and linear or nonlinear in different regions of the solutions.

The following four points related to high order numerical approximations motivate this study. First, the widespread use of spectral and pseudo-spectral methods for advection are evidence of considerable use of highly accurate schemes in the atmospheric sciences, especially but not exclusively in global weather prediction and research models. Boyd (1994, 2001) and Fornberg (1996) have gone to great lengths to promote the high accuracy of pseudo-spectral approaches. As

noted by Boyd (1994), "Fornberg [1975; 1987; 1990] has shown that the limit of high order finite differences is the pseudo-spectral method…" The high degree of success of spectral, pseudo-spectral, and other schemes such as high order local spectral advection (Anderson 1989; Straka and Anderson 1993), all of which are very accurate for linear and nonlinear problems, supports further investigation of the impact of >O7 advection accuracy in atmospheric models.

Second, it is well known (e.g., Haltiner and Williams 1980) that higher order advection numerical approximations can provide more accurate solutions for a given grid than a lower order solution with finer resolution for many simple linear problems. The computational physics community, among others, also has shown repeatedly (e.g., PL88; BS00; S03; SZS03; Latini 2007; G09; P15; etc.) that complex gas dynamics simulations, large-eddy simulations, and others, often can be made more accurate by improving the resolution or the numerical approximations beyond O3, often above O9, and as high as O17, or both resolution and numerical approximations, with increasing order of accuracy often being more computationally efficient for comparable solutions compared to low order solutions with finer grid resolution.

Third, different very high order finite-difference schemes, including those often used for high order numerical approximations (e.g., WENO, Crowley, traditional finite difference) with various orders, need to be objectively compared for multi-dimensional, nonlinear atmospheric flow problems. Very few studies in the atmospheric sciences have done this for >O7 numerical approximations. Furthermore, the impacts of very high order advection / flux numerical approximations, especially when combined with comparable order interpolations (e.g., Kalnay and Hoitsma 1979 or PL88), pressure gradient / divergence (e.g., PL88 and Klemp et al. 2003) in simulating complex kinematical aspects (vorticity, deformation, divergence, and translation), and SGS turbulent fluxes are rarely if ever considered for evolving multidimensional nonlinear atmospheric flows. The degree to which the use of higher order schemes can a) most importantly, produce better solutions, and b) be computationally less expensive / more cost effective needs to be further explored. Additionally, which higher order approximations achieve the most economically accurate solutions should be better established.

Fourth, many studies of very high order advection in gas dynamics for non-viscous or very weakly viscous flows (in a physical sense as well as numerical), often with multiple shocks, demonstrate very convincing results. However, very few of these studies attempted to make objective error measure estimates as they are difficult to interpret. Significantly fewer studies of very high order advection make use of diffusion-limited problems that incorporate a sufficiently large constant eddy mixing coefficient in the SGS turbulence closure, as in S93 or Zhang et al. (2003), in order to reasonably provide a nearly grid converged solution, which makes both visual and objective error measure comparisons possible. A rigorous determination of whether results based on the use of very high order advection are as convincing for viscous flows, as they have been shown to be for non-viscous or very weakly viscous flows, has not been well documented.

These points help motivate the demonstration in this paper of the accuracy improvement possible in numerical simulation solutions by using very high order (O9–17) upwind-biased spatial numerical flux approximations, above those traditionally used (O3–7). The impact of many other advection and flux schemes such as WENO, Crowley, compact, flux-corrected transport, finite-element, finite volume, piecewise parabolic schemes, etc., is not explored in this paper. Simulations are presented for high and very high order upwind-biased advective-flux schemes coupled with comparably high order (next higher even order) spatial filters, Lagrangian interpolations / reconstructions, and staggered-grid finite differences for pressure gradient accelerations in the velocity equations, and divergence in the pressure equation. The importance of the use of higher order interpolations and pressure gradient / divergence approximations is evaluated by comparison with solutions using O2–18 approximations for these terms. In addition, the use of high order SGS turbulent flux approximations is also evaluated and discussed. Objective error measures based on an approximately grid converged solution are used to help evaluate the test solutions. A summary of the model is presented in section 2. Results and discussion for both a simple, idealized example using an analytical function for flux, interpolations, and pressure gradient accelerations, as well as for 2D nonlinear, diffusion-limited, atmospheric simulations are presented in section 3, followed by conclusions in section 4.

2 | MODEL

The 3D model used in this study integrates the flux form of the fully compressible Navier-Stokes equations, which are cast on a Cartesian staggered Arakawa C-grid (Arakawa and Lamb, 1977) with 3D stretched grids and terrain options. The model is based on equations for the three components of velocity u_i (m s^{-1}), potential temperature (K), moisture and microphysical variables such as vapour, cloud, rain, snow, graupel, etc., turbulence kinetic energy (TKE or E; m^2 s^{-2}; or square root of turbulence kinetic energy m s^{-1} used by Deardorff 1980), density (kg m^{-3}), perturbation pressure p' (kg m^{-1} s^{-2}; or non-dimensional Exner function as is used in this study), and any number of additional scalar fields. The simulations in this study are dry with no other scalars than potential temperature and no passive scalar tracers. The equations are cast in a flux-conservative form that numerically improves conservation of mass and energy and can be used for dry or moist dynamics (Klemp and Wilhelmson 1978; Tripoli and Cotton 1980; Bryan and Fritsch 2002 BF02; Cotton et al. 2011; Morrison and Bryan 2012; and Bryan 2021 B21).

With a fast/slow mode-split system of equations (Skamarock and Klemp 1992), the slow modes (advection, turbulence, etc.) are integrated with a forward-in-time O3 (O2 for nonlinear problems; Baldauf 2010), three-stage Runge-Kutta scheme (RK3; WS02) and fast modes are integrated with the O2 in time forward-backward scheme (e.g., Mesinger 1977). Divergence damping (Skamarock and Klemp 1992) is used to help keep mode-split solutions stable, and is computed with O1 temporal and O2 spatial numerical approximations on the fast (sound) mode time step. Errors introduced by the low order of accuracy for divergence damping are kept at bare minimum by using a very small divergence damping coefficient as use of more traditional values can adversely impact solution accuracy for higher order solutions (Lian et al. 2022), as was seen in the course of this study. Values of the divergence damping coefficient up to 20 times more than the very small value used in this study had almost no impact on the behaviours of the solutions in this study.

The model dynamics and physics activated for the simulations in this study included advection, pressure gradient, divergence, buoyancy, and constant eddy mixing coefficient SGS turbulence. Schemes were constructed for low and high order (O1/2–17/18, and higher) flux and SGS turbulent flux computations using "constant grid" based coefficients (T87) for these flux interpolation (first derivative) calculations. These coefficients were produced so that they have the same order of error as pure advective (diffusion) schemes when the advective velocity (mixing coefficient), grid

increment, and density (when it is incorporated in fluxes) are constant (explained in T87 and Supporting Information S2a). In contrast, integrated flux versions based on differences of traditional Lagrangian interpolation flux values (explained in T87 and Supporting Information S2a), for either unstretched or stretched / irregular grids, while high order in terms of grid stencil points used, are not exactly equivalent to pure advective schemes when the advective velocity and grid increment are constant (T87), with accuracy limited even though the interpolation polynomials and first derivative are high order. In other words, the flux difference of the interpolated flux values at locations i+1/2 and i−1/2 results in reduced accuracy as the integrated flux and first derivative coefficients are found from a polynomial of one point less than the advective and diffusion forms. For the cases of <O3 accuracy, both integrated and constant grid flux coefficients are the same for the advective and diffusion related fluxes. Interestingly, some (e.g., Crowley 1968; Bott 1989) have used and continue to use the integrated flux form. As discussed later, it appears that advective fluxes are sensitive to the form used, but not the SGS-turbulent fluxes.

Values for CFL based on linear stability criteria for RK3 time integration with odd order one point upwind-biased advective fluxes are generated following methods by Baldauf (2008) and are given by CFL (O1–19) = 1.256373, 1.625891, 1.434983, 1.243779, 1.127174, 1.049315, 0.9935351, 0.9514629, 0.9184809, 0.8918446. Values generated for RK3 time integration with even order SGS turbulent fluxes are given by CFL (O2–20) = 0.6281864, 0.4711398, 0.4157116, 0.3864818, 0.3680779, 0.3552619, 0.3457371, 0.3383294. 0.3323715, 0.3274550. In contrast, the Euler forward linear stability criteria for even order SGS turbulent fluxes are smaller, and are given by CFL (O2–20) = 0.5, 0.375, 0.3308827, 0.3076172, 0.2929688, 0.2827679, 0.2751868, 0.2692906, 0.2645485, 0.2606353.

High order O2–18 pressure gradient and divergence terms were calculated using staggered grid stencils and coefficients from PL88 and Fornberg (1988), while spatial filters use 3–19 points in each direction, and the latter are denoted hereafter simply as O2–18 spatial filtering (PL88). Importantly, an Nth even order filter does not imply Nth order accurate, rather Nth order here implies O2 numerical approximations for the Nth even order derivatives (Fornberg 1988). An N_Ath order accurate N_Dth order even derivative filter would require (N_D + N_A −1) stencil points to

compute, thus, for example, an O10 accurate O10 derivative based filter would require 19 grid points versus 9 grid points for an O2 accurate O10 derivative. The divergence damping is computed with O2 staggered grid spatial differencing, although it can be made any order using any even order staggered grid scheme. For example, a higher order divergence damping scheme can be obtained by using very high order staggered grid differencing for divergence and then computing the differences of these values of divergence with the high order staggered grid coefficients, which was considered, but was not used, as the impact with a very small divergence damping coefficient was miniscule (e.g., differences were in the fifth or sixth digit for vertical velocity). Finally, turbulence and spatial filtering are often employed with forward or backward time differencing using temporal order of accuracy of O1 on the last stage of RK3 (e.g., WS02). In this study, O2 temporal accuracy is maintained for nonlinear RK3 time integrations by updating these tendencies on each of the three RK3 stages. The subgrid-stress terms in the momentum equations and turbulent fluxes for the potential temperature equation and other scalar equations generally follow those given by Deardorff (1980), P15, Cotton et al. (2011), and B21. Slight differences in the theoretical formulation of these subgrid-stress terms times density in the momentum equations [e.g., $\tau_{ij} = -\rho\, 2\, K_m\, d_{ij} + \rho\, 2/3\, \delta_{ij}\, E$ in, e.g., Deardorff (1980), Wyngaard (2004), and Cotton et al. (2011), and herein, where the second term is required for consistency, or $\tau_{ij} = -2\, \rho\, K_m\, d_{ij}$ in, e.g., P15 or B21, with the second term for τ_{ij} dropped as $\partial u_k / \partial x_k = 0$ in approximations for some scales (e.g., mesoscale, Mirocha et al. 2010) results in relative differences of up to $<1 \times 10^{-4}\,\%$ for maximums and minimums of the velocity components, and even smaller differences in root mean square (RMS) errors against a reference simulation, for the test problem used in this study when K_m is either a function of E or a specified constant. Use of a constant K_m effectively eliminates the dependence of τ_{ii} on the second term, except for the effect of density, as E is constant and its difference in x_i is zero. Tests with these different SGS closure formulations (not shown) resulted in the same conclusions based on objective errors and visual behaviour of the solutions. Further discussion is beyond the scope of this study.

An abbreviated summary of the dynamics, physics, and numerical approximations used in the model is provided in Supporting Information Table S1, as are the equations solved for the basic dynamic core, (additional details and codes available from the authors). All high order numerical

approximation coefficients used in this paper are provided in Supporting Information Tables S2a–d, including notes on how coefficients can be calculated.

Results for O1, O7, O11, O15, and O19 flux solutions were not shown to save space. All of these orders of fluxes are used in the telescoping stencils near the vertical boundaries. All solutions were made with 64-bit mathematics and storage as round-off errors can limit solution improvement for schemes with ~ >O17 numerical approximations. Hardware for 128-bit arithmetic is not available on most computers, but is available for some compilers at the software level; however, it is excessively computationally expensive. Additionally, as 128-bit memory is not available on most computers that use the latest Intel or GNU FORTRAN compilers that were freely available in the year 2022, all solutions in this study are made with 64-bit mathematics and storage and are comparable with those made with 32-bit mathematics and storage. Solutions herein were produced using code compiled with the Intel compiler.

3 | RESULTS AND DISCUSSION

3.1 | Idealised one-dimensional accelerations

First, before examining the nonlinear test solutions, continuous 1D analytical functions of an arbitrary coordinate, z, and their derivatives are used to compare various order difference forms of the pressure gradient acceleration (mid-point) and interpolations (mid-point) assuming constant Δz. The root mean square (RMS) error (Conte and de Boor 1980), a commonly used 'bulk' objective error measure in numerical analysis, is used to demonstrate the accuracy of the difference forms of an analytical function using three gradients and three resolutions. The function provides representative approximations of some of the relevant features in simulations used in this study. While the exercise is trivial, the results support the use of higher order numerical schemes at least for linear problems, and provide a performance basis for high order schemes for a simple test problem from which complexity can be added. Furthermore, only evaluation of the spatial differencing is considered to avoid time-differencing errors.

A perturbation pressure function is given by

$$p(i) = P_o [1 - cos^n (\pi z / L_z)]$$

and its analytical spatial derivative (pressure gradient acceleration *PGA*) is given by

$$1/\rho \; dp(i)/dz = PGA(i) = (1/\rho) \; (\pi \, / \, L_z) \; (P_o \; n) \; [cos^{(n-1)} \; (\pi \, z \, / \, L_z)] \; sin \; (\pi \, z \, / \, L_z),$$

where the index *i* is a grid location in *z* defined by $z(i) = i \, \Delta z$, $P_o = 100$ kg m^{-1} s^{-2} (Pa), $\rho = 1$ kg m^{-3}; $\Delta z = 25$, 50, and 100 m and wavelength $L_z = 600$ and 1200 m or wavenumber $k_z = 4$ and 2, respectively. Similarly, a buoyancy function (*b*) is defined, as buoyancy is defined at the mass grid points and needs to be interpolated to the vertical wind locations for the staggered C-grid, and it is also used to examine flux divergence of buoyancy (*BFLX*), where *b(i)* is given by

$$b(i) = B_o \; [1 - cos^n \; (\pi \, z \, / \, L_z)],$$

where $B_o = 0.1$ m s^{-2}, which is roughly $g \; (\theta - \theta_o)/\theta_o \sim 10$ m s^{-2} • 3K / 300 K for gravity $g = 9.81$ m s^{-2} and $L_z = 600$ and 1200 m, or $k_z = 4$ and 2, respectively. The analytical solution for linear flux divergence of buoyancy *BFLX* (the difference of the fluxes) is the same as linear advection assuming constant velocity and nondivergent flow, and is given by

$$-w \; db(i)/dz = -d(wb)/dz + b \; dw/dz = BFLX(i)$$
$$= -w \; (\pi \, / \, L_z) \; (B_o \; n) \; [cos^{(n-1)} \; (\pi \, z \, / \, L_z)] \; sin \; (\pi \, z \, / \, L_z),$$

where $w = 10$ m s^{-1} is the constant advection velocity, and $b \; dw/dz = 0$.

The values for *p(z)* and 100 • *PGA(z)* are plotted in Fig. 1a (*PGA* is multiplied by 100 for plotting), while those for *b(i)* and 10 • *BFLX(z)* are shown in Fig. 1b (*BFLX* is multiplied by 10 for plotting). The width of the O18 stencils for pressure gradient acceleration, and interpolation examples, and O17 for flux examples, using 25, 50, 100 m grid resolutions are also provided in Figs. 1a–b, respectively. The calculated convergence rates are provided in Supporting Information Tables S3a–b.

As expected, the use of increasingly high order approximations improved the idealised pressure gradient accelerations, buoyancy flux accelerations, and buoyancy interpolation RMS errors and the resulting convergence rates, within computational limitations, for the examples shown (Figs. 1c–k). The limit to computational accuracy is reached in several cases at higher resolutions and high order schemes, even with 64-bit arithmetic, owing to error saturation / round-off error accumulation, Runge phenomena, stencils extending beyond the range for which they are useful, or a combination of some or all of these. The RMS errors (as well as absolute errors, not shown) for fluxes, derivatives, and interpolations for all orders of accuracy also were ~6–12 orders of magnitude better for the highest order approximations and/or finer resolutions, especially with the smoother function examples, in comparison to lowest order approximations. In contrast to the constant grid flux results, the integrated flux results, regardless of the order of the integrated flux stencil, converged at ~O2. Finally, the high order constant grid flux form approximation for linear diffusion converges at the order of the approximation like advective flux (not shown), especially when there are very sharp gradients, while the integrated flux form approximation for linear diffusion only converges at ~O2 regardless of the order of the stencil for the integrated flux.

Extrapolating these general results for linear problems, especially the order-of-convergence results, to expectations for nonlinear problems, even diffusion-limited problems, is not clear-cut. Although, importantly, the absolute errors for solutions probably can be expected to improve with higher order numerical approximations (e.g., Park and Lee 2009 and Norman 2021). Whether or not constant grid flux schemes are more accurate than the integrated flux schemes for nonlinear problems when the wind fields are not constant is discussed later.

3.2 | Two-dimensional colliding plumes

Results from a comprehensive suite of simulations of a dry nonlinear 2D test problem are presented to demonstrate the impact of very-high order finite difference using O3, O5, O9, O13 and O17 upwind-biased advection / flux approximations (same approximation orders were also used by G09 and Wu et al. 2021 for various WENO flux schemes), coupled with comparable even order Lagrangian interpolations for information required at off-grid point locations and even order staggered pressure gradient / divergence approximations (one order higher for odd order schemes; e.g., for O17 advection, O18 interpolation / pressure gradient / divergence is used). A summary of

the grid resolutions [200, 166.66… (hereafter 166.67), 133.33… (133.33), 100, 66.66… (66.67), 50, 33.33… (33.33), 25 m] and domain parameters used in this study are in Table I, while orders of accuracy for fluxes, interpolations, pressure gradient / divergence, diffusion, and spatial filters are given in Table II. Flux / advection numerical approximations of O3–O7 combined with O2 interpolation and pressure gradient / divergence are approximately comparable to the highest order numerical approximations that most studies in the atmospheric sciences use, thus O3 is the lowest order of flux / advection numerical approximations shown in this paper.

To accomplish the main goals of this paper, a comprehensive suite of solutions that simulate 2D warm and cold spheroidal/circular plumes colliding with each other above the ground are produced (Norman 2021). (Technically the simulations are quasi–3D as the plumes initially are infinitely long cylinders in the model, though energy cannot cascade downscale in the infinite dimension.) As the plumes approach each other, vertical gradients of state variables are enhanced, and both cold and warm air spread out laterally while thermal and shear instabilities result in the development of rotors about a horizontally oriented axis. The solutions are not symmetric in the vertical owing to asymmetric vertical gradients in density, temperature, pressure, and sound speed. Horizontally symmetric rotors develop as the plumes spread laterally and tend to grow upscale owing to the 2D slab-symmetric geometry of the domain (e.g., Fjortoft 1953; Soong and Ogura 1973). The 2D colliding plume problem was chosen as it produces steep gradients with strong deformation, rotation, divergence, and translation kinematic characteristics, which can significantly challenge different numerical schemes in different ways (e.g., S82; Schlesinger 1985). As with the S93 density current problem, the colliding plumes problem has physical features with various degrees of resolvability, including marginally resolved scales, defined here as $\leq 10\Delta$.

The two plumes were placed initially in the horizontal centre ($x = 10$ km) of a $L_x = 20$ km by $L_z = 10$ km horizontally periodic domain with the rising warm plume initially centred at $z = 3050$ m and the sinking cold plume initially centred at 7050 m. The warm and cold plumes were initialised in an adiabatic (300 K) atmosphere with cosine-squared functions with maximum and minimum potential temperature an excess and a deficit of 2.5 K and −2.5 K, respectively. The warm and cold plume both have the same geometry with radii given by 2000 m in both x- and z- directions.

An attempt was made to keep time-differencing errors for mode-split RK3 time integrations at a minimum by using the smallest number of small steps possible (six) and a small value for the Courant number $C = u\Delta t/\Delta x = 0.046875$, where $u = 15$ m s^{-1} is roughly the fastest wind in the simulations. Note that all solutions were stable with at least $C = 0.1$–0.12 and six small (fast-mode) time steps. Stable solutions were also possible for all orders of schemes with C ~0.375 (e.g., $\Delta t = 2.5$ s for $\Delta x = 100$ m) and 18 small time steps with $\Delta\tau$ ~0.13688… s assuming sound speed c_s ~ 330 m s^{-1} and $\Delta x =100$ m (sound speed Courant number ~0.45833…) to keep the integration of sound modes stable. Larger values of Δt would require even more small time steps (24 small steps would be the next number divisible by 2 and 3 for RK3 time integration) with somewhat higher values of C possible with additional small time steps for lower order approximations. A constant eddy mixing coefficient ($K_m = 10.0$ m^2 s^{-1}; use of $K_m = 4$ m^2 s^{-1} was attempted and provided more complex colliding plumes solution, but also required a very fine grid reference solution) was applied to all variables except pressure to provide an approximate grid converged diffusion-limited solution at $\Delta x = \Delta z = 25$ m resolution. Finally, a weak O18 spatial filter (S82; Purser 1987 P87; PL88; K07, etc.) with a coefficient of $\alpha = 0.03$ so that $2\Delta x$ waves are damped 3% every time step, was applied in both x- and z- directions to perturbations of all variables from their base state (except pressure). The spatial filter coefficients are time step dependent (K07) and use of very large or small values can adversely impact solutions. The optimal grid resolutions and orders of accuracy of numerical approximations for efficiently achieving reasonable solutions are dependent on the values of K_m and α for a given problem. The value for α was chosen in order to not overly smooth the odd order flux scheme solutions. For comparison, the value of α used in this study was eight times smaller than the value of 0.24 [though Knievel et al. 2007 K07 state the value of α was effectively 0.2 with the Xue (2000) flux limited form of the filter] used in the Weather Research Forecast (WRF) model (K07), and ~11.1 and 3.3 times smaller than the corresponding value for α in the 17-point (O16) Shapiro filter applied once every three, or ten, time steps, respectively, in the study by S82]. Filter coefficients herein were chosen to be selective for higher wavenumber (small Δx) by choosing appropriate values for two parameters, R (rolloff) and S (smoothness), $(R, S) = (18, 0)$ for the O18 filter, as described by P87 and PL88, noting that PL88 employed slightly more damping of smaller wave numbers and a filter that had a higher order than the advection order.

The best solutions for a given resolution, based on linear theory, theoretically should be those produced using the high order approximations for all interpolations and finite differences. A summary of the suites of experiments to demonstrate the impact of very high order fluxes, SGS turbulent fluxes, interpolations, and pressure gradient / divergence terms is summarized in Table II. The evaluation of the results is derived from both visual comparisons and objective error measures. The names of the structures in the colliding plume solutions (regions of the solution) that are discussed herein are depicted in a schematic in Appendix A.

3.2.1 | Very high order solutions without a mean wind

3.2.1.1 | Reference solution

The importance of finer resolution to produce more accurate viscous solutions was well summarised by Ooyama (2001 O01) who stated, "…at finer resolutions, where the diffusion is dominant in the small-scale dynamics, the model solutions converge toward the ultimate solutions…" (i.e., a reference solution). In much coarser-resolution solutions, when artificial viscosity is unable to control errors, which can be from high frequency 'noise' associated with many types of schemes, solutions begin to lose integrity. Solution performance evaluation at intermediate resolutions (no consensus about a rigorous definition for intermediate) is often useful to compare solutions when diffusion is not excessively dominant and does not overwhelm the effect of any improvement in errors by high order schemes [as is well known, for linear problems, numerical schemes that are both stable and consistent (regardless of the order of accuracy) theoretically will converge as Δx and Δt go to zero (e.g., Haltiner and Williams 1980, Richtmyer and Morton 1994, Durran 2010)].

Objective comparisons of test solutions with finer-resolution reference solutions are more difficult when solutions are generated on staggered grids, as one of the solutions has to be interpolated to the grid points of the other. If O2 interpolations are used to compare solutions on a common grid, as done in this study, comparisons can still be useful, although they might be less accurate (WSK22) than if higher order interpolation were used (Zhang et al. 2003). Re-computation of the objective errors using O4–18 interpolations to compare solutions on a common grid surprisingly produced very little impact on the objective error calculations and no impact so ever on the

conclusions. With regard to the concept of nearly grid converged solutions, flow and scalar fields generally will become sufficiently resolved and smooth for increasing resolution such that the higher order derivatives become increasingly well posed and well behaved, largely as a result of the constant eddy-mixing turbulent diffusion (or in other studies by flux-limiters; e.g., N21). In this paper convergence of solutions using any higher order scheme for nonlinear problems means that the objective error measures are generally improving, as the nonlinearity significantly reduces convergence rates below the theoretical rates usually found for linear problems, and typically is at best O(1) to O(2) as discussed by, for example, Hernrick et al. (2005), and N21.

Comparisons of the perturbation potential temperature fields for the $\Delta x = \Delta z = 25, 50, 66.67, 100,$ and 200 m resolution constant grid flux solutions integrated with time step $\Delta t = 0.625, 0.3125, 0.20833…, 0.15625,$ and 0.078125 s, O17 constant grid flux numerical approximations for advection (the highest order shown), and comparable order interpolation and pressure gradient / divergence (Fig. 2), show, as expected, that finer resolution solutions have smaller maxima and minima, less apparent numerical noise, and better representation of smaller scale features, some of which are marginally resolved or more marginally resolved at coarser resolutions. (A more complete suite of solutions, with $\Delta x = \Delta z = 25, 33.33, 50, 66.67, 100, 133.33, 166.67,$ and 200 m, for potential temperature and KE are provided in Supporting Information Figs. S4 and S5, respectively.) Figure 2 shows most of the whole domain for the highest order (O17) solutions, and only O17 solutions are shown as they generally the most accurate. These solutions converge much slower than the theoretical convergence as previously discussed (calculated convergence rates for the nonlinear problem for all orders and resolutions are provided in Supporting information Table S7). Wicker and Skamarock (2002) commented that their density current simulations with a free slip lower boundary "should remain perfectly symmetric" with an added mean wind, and should not change the solution; their experience shows that adding a mean wind a) "is a more stringent test of splitting methods" and b) "translation magnifies numerical phase errors associated with the advection scheme", which more strongly challenges the numerical scheme. The wind speed added was determined from one perfect transit to the west of the plume systems around the periodic domain with $U_t = -20$ m s^{-1} = -20000 m / 1000 s, which was roughly the same speed as the fastest winds, which are ~15 m s^{-1} in the solutions without an added wind. The O17 solutions with the added mean wind converged more slowly than those without the added mean wind, suffered from

significant asymmetries for resolutions ≥ 66.67 m, especially in the region of the upwind side of the upper rotor. The solutions were increasingly less asymmetric for resolutions of ≤ 50 m, and not until resolutions were ≤ 33.33 m were asymmetries not readily visible in both perturbation potential temperature and KE fields. Lower order solutions not shown have more significant asymmetries as discussed later.

Finer resolutions also produced, as expected, better potential temperature and KE RMS errors and L_∞ error norms computed against the 25 m nearly grid converged solution (Fig. 3). The RMS error, L_∞, L_2, and L_1 error norms (e.g., Shu 1997), are commonly used in numerical analysis to provide bulk error measures of solutions against a reference, although they provide no direct information about phase and amplitude errors. Based on RMS errors (Fig. 3a–b) against the O17, $\Delta x = \Delta z = 25$ m, which is considered the reference solution, both the perturbation potential temperature and KE field solutions for this nonlinear problem converge at roughly O1–2 at coarser resolutions ≥ 66.67 m and roughly O2 for some of the higher order and higher resolution simulation measures. The convergence rates also are slightly greater than O2 for some finer and coarser resolutions. There was overall slightly slower convergence for KE than for perturbation potential temperature in both the RMS and L_∞ error measures (Fig. 3a–b) with KE L_∞ having the slowest convergence overall of the objective measures shown (see also Table S7 for computed convergence rates). Diffusion and filter errors, which are O2 in both space and O2 in time as they are integrated on each stage for RK3 time integration, also might be contributing by an unknown amount to reduced convergence rates. Clearly, and unsurprisingly, none of the nonlinear solutions converge at the theoretical rate predicted by linear theory for any given order of accuracy. These convergence rates were much lower than the scheme orders, which is consistent with results described by N21 (see Table 7 in N21) for comparisons between test solutions and a grid converged solution using a nonlinear, shock producing, 1D Euler problem.

The maximums and minimums of perturbation potential temperature do not approach the 25 m solutions within 10% until solutions are made with resolutions <133.33 m (not shown; see Supporting Information Fig. S4), while resolutions of <66.67 m are required for the solutions to become more visually comparable (Fig. 2). Additionally, while the visual appearance of generally smooth velocity and pressure fields is more similar amongst solutions with different resolutions

(not shown; see Supporting Information Fig. S5 for KE fields), the errors and convergence rates of all the state quantities (not shown) were comparable to those for perturbation potential temperature and KE (Fig. 3), and as expected, errors improved with increasingly finer resolution. The L_1 error norm (absolute error norm for perturbation potential temperature, which is of order or magnitude one, thus, relative and absolute errors are similar order; not shown) between the O(3–17) 33.33 m simulations and the O17, 25 m simulation, all at t = 1000 s, ranged from ~4.12 x 10^{-3} to 1.16 x 10^{-3} K. Additionally, L_1 error norms between the O3–17, 50 m solutions and the O17, 25 m solutions, all at t = 1000 s, ranged from ~4.81 x 10^{-3} to 3.79 x 10^{-3} K. These two sets of resolution comparisons show that all L_1 errors between 50 and 25 m and 33.33 and 25 m met the Zhang et al. (2003) L_1 error norm <0.01 criterion to indicate convergence for their viscous Rayleigh-Taylor problem. In contrast, the L_1 error norm between the 100 and 50 m solutions were 3.71 x 10^{-2} to 2.64 x 10^{-2} K, demonstrating these solutions were not converged according to the L_1 error criterion.

Importantly, the colliding plume problem was chosen as it remains in the middle of the domain in contrast to the density current problem which impinges on the lower boundary where lower order numerical approximations are traditionally employed [in contrast to the inverse Lax-Wendroff procedure, discussed by Tan and Shu (2013), to produce high order boundary and near-boundary fluxes]. The popular rising single plume problem also does not impinge on the lateral or vertical boundaries for over 1000 s, and could have been used, however, a single plume does not produce the very complex flow features as the S93 density current or the colliding plumes problems for the values of eddy mixing used herein. To affirm the independence of the colliding plumes problem on the specification of the boundary conditions, test solutions made using either free-slip or semi-slip boundary conditions for the bottom boundary and especially the top boundary for the test problem were remarkably indistinguishable both visually, and objectively in terms of maximum and minimums of perturbation potential temperature differing in the third–fifth or larger digit at 1000 s with a resolution of 100 m and decreasing to only the fifth–seventh digit at 1000 s with a resolution of 33.33 m. The primary reason for such small differences includes that at 1000 s, perturbation potential temperatures were generally <2 x 10^{-3} K within ~2000 m of the boundaries, and that horizontal (vertical) winds were generally 0–2.2 m s^{-1} (<0.5 m s^{-1}) within ~500 m of the

boundaries with the largest values only in regions of horizontal extent of roughly ~2500 m above and below the rotors.

As a note, an O17, 16.66... m (denoted as 16.67 m) solution was produced, which resulted in very small absolute differences of 6.30 x 10^{-3} and 1.97 x 10^{-3} K for the maximum and minimum from the O17, 25 m potential temperature solution against the O17, 16.67 m solution, absolute differences of 8.93 x 10^{-3} m s^{-1} for the u velocity (u velocities are symmetric), and 8.75 x 10^{-4} and 3.40 x 10^{-3} m s^{-1} for the maximum and minimum for w velocity. Interestingly, the differences for vorticity and deformation maximums and minimums were much less closely converged, and relative errors (not shown) were more than an order of magnitude larger than those for the velocities. Comparisons of the O17, 25 m solutions using Richardson extrapolation solutions produced from the O17, 33.33 and 25 m solutions (not shown) further demonstrated a nearly converged solution for the state variables in the 25 m reference solution.

Finally, O17, 25 to 200 m solutions (reference solution numerical approximations) with O18 accurate SGS turbulent fluxes based on constant grid flux and integrated flux formulations (see Supporting Information Fig. S6 for solution made at 25 to 200 m) produced very similar results to the simulations made with O2 accurate SGS turbulent fluxes (Fig. 2, and Supporting Information S4). At 25 m resolution the differences were very small with maximum (minimum) amplitude differences of 4.14 x 10^{-3} K (2.64 x 10^{-3} K) for potential temperature, 7.57 x 10^{-4} m s^{-1} for the u velocity (maximum and minimum are equal because u is perfectly symmetric), and 2.95 x 10^{-3} m s^{-1} (1.22 x 10^{-2} m s^{-1}) for the w velocity, respectively, using O18 accurate constant grid flux SGS turbulent fluxes. These same differences were consistently about twice the amplitude of those found using high order integrated flux formulations for SGS fluxes as integrated flux approximation are only ~O2 accurate, regardless of stencil length and implied order, as were the SGS fluxes in the reference solution. In summary, the findings of this study were not sensitive to the use of either O2 SGS fluxes, or the either form of very high order SGS fluxes, in the 25 m reference solution.

Finally, sensitivity to lower and upper boundary conditions were considered since the colliding plume problem was chosen as it remains in the middle of the domain for more than 1000 s, at least

vertically where lower numerical approximations were employed. The popular rising single plume problem also does not impinge on the lateral or vertical boundaries for over 1000 s, and could have been used. However, a single plume does not produce the more complex flow features seen with the colliding plumes problems for the values of eddy mixing used herein. In contrast to the single plume problem, the S93 density current test problem produces more complex flow features that are generated by a cold plume that impinges on the lower boundary. Moreover, the use of free-slip conditions produces vastly different density current solutions compared to semi-slip conditions. In all of these test problems lower order numerical approximations are traditionally employed near the vertical boundaries [in contrast to the inverse Lax-Wendroff procedure, discussed by Tan and Shu (2013), to produce high order boundary and near-boundary fluxes]. To affirm the independence of the colliding plumes problem solutions to the specification of the boundary conditions, test solutions were made using either free-slip or semi-slip conditions for both the bottom and top boundaries. These solutions were remarkably indistinguishable from each other both visually, and objectively in terms of maximum and minimums of perturbation potential temperature, which differed in the third–fifth or larger digit at 1000 s with a resolution of 100 m and in the fifth–seventh digit at 1000 s with a resolution of $\leq$33.33 m. The primary reason for such small differences at 1000 s was that the amplitudes of the perturbation potential temperature were generally <2 x 10^{-3} K within ~2000 m of the vertical boundaries, and that horizontal (vertical) winds were generally 0–2.2 m s^{-1} (<0.5 m s^{-1}) within ~500 m of the boundaries with the largest values only in regions of horizontal extent of ~2500 m above and below the rotors.

3.2.1.2 | Effect of resolution and order or accuracy for flux approximations (Set A)

The O3–17 upwind-biased, constant grid flux schemes solutions made without an added mean wind (Set A) using spatial resolutions of 25, 33.33, 50, 66.67, 100, 133.33, and 166.67 m, all with the same spatial filter and Courant number C, are now compared more closely, both visually and objectively. Perturbation potential temperature (Figs. 4 and Fig. 5 show zoomed-in and more zoomed-in views on the left side of the domain with resolutions of 33.33, 66.67, 100, and 133.33 m), perturbation potential temperature difference between reference and test solutions (Fig. 6, zoomed as in Fig. 5), kinetic energy per unit volume [KE = 0.5 ρ ($u_i \cdot u_i$); Fig. 7; zoomed as in Fig. 5], vorticity [2D vorticity in the xz-plane = ($\Delta u/\Delta z - \Delta w/\Delta x$); hereafter vorticity; Fig. 8, zoomed as in Fig. 5], and deformation [2D deformation in the xz-plane, S = [($\Delta w/\Delta x + \Delta u/\Delta z)^2$ + ($\Delta u/\Delta x -$

$\Delta w/\Delta z)^2]^{1/2}$; hereafter deformation; Fig. 9, zoomed as in Fig. 5] at $t = 1000$ s show the importance of very high order numerical approximations as a function of resolution for the colliding plumes problem.

Based on visual appearance of the perturbation potential temperature, kinetic energy, and vorticity, and deformation, the authors conclude that the solutions, with increasing order of numerical approximations, are close between O3 and O5 and almost indistinguishable between O5 and O9 at 25 and 33.33 m; close between O5 and O9 and almost indistinguishable between O9, 13, and 17, at 66.67 m; close between O9 and O13 and very close between O13 and O17, at 100 m; and close between O13 and O17, at 133.33 m. This descriptive assessment is based on regions of the perturbation potential temperature fields that compare well for various orders and resolutions especially in the regions with flow structures defined in Appendix A. Zoomed-in views (Fig. 4 and Figs. 5–9) are shown for the spatial portion of the solutions where the largest errors generally occurred in the simulations at $t = 1000$ s, which was in the vicinity of the marginally resolved upper rotor and the front and back side of the potential temperature leading and trailing edge fronts with the larger scale circulation. These regions also had strong gradients of all variables, as well as strong rotation and deformation. Cross-sections at $z = 6850$ m through the upper rotor for the 100 m solutions are included in Figs. 5–9 for the variables and their differences from the reference solution (note the differences for deformation and vorticity should not be considered in an absolute sense, rather they should only be used as indicators of the regions of largest absolute values as these variables are grid-scale dependent; although when the solutions become nearly grid converged they should not depend so much on resolution). The cross-sections for all variables clearly show that the O3–5, 100 m solutions have pronounced phase and amplitude errors, while O9–17 schemes generally perform much better.

The results in Figs. 2–9 show the higher order schemes and/or finer resolution solutions better matched the 25 m, O17 reference solution as expected. The visual appearance and cross-sections show that the solutions also were increasingly closer to the reference solution, as each incremental increase to higher order accuracy improved the solutions, although from a visual perspective, the rate of improvement decreases for the ≥O9 schemes with increasing order of accuracy (consistent with Shu 2020). The weaker performance of some solutions at very coarse resolutions (e.g., 166.67

and 200 m; see Figs. 2 and 4) was due to the lack of spatial resolution to resolve relevant flow features with spatially large difference stencils that spanned multiple features and sharp gradients (e.g., O13 and O17; Durran 2010 and Wu et al. 2021), increased aliasing and dispersion errors (e.g., Durran 2010), and the excitation of unrealistic physical shear and buoyancy instabilities associated with overshoots produced by these errors, which then can then amplify in a positive feedback (Grabowski and Clark 1991). At the lowest orders of accuracy, odd order upwind-biased schemes are well known to inherently damp all wavelengths as they are diffusive, although they tend to damp shorter wavelength features more than longer wavelength features (e.g., compare O3 and O5 solutions in Figs. 2, 4–9). In addition, small phase errors in the solutions often resulted in very large difference errors, especially in and near strong gradients. At the highest resolutions, the lowest order schemes performed reasonably well except that there were still rather small visually detectable differences. Overall, the errors in the simulations are evident to varying degrees in the RMS errors and L_∞ error norms (Fig. 3a–b), as well as differences in the maximum and minimum values (Fig. 2). The actual phase errors are difficult to compute (not attempted), however, phase error effects can be inferred visually, to some extent, when higher potential temperature bands of the rotors are spatially offset in such a way that if the solution were shifted left or right, or up or down, etc. one sees a substantial drop in the errors. Overall, compared to the reference solution, the results show visually that resolutions ≤ 133.33 m, and $\geq$O9 accuracy were needed to at least very marginally resolve the gross flow structures, while resolutions ≤ 66.67 m were needed to highly resolve the rotor bands and state variable gradient details for all orders of accuracy (e.g., Figs. 2 and 4–9).

The root mean square (RMS) error and L_∞ error norm measures (Figs. 3a–b) for the O3–17 order of accuracy and resolutions of 25–166.67 m can be used to establish improved accuracy beyond that which can detected by visual appearance. The appearance differences between test and reference potential temperature solutions (Fig. 6) and objective error measures for perturbation potential temperature and KE (Fig. 3a–b) demonstrated, as expected, that finer resolution and higher order numerical approximations produce better results when compared to the reference solution.

Additionally, objective errors from O3–13, 100 m solutions computed against the O17, 100 m solution (a reference solution specifically for the 100 m solutions) for perturbation potential

temperature, KE, and the derivative quantities, enstrophy and deformation squared, show expected improvements with each increase in order of accuracy (Figs. 3c–d). The O17, 100 m solution was used to compute errors in this manner for the un-converged scale-dependent derivative in the intermediate to coarse grid resolution ranges. Note however that error improvements of the 100 m solutions against the errors of the O3–13, 100 m solutions are better than against the 25 m solution as the errors of the 100 m, O17 solutions have at least part of the O17, 100 m solution error computed against the 25 m solution removed. The 25 m wind solutions could have been coarse-grained, which has some troublesome caveats, including how representative a coarse-grained 25 m solution would be of the reference solution. Importantly, the objective error measures show measurable improvements all the way to O17 as a function of resolution and/or as a function or accuracy.

Most of the simulations herein capture the important resolvable gross characteristics such as the upper and lower rotors as well as the leading and trailing frontal gradients with resolutions of 100 and 133.33 m (e.g., Fig. 4). However, for these resolutions, the difference between test and reference potential temperature solutions (Fig. 6) was often as large as ~0.1–1 K, but near the upper rotor and near fronts / strong gradients there were often local differences of very large absolute values >2.0 K (or >80% of the initial maximum/minimum perturbation potential temperature excess / deficit), in some solutions with finer resolution and / or higher order numerical approximations. Comparisons of maximums and minimums of the velocity components with the reference solutions (not shown) have differences of ~8–10% between adjacent ordered schemes, and as high as ~15% amongst all of the orders considered. Differences of this type for the pressure fields were generally <5–8%. Unsurprisingly, the difference fields were generally the smallest with the finest resolutions overall for a given order of accuracy as well as with highest order accuracy for a given resolution. At coarser resolutions with lower order numerical approximations, some of the visual differences (Figs. 4–9) and error measures (Fig. 3) were smaller only because the solutions (e.g., O5 versus O9) were more damped by the lower order flux schemes and not impacted as much by 'overshoots' (effectively numerical noise) from the flux computations. Damping of small-scale overshoots and undershoots with lower order schemes could be seen to be somewhat advantageous, however, the whole solution is also affected, thus reducing the overall solution accuracy.

Improvements based on visual appearances were most apparent between O3 and O5, and to a lesser extent between O5 and O9, and so on (e.g., Figs. 2 and 4–9), consistent with behaviour Shu (2020) discusses for WENO schemes. The visual errors for ≤O9 numerical approximations in most solutions were likely associated with both amplitude and phase errors that improved quickly as order of accuracy was improved from O3 to O9, while visual errors for >O9 numerical approximations improved more slowly (e.g., Figs. 2, 3, 4–9). Both visual comparisons and objective error measures demonstrated that solutions continue to improve as order of accuracy was increased toward O17. Improvements for O19 or higher order solutions (not shown) were very small and sometimes there was degradation, presumably, in part, because round-off error becomes more important for extremely high order finite differences. While the degree of visual improvements decreases for each successive order of accuracy increase, resolution refinement, or both, the improvements relative to the previous refinements continue to be seen in the error measures (Fig. 3). Interestingly, the objective error measures for ≤O13 schemes did not improve as much as expected when resolutions were refined to ≤50 m. In contrast, objective measures improved quickly for the O17 scheme, especially for resolutions ≤66.67 m. This might have to do with the fact that O17 was used in producing the 25 m nonlinear reference solution.

A possible, well-known contributing factor for convergence-rate plateaus that can occur with finer temporal resolution, higher order accuracy temporal schemes, and/or multi-function / multi-stage temporal schemes, is roundoff error accumulation / saturation, both with and without double precision computational arithmetic (e.g., WSK22, their Figs. 5 and 6). As seen in WSK22, this seems to be more prominent with multi-function / multi-stage time schemes, which have more computations per time step at each grid point. Obviously, higher order numerical approximations can be helpful to produce more accurate solutions both objectively, and in some regards visually, when flow structures, scalar field characteristics, and physics are not excessively under-resolved. Finer resolutions also can be helpful as long as the schemes are not excessively impacted by, for example, various numerical errors and inherent damping, such as in the lowest order schemes in this study. Unsurprisingly, there is only so much improved accuracy, if at all, that can be obtained with high order numerical schemes when coarser resolution is used.

3.2.1.3 | Integrated flux versus constant grid fluxes (Set A.IF)

High order ($\geq$O2) integrated flux schemes are O2 at best, both theoretically and experimentally based on linear analysis for advection, while constant grid flux schemes for advection retain the accuracy of a pure advective scheme (Fig. 1). These behaviours were also demonstrated in T87 for the rotating cone problem. One might expect that high order integrated flux and constant grid flux schemes might perhaps perform comparably for nonlinear problems, however, experiments in Set A.IF (Fig. 10, zoomed as in Fig. 5 and Supporting Information Fig. S8, zoomed as in Fig. 4) show the significant negative impact on all solutions using the integrated flux. Clearly, the integrated flux schemes did not perform as well as the constant grid flux scheme for the nonlinear test problem, especially near the stronger upper rotor, where the strongest gradients and smallest structures evolved. In contrast to constant grid flux solutions, integrated flux solutions, especially at resolutions of 133.33, 100, 66.67 m, and to a lesser but still substantial degree with 50 and 33.3 m, had excessively large magnitudes of perturbation potential temperatures (Fig. 10 and Fig. S8), especially near the marginally resolved upper rotor, consistent with T87 for linear rotating cone experiments. The errors in these regions resulted in perturbation potential temperatures differences from the O17, 25 m reference solution of >30% in the O3–17, 50 m integrated flux solutions, while in comparison these were generally <9% (1.5)% for the O3–9 (O13–17) constant grid flux solutions. Additionally, the potential temperature RMS errors for the 100 m, integrated flux solutions were (RMS = 0.1568, 0.1531, 0.1404, 0.1367, 0.1376) for the odd order O3–17 integrated flux solutions, which were worse than those of the O3–17, 100 m odd order constant grid flux solutions (RMS = 0.1424, 0.1072, 0.07800, 0.07088, 0.07026). Furthermore, the RMS errors for the $\geq$O5, 100 m (and also $\geq$O9, 133.33 m) constant grid flux solutions were better than all integrated grid flux RMS errors for any order with the same resolution. In contrast, both schemes performed comparably where the flow structures were well resolved, such as near the lower rotor and distant from the disturbed flow regions. The reasons for these differences seemed to be associated with somewhat better performance of constant grid flux in regions with smoother flow, as well as higher accuracy in marginally resolved flow structure.

In summary, the integrated flux solutions improved much more slowly from O3 through O17 for any given resolution, when compared to constant grid flux solutions, which was consistent with the convergence behaviour for the linear problem as shown earlier. In addition, integrated flux

scheme objective errors were notably worse than those produced by constant grid flux schemes for any of the resolutions considered, even with 33.33 and 25 m (not shown) resolution (e.g., the integrated flux scheme with O17 approximations, had RMS errors for 33.33 and 25 m resolutions of 0.02055 and 0.01182 K, L_∞, norm errors of 0.7986 and 0.4599 K, and maximum and minimum potential temperature values that were 2–4% and 5–10% in error, respectively, compared to the reference). Henceforth, all remaining simulations discussed herein use only constant grid flux.

3.2.1.3 | Computational effectiveness

Historically, cost-effective comparisons and assessments of high order numerical approximations for complex nonlinear solutions by, for example, SZS03 and Latini et al. (2007) for O5, and 9, and 2D non-viscous nonlinear Rayleigh-Taylor (a problem with much more detailed flow structure compared to simple rising plumes that are often used in atmospheric sciences) solutions, and N21 for colliding plumes solutions for O3, 5, 7, and 9, were based largely on visual comparisons. The non-viscous and very highly nonlinear nature of their solutions precluded meaningful objective error comparisons, as obtaining reference solutions is not feasible without diffusion. In particular, SZS03 and Zhang et al. (2003) demonstrated that an O9 WENO flux scheme could produce cost-effective, by a factor of two, comparably complex fluid flow solutions compared to an O5 WENO advection solution made with finer resolution. Their O9 coarser resolution solutions were 66–80% less expensive in computational costs compared to their O5 finer resolutions solutions. Zhang et al. (2003) also found similar cost effectiveness when the Rayleigh-Taylor problem used in SZS03 was solved with various levels of viscosity with Reynold numbers Re $\geq$25000. They found the largest errors near the fine-scale structures and examined these regions "to observe visually the convergence of the numerical solutions." More recently, Wu et al. (2021) attempted both visual and objective comparisons for their O5, 9, 13, and 17, 2D highly nonlinear, non-viscous Rayleigh-Taylor solutions, and expectedly showed slower order of convergence than the order of the numerical approximations for all orders of accuracy considered, as was found herein for a smoother nonlinear problem. Moreover, they showed that O9 solutions occasionally had better L1 and L_∞ error norm measures than their O11, O15, or O17 solutions.

The issue of cost-effectiveness for higher order fluxes with coarser resolutions compared to lower order fluxes with finer resolutions has not been as well demonstrated for very viscous diffusion-

limited problems (e.g., Re ~100) as it has been for simple linear problems and to some degree with complex non-viscous or weakly viscous nonlinear problems. Improvements were not expected to be as dramatic for the very viscous flow colliding plumes problem used in this paper owing to the effects of diffusion, and indeed this was found to be the case.

To examine the issue of cost-effectiveness for the very viscous, diffusion-limited colliding plumes, computational cost, based on an estimate of total floating-point operation (FPO) counts used in the model, where all operations (add, subtract, multiply, divide, absolute value, if-then, etc.) are assumed to have equal computational cost, is shown (Fig. 11a and the table inset in Fig. 11). These results are shown for each order of accuracy as a function of grid resolution in terms of total floating-point operations (FPO) per grid point per time step for the three-stage RK3 mode-split time integrations using two, three, and six fast mode small time steps for stages one, two and three, respectively. These FPOs are considered to be 'theoretical costs' (Zhang et al. 2022). Cost-effectiveness based on FPOs provides machine-independent comparisons, although FPOs should be considered the worst cases scenario in term of cost-effectiveness in some cases as actual CPU timings often provide better computational speed performance for some codes owing to efficient cache use. The same small Courant number was used for all orders so that a) the same number of small steps was always the same for integrating the fast sound modes, and b) temporal differencing errors were kept lower, which was not always the case in these types of simulations (e.g., S93, their Fig. 4), even with RK3 time integration (e.g., Park and Lee 2008, their Fig. 10). Additionally, it is useful to keep in mind that the CFL criterion for explicit time integration of SGS turbulent fluxes in regions with very fine resolution (e.g., for a stretched grid) and very large fluxes near a lower boundary (e.g., hurricane or tornado), can exceed the CFL criteria for advection (this issue can be avoided with implicit solvers for diffusion, although implicit solvers have other issues). With theoretical FPOs, only a few cost-effective solutions were found between O3 and next coarser resolution ≥O5 solutions, as well as some O9 and next coarser O13–17 solutions (fine resolutions; Figs. 11b, c). Some of the O5 and next coarser resolution O9 solutions were roughly cost-comparable, at least visually, but not objectively. In contrast, solutions made with very high order ≥O13 fluxes, coupled with very fine resolutions ≤33.33 m, were generally somewhat cost-effective using objective-based error measures, as was expected, owing to better convergence rates for smoother solutions, although seeing this visually tended to be difficult. Additionally, it is worth

noting that coarser resolution solutions made with O5 fluxes performed roughly as well, and in some cases as well as next finer resolutions with O3 fluxes.

The cost-effectiveness results above were not adjusted for the Courant number reduction associated with the use of higher order of numerical approximations for stable time integration [e.g., Courant number for linear stability from section 2; O3/O5 ~1.13, O5(3)/O9 ~1.27(1.44), O5(3)/O13 ~1.44(1.63), and O5(3)/O17 ~1.56(1.77); CFL generated following Haltiner and Williams (1980), Fornberg (1987), Straka and Anderson (1993), especially Baldoff (2008), etc.]. Increasing the Courant number also typically required an increased number of small time steps by up to a factor of four for stable fast mode time integration, and as is well known, generally led to larger objective error measures (e.g., Haltiner and Williams 1980; T87). Nevertheless, calculating the FPOs for larger stable Courant numbers with lower order approximations made most of the comparisons shown in Fig. 11 less cost comparable than with constant Courant numbers, although the highest order flux ≥O13 (O17) solutions with finer resolutions ≤33.33 m, were marginally cost-effective, compared to O9 (O13), 25 m solutions.

However, as stated above, use of the total FPOs to assess cost-effectiveness, should be considered a 'worst-case' scenario, especially for intermediate solutions. For example, Balsara and Shu (2000) showed that an O9 WENO scheme required 3.4 times more FPOs than an O5 WENO scheme, while in practice, with efficient cache use, their O9 scheme only required 30–50% more CPU than their O5 scheme. The ratio of the total FPOs (Table in Fig. 11) for O9 to O5 (O17 to O9) upwind-biased flux solutions in this paper is ~1.42 (1.59), while this ratio is ~1.75 (1.92) with near maximum CFLs. In contrast, the ratio of actual CPU for O9 to O5 (O17 to O9) is ~1.07 (1.13), while this ratio is ~1.32 (1.21) with near maximum CFLs. The CPU estimates were based on an average of five simulations and only included computations for the flux, interpolation, buoyancy, diffusion, filter, pressure gradient and divergence, and boundary calculations, but not CPU for model startup, input/output, and run-time statistics for state variables, etc. It is important to keep in mind that the computations for many of the flux, SGS turbulent flux, etc. terms require substantial supporting calculations regardless of the order of accuracy. The practical (actual) cost-effectiveness, based on FPOs, of the solutions shown in Fig. 11 for the two comparison examples (O9 to O5 and O17 to O9) were under-estimated by 32 and 59%, respectively (i.e., they were faster

than the theoretical cost). The CPU/cache-based results are not shown as in Fig. 11 as they can be machine dependent, while FPOs are purely theoretical. Use of lower-order (e.g., O4) pressure gradient and divergence, and especially interpolation, can further reduce FPOs (Table inset in Fig. 11) and can improve the potential for cost-effectiveness. Another limitation to the interpretation of Fig. 11 is that the objective errors do not necessarily represent the optimal solutions since some solutions visually have some important characteristics that are closer to the reference solution, but their objective errors are larger, (possibly owing to amplitude and phase errors, etc.) and vice-versa.

In summary, based on Fig. 11, and especially when including near maximum CFLs (not included in Fig. 11), the diffusion-limited nature of the test problem seems to have compromised, at least partially, and in many cases wholly, the cost-effectiveness of higher order solutions in comparison to previous studies that used either smooth linear problems or complex non-viscous / weakly viscous nonlinear solutions. Fortunately, more advantageous cost-effectiveness can sometimes be possible for high order solutions through careful use of computer CPU / cache. These cost-effectiveness results generally will be more improved (or less-worse) for 3D simulations. Cost-effectiveness can also be improved with high order fluxes by using lower order interpolations and pressure gradient / divergence (and not filtering) during the first two stages of the three stages of the RK3 time integration. Gadd (1980) showed little or no loss of accuracy using O2 spatial numerical approximations on the first stage of Lax-Wendroff time integration and O4 spatial approximations on the second stage. As discussed later, the overall O1 to O2 convergence rates (e.g., Fig. 3 and Table S7) associated with the mode-split RK3 time scheme, were negatively impacted by temporal convergence rates of $\leq$O1 compared to O3 with spatial filter, SGS turbulence and divergence damping turned off, which demonstrates the influence of these on overall convergence rates and their possible negative effects on cost-effectiveness.

The lack of cost-comparable and/or cost-effective solutions using very high order numerical approximations to solve nonlinear problems does not argue entirely against their utility for testing schemes, as discussed by Park and Lee (2009). Most comprehensive atmospheric models have complicated physical parameterizations that account for a large portion of the CPU time consumed by these models. In these cases, the use of higher order numerical approximations for advective

fluxes probably would not be an excessive computational burden even if the high order schemes were not cost-comparable or cost-effective. Additionally, higher order schemes, for a given resolution, can generally provide better solutions through better mass and energy conservation along with reduced phase and amplitude errors (e.g., Haltiner and Williams 1980; Purser and Leslie 1988; Balsara and Shu 2000; Desjardins et al. 2008). Therefore, the issue of requiring cost-effectiveness to achieve the best solution for the least computational cost can be less relevant if the computational resources are unavailable for spatial resolution to be increased, as can easily happen in 2D or 3D, but if instead, order of accuracy can be increased. In the case when computational resources are unlimited, perhaps the main drawback of using higher order numerical approximations might be associated with roundoff error with extremely high order schemes and 32-bit computer mathematics.

3.2.3 | Very high order solutions with a mean wind (Set B)

The effects of dispersion, dissipation and phase errors (e.g., Durran 2010 and WS02) in numerical schemes can be more readily demonstrated by adding a relatively strong mean wind to the initial conditions for Set A, and these are shown as Set B. Solutions with the added mean wind (Fig. 2, right column) are not symmetric until resolution is refined to <66.67 m and are not visually nearly indistinguishable from the solutions without the added mean wind (mathematically, the ideal solutions should be Galilean invariant) until resolution is ≤33.33 or 25 m (Fig 2; also see Supporting Information in Fig. S4 and S5 for all resolutions for both perturbation potential temperature and KE per unit volume).

Behaviours of the perturbation potential temperature fields solutions with resolutions of 25, 33.33, 50, 66.67, 100, 133.33, and 166.67 m resolution (Fig. 12) and zoomed-in plots of perturbation potential temperature, perturbation potential temperature difference from the reference, and KE (Figs. 13, 14, and 15, zoomed as in Figs. 5, 6, and 7) at $t = 1000$ s also show that the highest odd order constant grid flux schemes, as expected, produced the best solutions amongst all those with an added mean wind in terms of rotor shape preservation as well as subjective phase and amplitude errors (Fig. 2; recall a perfect scheme and perfect arithmetic would not have errors regardless of the magnitude of mean added wind). For example, the errors in the locations of the leading front and upper rotor were generally reduced visually compared to those in the no-wind simulations

when resolutions of 100, 66.67, 50, and 33.33 m were used with each of ≥O13, ≥O9, ≥O5, and ≥O3 numerical approximations, respectively. Additionally, symmetry is lost in coarse resolutions solutions (e.g., see Fig. 2 right column for the O17 solutions) made with the added mean wind owing to variations in dispersion and phase errors in the parts of the solutions moving with and opposing the flow, especially for lower order (<O9) schemes. Difference plots for potential temperature (Fig. 14) show the larger phase errors as large positive and negative dipoles near regions of stronger gradients, especially with lower order numerical approximations and/or coarser resolutions. While the nature of phase errors can be difficult to interpret, quantify, and understand, their impact is readily seen as displacements of flow structures. Solutions made with an added mean wind showed that potential temperature and KE fields in the highest order ≥O9 solutions were generally well behaved for resolutions ≤66.67 m with visually smaller errors than lower order solutions, as seen by better preserved maximums and minimums, circulation shape, and front movement.

3.2.4 | Impact of high order interpolation and pressure gradient / divergence (Sets C–H)

The next six sets of simulations (Sets C–H), made using the intermediate resolution of 100 m, odd order O3–17 constant grid advective fluxes, and changes in the order of accuracy of the interpolations and pressure gradient / divergence, were produced to help show which combinations of terms with of higher and lower orders of accuracy produced the best solutions.

The relative change in accuracy for these solutions is described by computing the RMS and L_∞ objective error measures against the reference solution of potential temperature and KE per unit volume, and then computing the percent error differences between the these errors for the test solutions and those for set A (also calculated against the reference solution) at $t = 1000$ s (Fig. 16; percent error differences between the test solutions and those in Set A are computed to more clearly show differences in solution errors that are very close in value; positive numbers mean the errors are better than errors for Set A compared to the reference solution and negative numbers mean worse than Set A). First, the objective errors between solutions made with odd order O3–17 constant grid flux approximations, next higher order /comparable order interpolations, but only O2 pressure gradient / divergence (Set C) at $t = 1000$ s are comparable (or even slightly better at higher orders of accuracy) to solutions with the same order of accuracy in Set A. The appearance of the

perturbation potential temperature fields between Sets A and C (Fig. 17, rows one and two, respectively) have only slight differences at higher orders. These visual differences can be seen in the difference fields between Set C and Set A, 100 m, potential temperature solutions (Fig. 18; $T_{SetA}-T$) with the same order of flux accuracy, as well as in the difference fields between Set C from the O17, 25 m reference solutions (Fig. 19). An examination of the Set C vorticity and deformation fields (Figs. 20 and 21; zoomed as in Figs. 5–9) shows noticeable differences especially in the vicinity of the marginally resolved upper rotor for all orders when compared to Set A solutions. Next, larger objective error measures (Fig. 16), including the largest RMS errors, were found in the simulations with odd order O3–17 constant grid flux approximations, next higher order /comparable order pressure gradient /divergence, but only O2 interpolations (Set D). Notable shape distortion in the upper rotor of the Set D simulations compared to Set A is discernible in the perturbation potential temperature fields (Fig. 17), the difference of potential temperature between the Set A and test (Fig. 18), difference between reference and test solutions (Fig. 19), vorticity (Fig. 20), and deformation fields (Fig. 21).

These first two subsets of experiments, Sets C and D, help show that high order advection is most important for achieving higher accuracy, and that high order interpolations generally are more important than high order pressure gradient / divergence. Interestingly, comparable high order interpolations coupled with low order pressure gradient / divergence approximations had less detrimental effects in terms of solution changes from those in Set A, than high order pressure gradient / divergence approximations coupled with low order interpolations, which is most clearly seen in the difference potential temperature fields from the Set A, 100 m solutions (Fig. 18) and the objective errors (Fig. 16). These effects are most readily seen as differences in locations and magnitudes of potential temperature difference fields in the vicinity of the upper rotor and edges of the outward propagating rotors.

Simulations made with higher order flux approximations coupled with O2 interpolations and O2 pressure gradient / divergence approximations (Set E), which is the typical combination in most atmospheric models, produced worse RMS potential temperature errors for >O9 and worse RMS KE errors for >O5 numerical approximations than Set A. The largest difference errors in Set E were associated with the upper rotor. Importantly, the Set E solutions, along with Set D solutions,

were the most degraded of all solutions discussed in this section, even when they were evaluated against a reference solution made with O17 fluxes and O2 interpolations and pressure gradient / divergence (not shown), which was visually very difficult to distinguish from the reference solution developed for this study.

To be more complete, three sets of simulations were made with odd order upwind-biased O3–17 constant grid advective flux approximations, with either O4, O6 or O18 on both interpolations and pressure gradient / divergence approximation (Sets F, G, and H, respectively). These appeared to be relatively accurate visually (Figs. 17–21, zoomed as in Figs. 5–9; plots for set F are not shown in Figs. 17–21) when compared to Set A, and in some cases for Sets F and G had slightly better objective error measures made against the O17, 25 m reference solution (Fig. 16), especially for the O9, O13, and O17 solutions. The solutions from Sets F–H helped demonstrate that while high order advection was most important to obtaining accurate solutions, high order interpolations and pressure gradient / divergence contribute as well to accurate solutions. Additionally, the solutions from Set F–H showed that slightly more accurate solutions were sometimes possible with marginally reduced orders of advection coupled with higher order interpolations and pressure gradient approximations. As the use of very high order interpolations are the most computationally intensive calculations in the simulations (Fig. 11), the use of comparable order interpolation and pressure gradient / divergence numerical approximations might be considered too costly, but the use at least O4 or O6 for both interpolations and pressure gradient /divergence seems warranted and is perhaps a good compromise.

Consistent with the results of this section, Klemp et al. (2003) demonstrated that their mountain wave simulations, which involved complicated metric terms associated with terrain, were not much different with higher order (O4) spatial numerical approximations for pressure gradient acceleration. However, Klemp et al. did not indicate the order of their interpolations of necessary off-grid point information in the simulations, nor if high order interpolation would help with issues related to amplifying truncation errors owing to unbalanced terrain-related metric terms they described. Nevertheless, the gas dynamics community, especially those in the WENO development community, and perhaps only PL88 in the atmospheric sciences, use higher order interpolations as well as higher order pressure gradient / divergence approximations (e.g., Shu

personal communication to the first author, 2019). In summary, based on the simulations in Sets C–H, better interpolations generally have less impact on solution accuracy than higher order flux / advection, but more impact than higher order pressure gradient / divergence.

3.2.5 | High order turbulent flux approximations with constant eddy mixing (Set I–J)

Interestingly, the use of O4 numerical approximations for SGS turbulent fluxes and interpolations to generate the turbulent fluxes for ≥O9 flux solutions produced the best objective results relative to Set A (see Figs. 16a, b inset) compared to the same using O10 (or even O18; not shown) numerical approximations for the SGS turbulent fluxes, but only by a very slight margin, and only for perturbation potential temperature. In contrast, some of the better objective results relative to set A for KE were achieved using O4–10 (or even O18) numerical approximations for the SGS turbulent fluxes, however, only by a very slight margin, with unknown reasons for the different behaviour of the RMS error. The perturbation potential temperature fields (Fig. 17) for Sets I and J (O4 and O10 SGS turbulent approximations, respectively), difference fields between the perturbation potential temperatures from Set A (Fig. 18), difference fields from the reference solution (Fig. 19), vorticity (Fig. 20) and deformation fields (Fig. 21), show that use of higher order turbulent flux approximations generally has relatively small effects on the solutions. The $L\infty$ errors norms (Fig. 16) and results in Figs. 17–21 for Sets I and J show that higher order turbulent flux approximations slightly damped the perturbation potential temperature field in regions where there were extrema compared to the solutions made with O2 turbulent flux approximations (Set A), which generally had values and especially extrema that were too large when compared to the reference solution, while much of the rest of the solution was much less affected.

In these tests, with 100 m resolution, and O17 constant grid flux, O18 constant grid SGS flux, and 100 m resolution with the constant eddy mixing coefficient, for example, resulted in absolute relative differences of up to ~0.22%, 0.14%, 0.096%, and 0.93% for maximums of perturbation potential temperature, perturbation pressure, u, and w, respectively, at $t = 1000$ s from the O17, Set A simulations, which used O2 numerical approximations for SGS turbulent fluxes, from the complementary simulations using O4–18 constant grid flux approximations for SGS turbulent fluxes. Absolute relative differences for the maximums of the same variables were comparable or smaller at ~0.22%, 0.011%, 0.005%, and 0.024% for the 25 m reference solution resolution. In

addition, the RMS errors for the perturbation potential temperature (KE) for a 33 m, O17 with O18 interpolations, O18 pressure gradient / divergence, and O18 constant grid SGS fluxes against the 25 m reference solution were 3.9% (1.3%) better than the 33 m, O17 flux solution from the Set A simulation showing there is some advantage in terms of accuracy improvement to using higher order SGS fluxes.

Unlike differences between constant grid flux and integrated flux approximations for advection, with the latter producing much larger errors, the use of these two flux formulations for the staggered first derivatives to compute SGS turbulent fluxes interestingly produced small relative differences of only 0.12% (0.11%) for constant grid SGS flux (integrated SGS flux) for maximums of perturbation potential temperatures and ~0.42% (0.088%) for maximums of KE at $t = 1000$ s compared to Set A using O17 fluxes and O18 SGS fluxes. Additionally, the absolute relative differences in RMS errors (based on the O17, 25 m Set A reference solution) between each other (and Set A) and these experiments for perturbation potential temperature and KE were ~0.04% (~0.2%) and ~0.02% (~0.4%), respectively [see Figs. 16–21 for O4 and O10 turbulent flux approximations, labeled as Set I and J, respectively; results for O6–8 and O12–18 turbulent fluxes are not shown], with the biggest changes, occurring between the O2 and O4 order turbulent flux approximations. These RMS error differences are more than 10 times smaller than those for the O17 solutions made with O2 approximations pressure gradient / divergence (Set C), O2 interpolations (Set D), or O2 for both interpolations and pressure gradient / divergence (Set E). Given that high order SGS turbulent fluxes did not change the convergence rates for the solutions it seems unlikely that O2 SGS turbulent fluxes degraded solutions as much as lower order advection.

Presumably the diffusive nature of turbulent fluxes minimizes the differences between solutions with different orders of turbulent fluxes as diffusion operators tend to damp difference errors each time step, whereas convective (advective) operators allow difference errors to propagate and accumulate (personal communication, B. Fornberg, 2019). With such small improvements using higher order SGS turbulent flux numerical approximations, it was concluded they were not generally necessary for accurate solutions, nor were they excessively costly if priorities for a specific problem might benefit from their use. Test solutions (not shown) made with variable eddy

mixing coefficients by solving the TKE equation showed that use of higher order approximations for SGS turbulent fluxes generally led to larger differences than those with constant eddy mixing coefficients, although they were not excessively different.

3.2.6 | Comments on effects of filtering strength and constant eddy mixing

The obvious and simplest, but not always the best, way to control numerically generated high frequency waves when physical solutions are excessively impacted by dispersion/phase errors, aliasing errors, nonlinear physical instabilities, etc., is to add and/or increase the spatial filter coefficient (e.g., Shuman 1957; Shapiro 1970; S82; P87; PL88: Kusaka et al. 2005; K07) and/or eddy mixing (e.g., Anderson 1989; Ooyama 2002). Reducing or increasing the value of the filter parameter α by 400% or a factor of four times smaller ($\alpha = 0.0075$ damping $2\Delta x$ waves 0.75% every time step) or 400% four times larger ($\alpha = 0.12$ damping $2\Delta x$ waves 12 % every time step) than the value used in this paper can potentially have a variety of effects such as under-damping noise or excessively damping the physical solutions (not shown as the focus was not on filters; K07 comprehensively investigated this topic for atmospheric flows using the WRF model using $\alpha = 0.24$, noting they stated they did not advocate using a value as large as 0.24). For the O17, 100 m solutions in this paper, the effects on the maximum, minimum, and RMS errors for perturbation potential temperature and KE at $t = 1000$ s when using the O18 filter and $\alpha = (0.0075; 0.03; 0.12)$ include ~0.2–3.1% and ~0.5% differences in the maximums and minimums and ~0.6–10%, and 0.5% for RMS errors for perturbation potential temperature and KE. Given the relatively minimal impact on the solutions for these large changes in the filter coefficient α, the results in this paper were likely robust and not excessively dependent on the value of α. Strengths of this study were that the filter was the same for all schemes, use of a very high order filter did not degrade low order solutions, and that using a constant filter value for all simulations precluded any solution differences that could have been caused by different filter strengths. A weakness is that the filter orders and filter coefficients could have been 'fine-tuned' for each scheme and resolution, but this was far beyond the scope of this paper.

If instead the constant eddy mixing (which was also a form of filter but was intended to mimic SGS turbulent fluxes in a crude sense) was reduced or increased by only 25% the impact was much more substantial owing to the larger impact on $>2\Delta$ waves by the effectively O2 filter than the

selective high order O18 spatial filters (P87; PL88; K07). For comparison, in the O17, 100 m solutions, the effects on the maximum, minimum and RMS error for perturbation potential temperature and KE at $t = 1000$ s when using $K_m = (7.5; 10; 12.5 \text{ m}^2 \text{ s}^{-1})$ were ~2.6–7.9% and ~2.3% difference for the maximums and minimums and ~12–16% and ~6–12% for RMS errors for perturbation potential temperature and KE. However, the solutions trended toward different solutions in comparison to those solutions made with the three values of α for the O18 spatial filter. Unfortunately, increasing the filter strength or eddy mixing coefficient potentially can adversely smooth resolvable features (e.g., Anderson 1989; K07; WSK22), making assessment and interpretation of the impact of higher order advection and interpolation difficult (e.g., WSK22). On the other hand, proper use of filters can result in much improved solutions. As discussed by P87 and PL88, use of a filter with a lower order than the advection order will reduce the accuracy of solutions, while using higher order filters often can improve the accuracy of solutions.

3.2.7 | Comments on the effects of time differencing

Importantly, the time differencing errors with mode-split RK3 temporal schemes (at best O2 in time for any RK3 nonlinear solutions, as shown theoretically by Baldauf 2010), were perhaps contributing to the small overall convergence rates of the solutions for the nonlinear colliding plumes problem in part, since the best overall convergence rates obtained were typically O1 to O2, as expected. Temporal errors have been shown repeatedly to limit overall convergence of solutions in other similar studies. For example, S93 showed that that they could not attain better than O1 temporal convergence with their nonlinear density current solutions when keeping spatial resolution constant with O2 spatial differencing and using increasingly smaller time steps. Their solutions converged at ~O1 for the Robert–Asselin time-filtered leapfrog, which is theoretically O1 in time, but absolute errors increasingly improved against the solution made with the smallest time step, which served as the reference. Similarly, Park and Lee (2009) showed that their nonlinear rising plume problem converged at the rate of the time schemes they used including ~O3 for the WS02 RK3 scheme and ~O4 for their O4 L1 scheme. They also showed more improvement in temporal convergence rates using higher order time schemes and higher order spatial differencing than the same with lower order spatial differencing. In another study, WSK22 could not achieve better than ~O3 overall convergence for a linear advection problem using O10 spatial differencing and the RK3 scheme, which is O3 in time for linear solutions (Baldauf 2010). High

order overall convergence rates were achieved by G09 and Wu et al. (2021), including O17 overall convergence for an O17 Runge-Kutta time scheme coupled with O17 spatial differencing for a number of linear problems; however, G09 could not achieve overall convergence rates that matched order of accuracy for the spatial differencing for the nonlinear inviscid Burgers' equation as high order RK schemes become O2 for nonlinear problems. By choosing a very small time step with the RK4 time scheme, Wu et al. (2021) was able to achieve overall convergence rates that matched spatial order of accuracy (O3–17) for inviscid nonlinear Burgers' equation solutions, but only when the time step was reduced dramatically by $2^{-(2r-1)/4}$ (where 2r–1 is the order of accuracy, e.g., O17 for r = 9, for the odd order of the spatial scheme) for each halving of spatial resolution so that the temporal errors were roughly the same order as the spatial order of accuracy. Using the approach employed by Wu et al. would have required time steps for O17, 50 m solutions that were ~19 times smaller than time steps used for O17, 100 m solutions in this study, rather than just twice as small.

Unsurprisingly, many including S93, Park and Lee (2009), Wu et al. (2021), WSK22, etc., have found that using smaller time steps than dictated by the CFL typically resulted in more accurate solutions, but not better convergence rates. In the study here, using O17, resolution of 100 m, and time steps that were two and four times smaller than that used in Set A resulted in: solution maximums and minimums (not shown) that were closer to those in the reference simulation than any of the other experiment sets at 100 m resolution; maximum and minimums up to 5.5% better than those in Set A; variable fields that were somewhat less noisy than in Set A; and as much change in solution fields in some cases as in Sets C–J, where impacts of interpolations, pressure gradient / divergence, and SGS turbulent fluxes were compared. Also, as one might expect, the use of a time step 2–9.6 times larger than used in Set A produced maximums and minimums that were further from the reference solution, as well as variable fields that were more distorted and noisier than in Set A. The calculated temporal convergence rates for these experiments were typically ≤O1 for potential temperature, KE, deformation, and vorticity, thus, even though absolute temporal errors were fairly small, they seemingly were not too small to impact overall convergence rates.

A preliminary examination of temporal convergence rates (figures not shown) was made using a subset of simulations employing O9 and O17 numerical approximations, holding spatial resolution constant at ~100 m, systematically reducing the time step (2.4, 1.2, 0.6, 0.2, and 0.1 s), and using the solution with the smallest time step (0.1 s) as the reference. When spatial filters, SGS turbulence, and divergence damping were simultaneously made inactive, the results demonstrated much larger calculated temporal convergence rates of ~O3 (usually slightly larger than O3 and occasionally as large as ~O3.96 with O17 spatial differencing, as others have occasionally noted using higher order spatial schemes with RK3 time schemes), compared to ≤O1 with all of these terms active. These results were consistent ~O3 RK3 temporal convergence rates reported by Park and Lee (2009), which did not include either spatial filtering or SGS turbulence, but did include stronger divergence damping, and were better than expected based on the analysis done by Baldauf (2010). When used without SGS turbulence and divergence damping, the spatial filters, which had a very modest Courant number of ~1×10^{-2}, produced calculated temporal convergence rates ≤O1, compared to ~O2–O3 when the filtering Courant numbers were $1 \times 10^{-4} - 1 \times 10^{-5}$ (i.e., much weaker filter). Additionally, the O2–18 SGS turbulence and O2 divergence damping, which had Courant numbers of ~3×10^{-4} and ~1×10^{-2}, respectively, both individually produced ~O2–O3 calculated temporal convergence rates. The temporal errors with high order flux, and either O2 or high order (≥O4) interpolations and pressure gradient / divergence, did not reduce temporal convergence rates to less than ~O3.

In summary, low temporal convergence rates associated with the spatial filters, and to some degree divergence damping and SGS turbulence terms, had potentially significant negative impacts on overall convergence rates, especially those with the filter, and as a consequence they impacted on the cost effectiveness of high order spatial differencing schemes. In spite of the effect of slowed convergence rates associated with time differencing, the absolute errors for solutions that were the used in this paper were generally small, and the use of increasingly higher order spatial schemes almost always improved objective errors, sometimes by a factor of up to 5–7, compared to the lower order spatial schemes at the same resolution. Finally, in the spirit of Park and Lee (2009), who state "For a lower-accuracy calculation (i.e., larger L2 norm), the [simplified RK3] SRK3 [WS02] scheme is still more efficient. However, for high-accuracy simulations, it may be possible that higher-order time-integration schemes should become efficient at a sufficiently high resolution

and that the R21 and L21 schemes are more efficient than the SRK3 scheme." This perhaps holds for very high order spatial differencing schemes as well, with a hint of this possibly seen in the higher resolution solutions made with ≤33.33 m along with high order ≥O13 numerical approximations, as indicated by some of the L2 and L∞ error norm measures presented herein.

4 | CONCLUSIONS

The main conclusions of this study include the following:

1) the best solutions, based on comparisons with a O17, 25 m reference solution, were attained at most resolutions with the highest order flux schemes, interpolations, and to a lesser extent, pressure gradient / divergence approximations; thus for a given resolution, higher order flux / advection was the most important factor in producing more accurate solutions, followed by high order interpolations, and to a lesser extent high order numerical approximations for pressure gradient / divergence, while high order O4–20 numerical approximations for SGS turbulent fluxes had minimal impact on solutions (although O4–6 SGS turbulent flux approximations may provide some improved accuracy compared to O2 approximations when using constant eddy-mixing coefficients in tests such as those shown in this paper);

2) formal convergence rates were generally limited to at best ~O1–2 for the mode-split RK3 solutions discussed in this paper, regardless of the order of accuracy of the spatial schemes used owing to the strong nonlinearity of the test problem, and perhaps partly to the time scheme, which is theoretically at best O2 for nonlinear, mode-split, RK3 time integration schemes (Baldauf 2010); temporal convergence rates were ≤O1 especially when spatial filters, and to a lesser degree when SGS turbulence and divergence-damping were active, and ~O3 with them turned off, this indicated the possible negative impact of the temporal errors with these terms on overall convergence rates;

3) integrated flux solutions, which were at best O2 for linear problems (T87), were worse both objectively in terms of RMS errors and various error norms, as well as visually, when compared to the constant grid flux solutions for the 2D colliding plumes nonlinear problem;

4) visual appearances and objective error measures, based on an O17, 25 m resolution reference solution, showed that solutions improved with increases in order of numerical approximations for fluxes past O3–7 through O9–17, with the most visual and objective error improvement achieved with increasing the overall order from O3 to O5, followed by O5 to O9, and so on, although improvement was grid-resolution dependent for the test problem;

5) higher order numerical approximations improved the representation of circulation structures and shapes, phase, amplitudes, and overall accuracy of kinematic aspects of flows, such as KE, deformation, and vorticity, for all of the resolutions used in the simulations of the test problem;

6) improving the order of accuracy of pressure gradient / divergence could not compensate (except perhaps marginally) for low order of accuracy of flux / advection;

7) the inherent amplitude errors and diffusive nature associated with upwind-biased flux schemes (larger than next higher even order schemes) were increasingly less noticeable with increasingly higher order numerical approximations (T87);

8) some theoretically cost-effective solutions in terms of FPOs, assuming the same Courant number, were found between finer resolution O3 and next coarser resolution ≥O5 solutions, as well as some of the finer resolution O9, O13, and O17 solutions; however, the intermediate resolution O5 and next coarser resolution O9 solutions were at best cost-comparable;

9) the diffusion-limited nature of the nonlinear colliding plumes test problem, as well as time scheme errors, (especially when coupled with SGS turbulence, spatial filtering, and divergence damping, which increased overall absolute errors and diminished temporal convergence rates to <O1 from ~O2, at least partially, if not wholly), compromised cost-effectiveness of the flux solutions made with <O13 numerical accuracy if the CFL-based time step for each order of accuracy was considered, in comparison to previous studies that utilized non-viscous or weakly viscous solutions;

10) employing CPU times instead of theoretical FPOs improves the estimates of cost-effectiveness for many solutions through efficient computer cache memory use, noting that CPU times are machine sensitive, while FPOs are not.

The main limitations of this work include the following:

1) the test problem used might not have been challenging enough to the numerical schemes;

2) only one value of constant turbulent eddy mixing coefficient was considered (simulations not shown with $K_m = 4$ m^2 s^{-1} contained more fine-scale detail);

3) all of the possible combinations of orders or accuracy for advection, interpolations (including different interpolation schemes), and pressure gradient / divergence were not examined, reported, and/or attempted;

4) objective error measure accuracy might possibly be weakened by interpolating solutions on a staggered grid using O2 bilinear interpolation;

5) power spectra were not yet analyzed; they can show whether or not smaller scale waves have more KE power with higher rather than lower order schemes, which would indicate that smaller scale features are being better resolved (e.g., Skamarock 2004; P15; N21; Wang 2021; Zhang 2022), and with further analysis could also reveal dispersion and dissipation properties of nonlinear schemes (Zhang et al. 2022);

6) collapsing numerical approximations (lower order accuracy) near the lower and upper boundaries were likely affecting solutions, but this could be averted to some degree with inverse Lax-Friedrich type approaches (Tan and Shu 2010, 2013; personal communication Shu 2019) or mirror conditions at the vertical boundaries (mirror conditions are not practical for numerical weather prediction with surface fluxes);

7) the use of unstretched grids likely limited the relative importance of high order interpolations for computing off-grid point information and fluxes, the former which are often computed with simple averaging, but not always, especially in the vertical (e.g., the CM1 model; Bryan 2021);

8) the degree of conservation of passive scalars, momentum, mass, energy, etc. was not evaluated [experiments comparing two or more passive scalars and their sum would have provided more insight concerning the behaviours of schemes for cases with many scalar variables that are dependent on each other (e.g., mixing ratio and concentration of precipitation, or mixing ratio of rain and snow compared to total mixing ratio and snow)];

9) the short simulation times may not have allowed full appreciation of the production of better solutions with higher order advective fluxes, interpolations, and pressure gradient / divergence numerical approximations; and

10) monotonic operators were not extensively tested as a method to reduce overshoots as their use is beyond the scope of this study; however, a preliminary test with the 100 m solutions was done to test Leonard's (1991) monotonic operator (not shown), which showed that while the monotonic operator did indeed keep the solutions monotonic, they were much less accurate compared to the O17, 25 m reference solution.

Future work should include consideration of

1) other types of both odd and even high order flux schemes and other forms of interpolations, for both uniform and stretched grids;

2) the effect of collapsing order of accuracy of numerical approximations as boundaries are approached, especially when near-boundary interactions are important, such in atmospheric boundary layer simulations with strong surface fluxes or in other flows with rigid physical boundaries (e.g., pipe flows, etc.);

3) the impact of time differencing errors on overall convergence (although usually considered negligible), especially in simulations with SGS-turbulence, spatial filtering, and divergence damping;

4) the importance of interpolations and flux approximations using stretched grid-based coefficients should be considered (initial work shows that at least interpolation for off-grid information becomes more important for improved accuracy for more stretched grids); and

5) consideration of complicated problems, including those with parameterised physical processes (e.g., turbulence, microphysics, radiation, etc.), to determine if these might result in any offset in the improvements obtained by the use of higher order advection, pressure gradient / divergence / interpolation and/or could interact in unexpected, or perhaps, nonlinear ways.

In summary, very high odd order (O9–17) upwind-biased constant grid advective flux schemes coupled with high order interpolation, pressure gradient / divergence numerical and SGS turbulent fluxes approximations, both visually and objectively produced the most accurate solutions for the experiments presented in this paper. We conclude that O9–17 flux schemes, coupled with at least ≥O4 high-order interpolation, and to a lesser extent ≥O4 SGS turbulent fluxes and pressure gradient / divergence, can produce high quality solutions, and have the potential to perform better in terms of objective measures than O3–7 advective flux schemes, coupled with commonly used O2 interpolations, pressure gradient / divergence, and SGS turbulent fluxes limited-area atmospheric models, without being a computational burden.

AUTHOR CONTRIBUTIONS

Jerry Straka: Conceptualization; formal analysis; investigation; methodology; software; validation; visualisation; writing – original draft; writing – review and editing. Paul D. Williams: Conceptualization; investigation; methodology; writing – review and editing. Katharine Kanak: Conceptualization; formal analysis; methodology; investigation; visualisation; writing – review and editing.

DATA AVAILABILITY STATEMENT

All data and codes are available from authors. There are no conflicts of interest or funding statements to report.

SUPPORTING INFORMATION LIST

Supporting Information Table S1: 3D Compressible model physics and numerical approximations, along with model equation set documentation.

Supporting Information Table S2a–d: Finite difference, interpolation, and filter coefficients

Supporting Information Table S3a–b: Calculated convergence rates for interpolations and linear accelerations computed with various orders of numerical accuracy

Supporting Information Figure S4: Perturbation potential temperature (K) for all 25 to 200 m solutions, as in Fig. 2

Supporting Information Figure S5: Kinetic energy (KE) per unit volume for all 25 to 200 m solutions, as in Fig. 2

Supporting Information Figure S6: Perturbation potential temperature (K) for all O17 advective flux solutions made with 25 to 200 m solutions and O18 accurate constant grid flux SGS turbulent flux and O18 accurate integrated flux SGS turbulent flux. Differences from O2 accurate SGS turbulent flux are also shown.

Supporting Information Table S7: Calculated convergence rates for interpolations and linear accelerations computed with various numerical orders of accuracy

Supporting Information Figure S8: Perturbation potential temperature (K) solutions for Set A.IF using integrated advective flux approximations and 25 to 166.66 m resolution, as in Fig. 4, except Fig. 4 uses constant grid flux

REFERENCES

Anderson, J.R. (1989) A local, minimum aliasing method for use in nonlinear models. *Monthly Weather Review*, 117, 1369–1379.

Arakawa, A. and V.R. Lamb (1977) Computational design of the basic dynamical processes of the UCLA General Circulation Model. *Methods Computational Physics*, 17, 173–265, http://dx.doi.org/10.1016/B978-0–12–460817-7.50009–4.

Balsara, D.S. and Shu, C.-W. (2000) Monotonicity reserving weighted essentially non-oscillatory schemes with increasing high order of accuracy. *Journal of Computational Physics*, 160, 405–452.

Baldauf, M. (2008) Stability analysis for linear discretisations of the advection equation with Runge–Kutta time integration. *Journal of Computational Physics,* 227 (2008), 6638–6659. doi:10.1016/j.jcp.2008.03.025

Baldauf, M. (2010) Linear stability analysis of Runge–Kutta-based partial time-splitting schemes for the Euler equations. *Monthly Weather Review*, 138(12), 4475–4496. https://doi.org/10.1175/ 2010MWR3355.1.

Bott, A. (1989) A positive definite advection scheme obtained by nonlinear renormalization of the advective fluxes. *Monthly Weather Review*, 117, 1006–1015.

Boyd, J.P. (1994) Sum-accelerated pseudospectral methods: Finite differences and sech-weighted differences. *Computer Methods in Applied Mechanics and Engineering*, 116, 1–11.

Boyd, J.P. (2001) *Chebyshev and Fourier Spectral Methods*. Second Edition. New York: Dover.

Bryan, G.H. (2021) The governing equations for CM1. UCAR Tech. Note, 30 pp. https://www2.mmm.ucar.edu/people/bryan/cm1/cm1_equations.pdf.

Bryan, G.H. and Fritsch, J.M. (2002) A benchmark simulation for moist nonhydrostatic numerical models. *Monthly Weather Review*, 130(12), 2917–2928. https://doi.org/10.1175/ 1520-0493(2002)130<2917:ABSFMN>2.0.CO;2.

Conte, S.D. and de Boor, C. (1980) *Elementary Numerical Analysis, An Algorithmic Approach*, Third Edition. McGraw-Hill Book Company, 432 pp. ISBN 0-07-012447-7

Costa, A.A. and Sampio, A.J.C. (1997) Bott's area-preserving flux-form advection algorithm: Extension to higher orders and additional tests. *Monthly Weather Review*, 125, 1983–1989.

Cotton, W.R., Bryan, G. and van den Heaver, S. (2011) Storm and Cloud Dynamics, 2nd ed., Academic, Burlington, Mass.

Crowley, W.P. (1968) Numerical advection experiments. *Monthly Weather Review.*, 96, 1–11, https://doi.org/10.1175/1520-0493(1968)096<0001:NAE>2.0.CO;2.

Deardorff, J.W. (1980) Stratocumulus-capped mixed layers derived from a three-dimensional model. *Boundary-Layer Meteorology*, 18(4), 495–527. https://doi.org/10.1007/BF00119502.

Desjardins, O., Blanquart, G., Balarac, G. and Pitsch, H. (2008) High order conservative finite difference scheme for variable density low Mach number turbulent flows. *Journal of Computational Physics*, *227*(15), 7125–7159. https://doi.org/10.1016/j.jcp.2008.03.027

Durran, D.R. (2010) *Numerical Methods for Fluid Dynamics*. Second Edition. New York: Springer-Verlag.

Fjortoft, R. (1953) On the changes in spectral distribution of kinetic energy for two dimensional nondivergent flow. *Tellus*, 5, 225–230. DOI: 10.3402/ tellusa.v5i3.8647.

Fornberg, B. (1975) On a Fourier method for the integration of hyperbolic equations. *SIAM Journal on Numerical Analysis*, 12, 509–528.

Fornberg, B. (1987) The pseudospectral method: Comparisons with finite differences for the elastic wave equation. *Geophysics*, 52, 483–501.

Fornberg, B. (1988) Generation of finite difference formulas on arbitrarily spaced grids. *Mathematics of Computation*, 51, 699–706.

Fornberg, B. (1990) High order finite differences and the pseudospectral method on staggered grids. *SIAM Journal on Numerical Analysis*, 27, 904–918.

Fornberg, B. (1996) A Practical Guide to Pseudospectral Methods. Cambridge University Press, Cambridge, ISBN–13: 978-0521645645, ISBN–10: 0521645646.

Gadd, A.J. (1980) Two refinements of the split explicit integration scheme. *Quarterly Journal of the Royal Meteorological Society*, 106, 215–220, https://doi.org/10.1002/qj.49710644715.

Grabowski, W.W. and Clark, T.L. (1991) Cloud–environment interface instability: rising thermal calculations in two spatial dimensions. Journal of the Atmospheric Sciences, 48(4), 527–546. https://doi.org/10.1175/1520-0469(1991)048<0527:CIIRTC>2.0. CO;2.

Gerolymos, G.A., Sénéchal, D. and Vallet, I. (2009) Very-high order WENO schemes. *Journal of Computational Physics*, 228, 8481–8524.

Gerrity, J.F. Jr. (1976) The LFM model 1976: A documentation. NOAA Tech. Memo. NWS NMC 60, NMC, Washington, DC, 68 pp.

Haltiner, G.J and Williams,R.T. (1980) *Numerical Prediction and Dynamical Meteorology*. John Wiley and Sons, Inc. 477 pp. ISBN 0-471-05971-4.

Henrick, A.K., Aslam, T.D., Powers, J.M. (2005) Mapped weighted essentially non-oscillatory schemes: Achieving optimal order near critical points. Journal of Computational Physics, 207, 42-567. 10.1016/j.jcp.2005.01.023

Jameson L. (2000) High order schemes for resolving waves: Number of points per wavelength. *Journal of Scientific Computing*, 15, 417–439.

Kalnay, E. and Hoitsma, D. (1979) Documentation of the Fourth Order Band Model. NASA Tech, Memo. 80606, Goddard Space Flight Center, Silver Spring, Maryland 20771. 116 pp.

Kaplan, M.L, Zack, J.W., Wong, V.C. and J.T. Tuccillo, J.T. (1982) Initial results for a Mesoscale Atmospheric Simulation System and comparisons with the AVE-SESAME I data set. *Monthly Weather Review*, 110, 1564–1590.

Klemp, J.B., Skamarock, W.C. and Fuhrer, O. (2003) Numerical consistency of metric terms in terrain-following coordinates, *Monthly Weather Review*, 130 (7), 1229–1239. https://doi.org/10.1175/1520-0493(2003)131<1229:NCOMTI>2.0.CO;2.

Klemp, J. B. and Wilhelmson, R. B. (1978) The simulation of three-dimensional convective storm dynamics. *Journal of Atmospheric Sciences*, **35**, 1070–1096. https://doi.org/10.1175/1520-0469(1978)035<1070:TSOTDC>2.0.CO;2.

Knievel, J.C., Bryan, G.H. and Hacker, J.P. (2007) Klemp, J.B. and Wilhelmson, R.B. (1978) The simulation of three-dimensional convective storm dynamics. *Journal of the Atmospheric Sciences*, 35(6), 1070–1096. https://doi.org/10.1175/ 1520-0469(1978)035<1070:TSOTDC>2.0.CO;2.

Kosović, B., 1997: Subgrid-scale modelling for the large-eddy simulation of high-Reynolds-number boundary layers. *Journal of Fluid Mechanics*, 336, 151–182.

Kreiss H.O. and Oliger J. (1972) Comparison of accurate methods for the integration of hyperbolic equations. *Tellus*, 24, 199–215.

Kusaka, H., Crook, A., Knievel, J.C. and Dudhia, J. (2005) Sensitivity of the WRF model to advection and diffusion schemes for simulation of heavy rainfall along the Baiu Front. *Scientific Online Letters On The Atmosphere*, 1 (12), 177–180. doi:10.2151/sola.2005-046.

Latini, M., O. Schilling and Don, W.S. (2007) Effects of WENO flux reconstruction order and spatial resolution on reshocked two-dimensional Richtmyer–Meshkov instability. *Journal of Computational Physics*, 221, 805–836, https://doi.org/10.1016/j.jcp.2006.06.051.

Leonard, B.P. (1991) The ULTIMATE conservative difference scheme applied to unsteady one-dimensional advection. *Computational Methods in Applied Mechanics and Engineering*, 88, 17–74.

Lian, Y, Richardson, M.I., Newman, C.E., Lee, C., Toigo, A., Guzewich, S. and Yelle, R.V. (2022) Dynamical core damping of thermal tides in the Martian atmosphere. *Journal of the Atmospheric Sciences*, 80, 535-546.

Merilees, P.A. and Orzag, S.A. (1979) The pseudospectral method. In: Numerical Methods Used in Atmospheric Models, GARP Publication Series No. 17, Vol. II, World Meteorological Organization, Geneva, pp 276–299.

Mesinger, F. (1977) Forward–backward scheme, and its use in a limited-area model. *Beiträge zurPhysik der Atmosphäre (Contributions to Atmospheric Physics)*, 50, 200–210.

Mirocha, J.D., Lundquist, J.K. and Kosović, B. (2010) Implementation of a nonlinear subfilter turbulence stress model for large-eddy simulation in the Advanced Research WRF model. Monthly Weather Review, 138, 4212 – 4228.

Morrison, H. and Bryan, G.H. (2012) Sensitivity of a simulated squall line to horizontal resolution and parameterization of microphysics. *Monthly Weather Review* 140, 202–225. doi: 10.1175/MWR-D–11-00046.1.

Norman, M.R. (2021) A high-order WENO-limited finite-volume algorithm for atmospheric flow using the ADER-differential transform time discretization. *Quarterly Journal of the Royal Meteorological Society*, 147, 1661–1690. https://doi.org/10.1002/qj.3989

Ooyama, K.V. (2001) A dynamic and thermodynamic foundation for modeling the moist atmosphere with parameterized microphysics. *Journal of the Atmospheric Sciences*, 58 (8), 2073–2102.

Ooyama, K.V. (2002) The cubic-spline transform method: Basic definitions and tests in a 1D single domain. *Monthly Weather Review*, 130 (10), 2392–2415. https://doi.org/10.1175/1520-0493(2002)130<2392:TCSTMB>2.0.CO;2.

Ovtchinnikov, M. and R.C. Easter (2009) Nonlinear advection algorithms applied to interrelated tracers: Errors and implications for modeling aerosol–cloud interactions. *Monthly Weather Review*, 137 (2), 632–644. https://doi.org/10.1175/2008MWR2626.1.

Pardo, L.H, Morrison, H., Lauritzen, P.H. and Pöhlkera, M. (2022) Impact of advection schemes on tracer inter-relationships in large-eddy simulations of deep convection *Monthly Weather Review*, 150 (10), 2765–2785. https://doi.org/10.1175/MWR-D–22-0025.1.

Park, S.-H. and Lee, T.-Y. (2009) High-order time-integration schemes with explicit time-splitting methods. *Monthly Weather Review*, **137**, 4047–4060. https://doi.org/10.1175/2009MWR2885.1.

Pressel, K.G., Kaul, C.M., Schneider, T., Tan, Z. and Mishra, S. (2015) Large-eddy simulation in an anelastic framework with closed water and entropy balances. *Journal of Advances in Modeling Earth Systems*, 7, 1425–1456. doi:10.1002/ 2015MS000496.

Purser, R.J. (1987) The filtering of meteorological fields. *Journal of Applied Meteorology and Climatology*, 26, 1764–1769. https://doi.org/10.1175/1520-0450(1987)026<1764:TFOMF>2.0.CO;2.

Purser, R.J. and Leslie, L.M. (1988) A semi-implicit, semi-Lagrangian finite difference scheme using high order spatial differences on a nonstaggered grid. *Monthly Weather Review*, 116, 2069–2080.

Richtmyer, R.D. and Morton, K.W. (1994) *Difference Methods for Initial-Value Problems*. Second Edition. Krieger, 420 pp. ISBN–10: 0894647636, ISBN–13: 978-0894647635.

Sari, M., Gürarslan, G. and Zeytinoğlu, A. (2010) High-order finite difference schemes for solving the advection-diffusion equation. *Mathematical and Computational Applications*, 15(3), 449–460. https://doi.org/10.3390/mca15030449

Schlesinger, R.E. (1985) Effects of upstream-biased third order space correction terms on multidimensional Crowley advection schemes. *Monthly Weather Review*, 113(7), 1109–1130. https://doi.org/10.1175/1520-0493(1985)113<1109:EOUBTO> 2.0.CO;2.

Shapiro, R. (1970) Smoothing, filtering, and boundary effects. *Reviews of Geophysics*, 8(2), 359–387. https://doi.org/10.1029/ RG008i002p00359.

Shen, Y. and Zha, G. (2010) Large eddy simulation using a new set of sixth order schemes for compressible viscous terms. *Journal of Computational Physics*, *229*(22), 8296–8312. https://doi.org/10.1016/j.jcp.2010.07.017

Shi, J, Zhang, Y.-T. and Shu, C.-W. (2003) High order WENO schemes for complicated flow structures. *Journal of Computational Physics*, 186, 690–691.

Shu, C.-W. (1997) Essentially Non-Oscillatory and Weighted Essentially Non-Oscillatory Schemes for Hyperbolic Conservation Laws. NASA/CR-97–206253 ICASE Report No. 97-65. 79 pp.

Shu, C.-W. (2003) High order finite difference and finite volume WENO schemes and discontinuous Galerkin methods for CFD. *International Journal of Computational Fluid Dynamics*, 17, 107–118, https://doi.org/ 10.1080/1061856031000104851.

Shu, C.-W. (2020). Essentially non-oscillatory and weighted essentially non-oscillatory schemes. *Acta Numerica* (2020), pp. 1–63, Cambridge University Press, 2020, doi:10.1017/S09624929XXXXXX. Printed in the United Kingdom

Shuman, F.G. (1957) Numerical methods in weather prediction. II: Smoothing and filtering. *Monthly Weather Review*, 85(11), 357–361. https://doi.org/10.1175/1520-0493 (1957)085<0357:NMIWPI>2.0.CO;2.

Skamarock, W.C. (2004) Evaluating mesoscale NWP models using kinetic energy spectra. *Monthly Weather Review*, 132, 3019–3032.

Skamarock, W.C. and Klemp, J.B. (1992) The stability of time-split numerical methods for the hydrostatic and the nonhydrostatic elastic equations. *Monthly Weather Review*, 120(9), 2109–2127. https://doi.org/10.1175/1520-0493(1992)120<2109:TSOTSN> 2.0.CO;2.

Soong, S.-T. and. Ogura, Y. (1973) A comparison between axisymmetric and slab-symmetric cumulus models. *Journal of the Atmospheric Sciences*, 30, 879–893

Straka, J.M. and Anderson, J.R. (1993) Extension and application of a local, minimum aliasing method to multidimensional problems in limited-area domains. *Monthly Weather Review*, 121, 2903–2918, https://doi.org/10.1175/1520-0493(1993)121<2903:EAAOAL>2.0.CO;2. rso

Straka, J.M., Wilhelmson, R.B., Wicker, L.J., Anderson, J.R. and Droegemeier, K.K. (1993) Numerical solutions of a non-linear density current: A benchmark solution and comparisons. *International Journal for Numerical Methods in Fluids*, 17(1), 1–22. https://doi.org/10.1002/fld.1650170103.

Tan, S. and Shu, C.-W. (2010) Inverse Lax-Wendroff procedure for numerical boundary conditions of conservation laws. *Journal of Computational Physics*, 229, 8144–8166, https://doi.org/10.1016/j.jcp.2010.07.014.

Tan, S. and Shu, C.-W. (2013) Inverse Lax–Wendroff Procedure for Numerical Boundary Conditions of Hyperbolic Equations: Survey and New Developments. *Advances in Applied Mathematics, Modeling, and Computational Science*, R. Melnik and I.S. Kotsireas, Eds., Vol. 66 of *Fields Institute Communications*, Springer US, 41–63.

Tremback, C.J., Powell, J., Cotton, W.R. and Pielke, R.A. (1987) The forward–in-time upstream advection scheme: extension to higher orders. *Monthly Weather Review*, 115(2), 540–555. https://doi.org/10.1175/1520-0493(1987)115<0540:TFTUAS> 2.0.CO;2.

Tripoli, G.J. and Cotton, W.R. (1980) A numerical investigation of several factors contributing to the observed variable intensity of deep convection over South Florida. *Journal Applied Meteorology,* 19(9), 1037–1063.

Tripoli, G.J. (1992) A nonhydrostatic mesoscale model designed to simulate scale interaction. *Monthly Weather Review*, 120(7), 1342–1359. https://doi.org/10.1175/1520-0493(1992)120<1342:ANMMDT>2.0.CO;2.

Wang., Z.J, Fidkowski, K., Abgrall, R., Bassi, F., Doru, C., Cary, A., Deconinck, H., Hartmann, R., Hillewaert, Huynh, H.T., Kroll, N., May, G., Perrson, P.-O., van Leer, B. and Visbal, M. (2013) Review Article: High order CFD methods: Current status and perspective. International *Journal for Numerical Methods in Fluids*, 72 (8), 811–845. https://doi.org/10.1002/fld.3767

Wang, A., Pan, Y. and Markowski, P.M. (2021) The influence of WENO schemes on large-eddy simulations of a neutral atmospheric boundary layer. *Journal of the Atmospheric Sciences*, 78, (12), 3613–3628. DOI: https://doi.org/10.1175/JAS-D–21-0033.1.

Wicker, L.J. and Skamarock, W.C. (2002) Time-splitting methods for elastic models using forward time schemes. *Monthly Weather Review*, 130(8), 2088–2097. https://doi.org/10.1175/ 1520-0493(2002)130<2088:TSMFEM>2.0.CO;2.

Williams, P.D., Straka, J.M. and Kanak, K.M. (2022) The performance of filtered leapfrog schemes in benchmark simulations. *Quarterly Journal of the Royal Meteorological Society*, 148, 784–808. https://doi.org/10.1002/qj.4231.

Wu, C., Wu, L., Li, H. and Zhang S. (2021) Very high order WENO schemes using efficient smoothness indicators. *Journal of Computational Physics*, 432, 110158. https://doi.org/10.1016/j.jcp.2021.110158

Wyngaard, J.C. (2004) Toward numerical modeling in the "terra incognita". *Journal of Atmospheric Sciences*, 61, 1816–1826. https://doi.org/10.1175/1520-0469(2004)061<1816:TNMITT>2.0.CO;2

Xue, M. (2000) High order monotonic numerical diffusion and smoothing. *Monthly Weather Review*, 128(8), 2853–2864. https://doi.org/10.1175/1520-0493(2000)128<2853:HOMNDA>2.0.CO;2.

Xue, M. and Lin, S.J. (2001) Numerical equivalence of advection in flux and advective forms and quadratically conservative high order advection schemes. *Monthly Weather Review*, 129, 561–565.

Zhang, Y.-T., Shi, J., Shu, J.-W. and Zhou, Y., (2003) Numerical viscosity and resolution of high-order weighted essentially nonoscillatory schemes for compressible flows with high Reynolds numbers. *Physical Review,* E 68, 046709.

Zhang, X., Huang, L., Jiang, Z. and Yan, C. (2022) A class of high-order improved fast weighted essentially non-oscillatory schemes for achieving optimal order at any critical points. *Physics of Fluids,* **34**, 126102 (2022); https://doi.org/10.1063/5.0128716
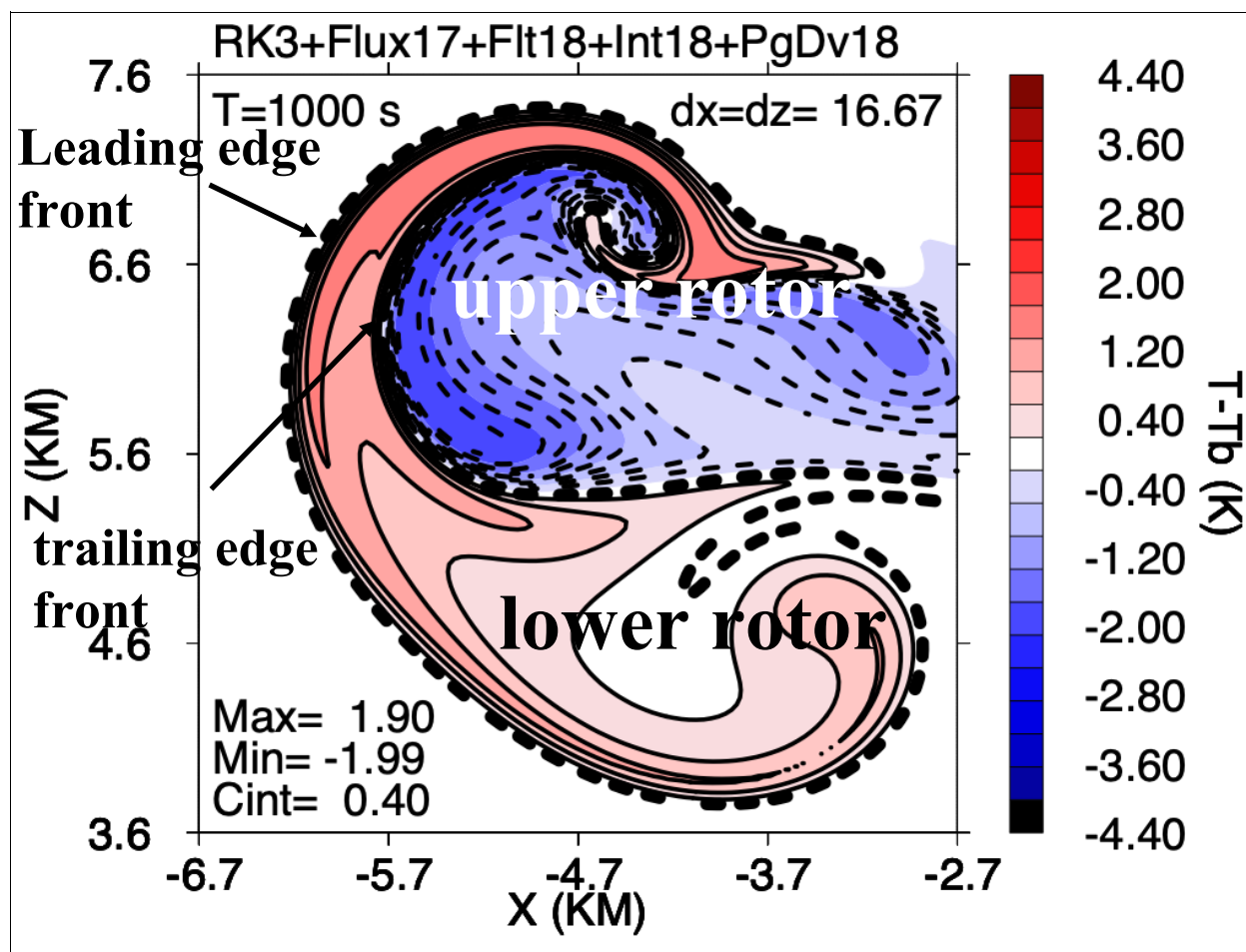
Appendix A. Locations of flow structures in the perturbation potential temperature field for the colliding plumes circulation in a solution made with O17 constant grid fluxes, O18 interpolations and pressure gradient / divergence, O18 spatial filter, and constant eddy mixing coefficient of K_m = 10 m^2 s^{-1} using $\Delta x = \Delta z$ = 16.67 m.
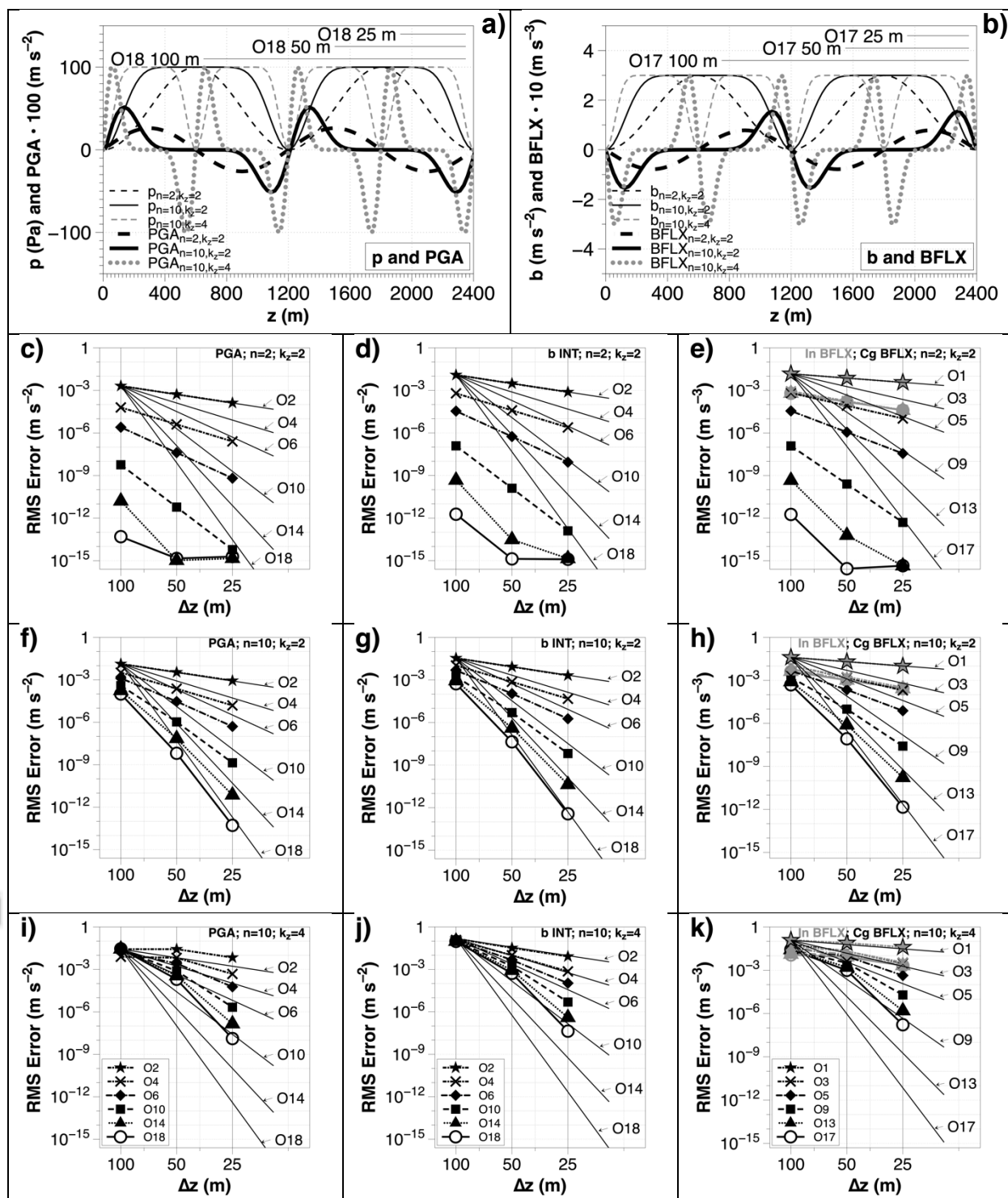
FIGURE 1. Analytical function for pressure (p; kg m^{-1} s^{-2}) and pressure gradient acceleration (PGA m s^{-2}; panel a), buoyancy acceleration function (b; m s^{-2}) and buoyancy flux divergence (BFLX m s^{-3}; panel b). The spatial width of the O18 (panel a) and O17 (panel b) stencils for 25, 50, 100 m grid resolutions also are provided. The second, third, and fourth rows have, from left to right, Root Mean Square (RMS) errors for Δz = 25, 50, and 100 m and orders for PGA,

interpolation of b (b INT), and integrated advective flux for b (In BFLX) and constant grid advective flux for b (Cg BFLX). Subscript symbol n denotes the power of the analytical function, $k_z = 2$ for $L_z = 1200$ m, and $k_z = 4$ for $L_z = 600$ m. Second row results are for $n = 2$ and $k_z = 2$, third row, n = 10, $k_z = 2$, and bottom row, $n = 10$ and $k_z = 4$.
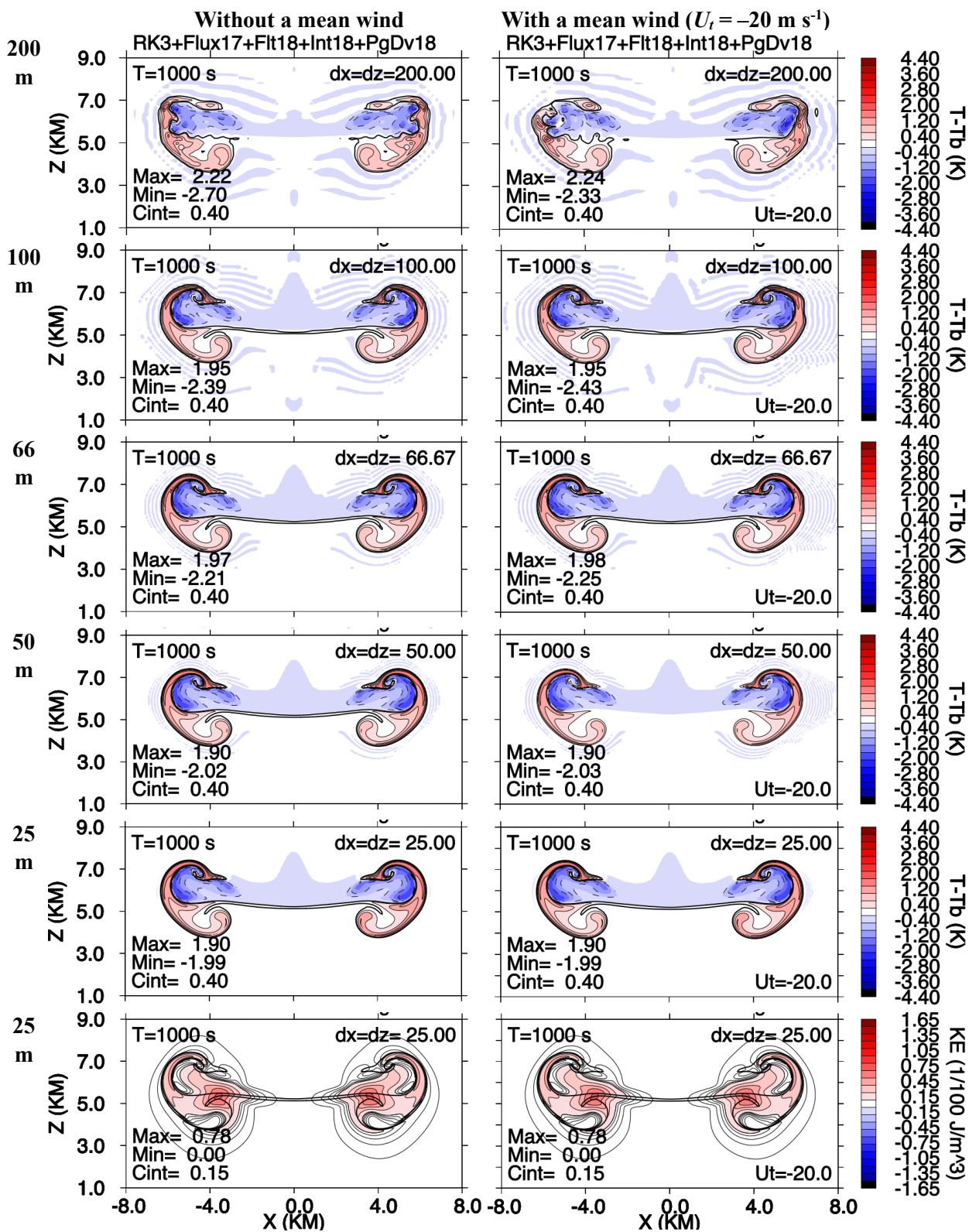
FIGURE 2. Sets A and B perturbation potential temperature ($T - T_b$; K) fields at $t = 1000$ s using $\Delta x = \Delta z = 200, 100, 66.67, 50,$ and 25 m for simulations made with odd order O17 upwind-biased

constant grid advective flux schemes, O18 interpolations and pressure gradient / divergence, same O18 spatial filter, same Courant number, and same constant eddy mixing coefficient of $K_m = 10$ m^2 s^{-1}. Additionally, the O17 kinetic energy per unit volume (KE; J m^{-3}) using $\Delta x = \Delta z = 25$ m is shown in the last row. The left and right columns have simulations made without (Set A; left), and with (Set B; right), an added mean wind $U_t = -20$ m s^{-1}. Maximum (Max), minimum (Min), and contour interval (Cint) values are on each plot, as is $U_t = -20$ m s^{-1} for simulations with an added mean wind ($U_t = 0$ m s^{-1} is omitted for the simulations without an added mean wind). The bold solid line is the 0.2 K perturbation potential temperature contour of the simulation in the plot. Only a sub-domain from $x = -8$ to 8 km and $z = 1$ to 9 km is shown. See Supporting Information S4 and S5 for a plot with all resolutions used between 200 m and 25 m for both perturbation potential energy and KE, respectively.
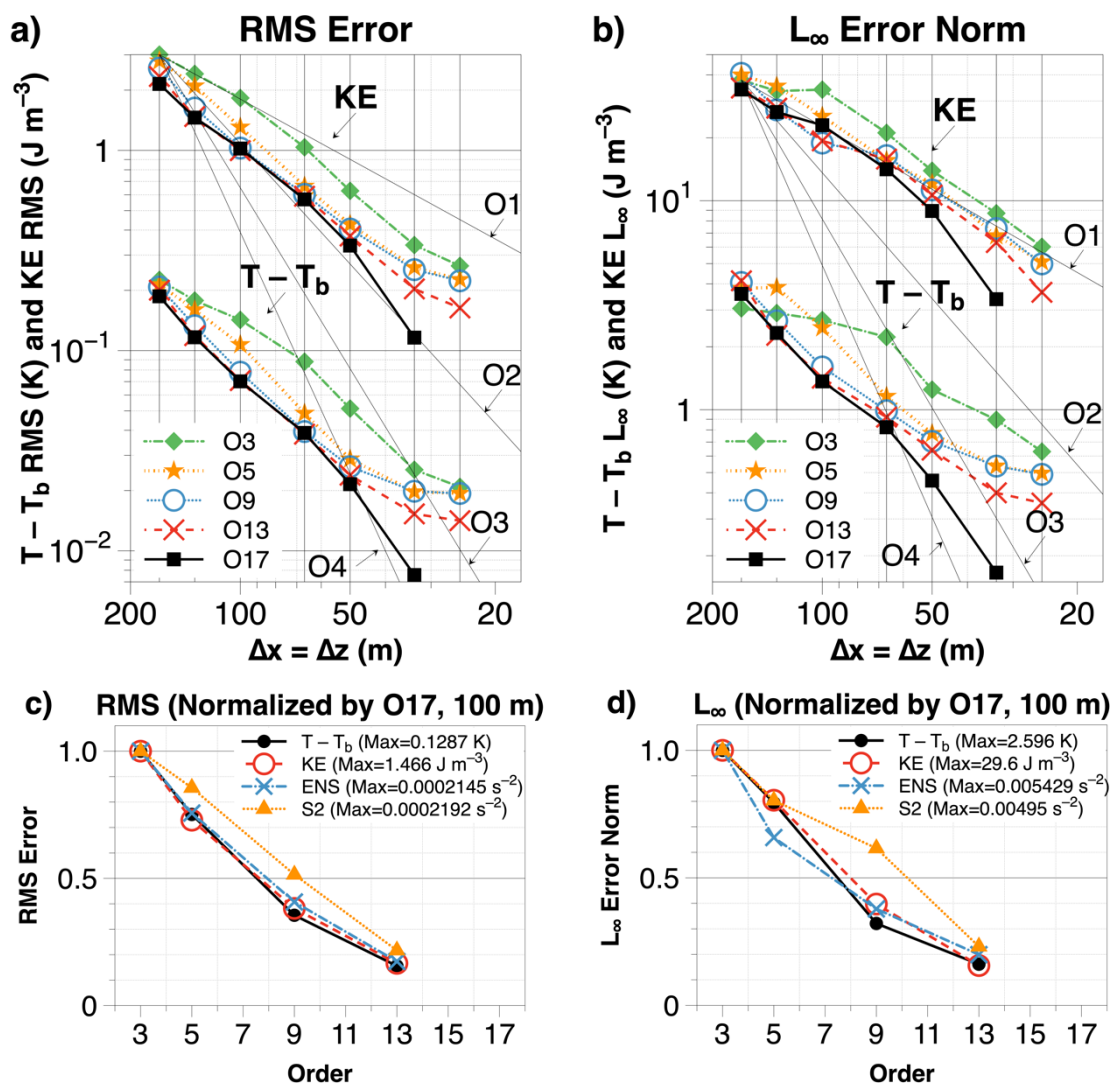
FIGURE 3. Set A objective error measures. a) Perturbation potential temperature ($\theta' = T - T_b$) Root Mean Square error (RMS; K) and Kinetic Energy per unit volume (KE) RMS error (J m^{-3}) of the O3, 5, 9, 13, and 17 test solutions versus resolution $\Delta x = \Delta z$ (m) and b) θ' L_∞ error norm (K) and KE L_∞ error norm (J m^{-3}) versus resolution $\Delta x = \Delta z$ (m) calculated against the O17, 25 m reference solution. In the two lower graphs c) shows normalized RMS error and d) shows normalized L_∞ error norm. The RMS errors and L_∞ error norms are normalised to unity by the maximum value for each variable (shown in parentheses in legends) in order to plot all the curves on a common y-axis for ease of comparison for θ' (K), KE (J m^{-3}), enstrophy (ENS; s^{-2}), and deformation squared (S2; s^{-2}) versus order for the O3, 5, 9, and 13, $\Delta x = \Delta z$ =100 m test solutions calculated against the O17, 100 m solution.
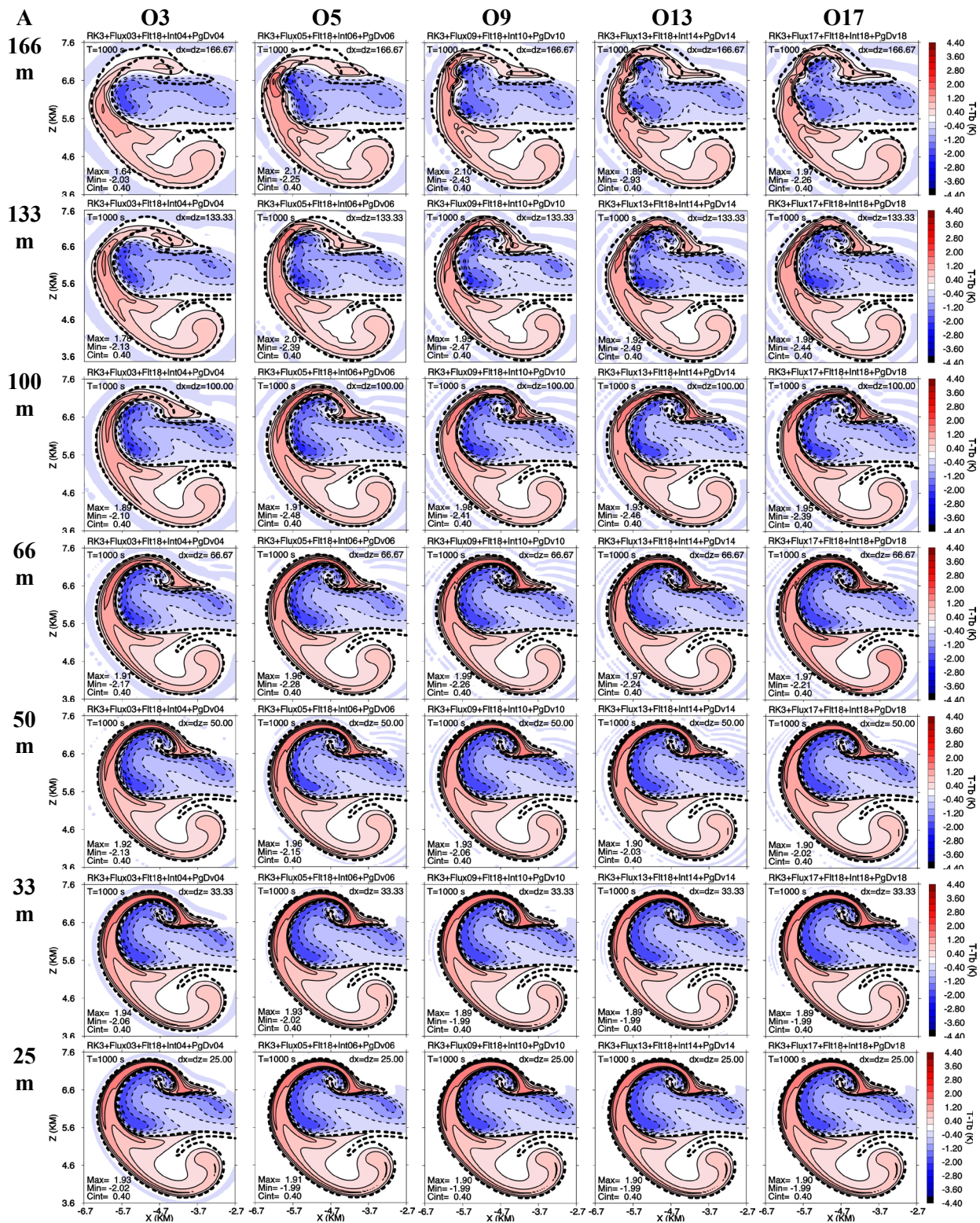
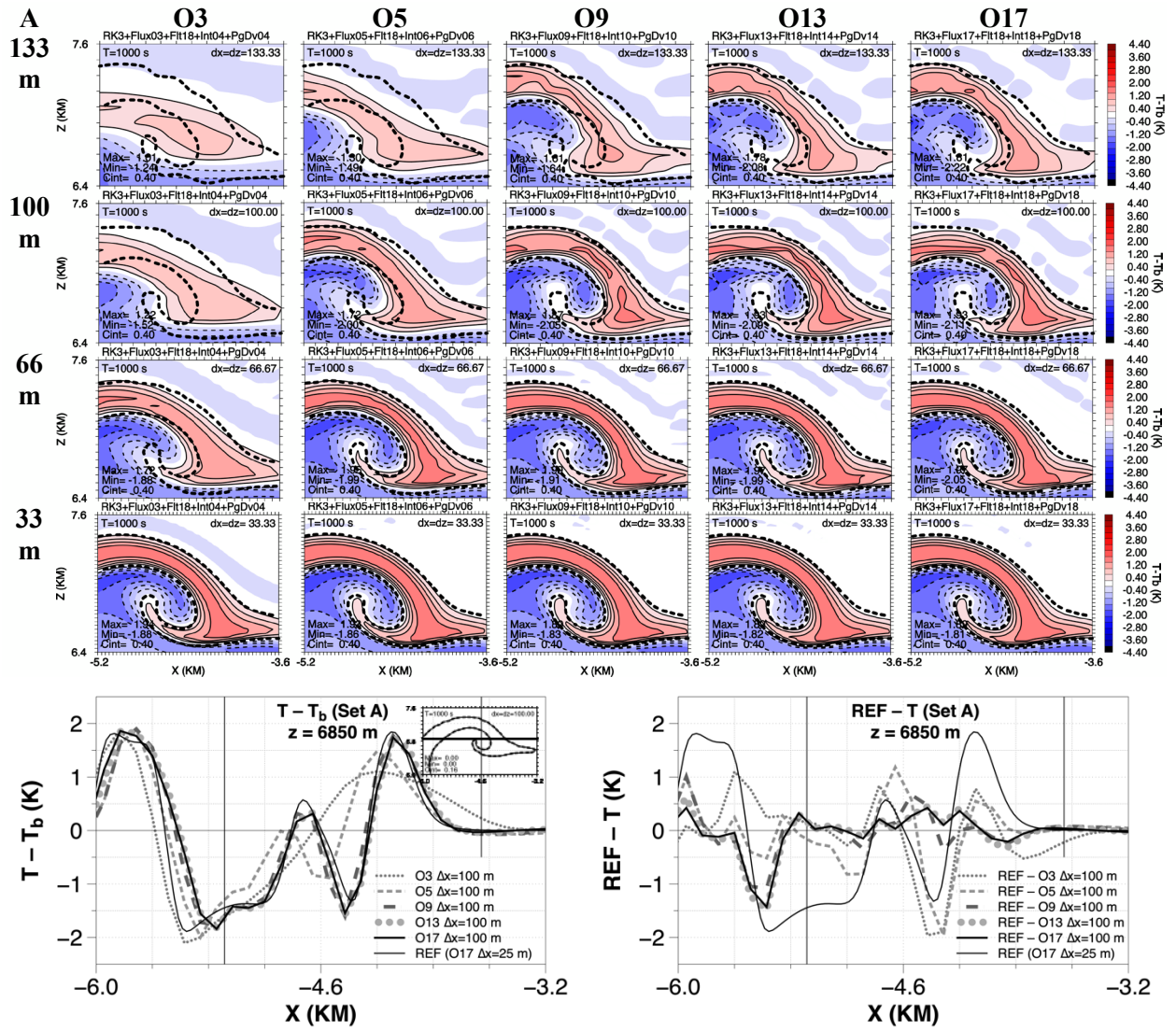FIGURE 4. Set A perturbation potential temperature ($T - T_b$; K) fields at $t = 1000$ s for simulations with odd order O3, 5, 9, 13, and 17 upwind-biased constant grid advective flux schemes, comparable order interpolations and pressure gradient / divergence, same O18 spatial filter, same

Courant number, and same constant eddy mixing coefficient of $K_m = 10$ m^2 s^{-1}. From top to bottom the resolutions are $\Delta x = \Delta z = 166.67, 133.33, 100, 66.67, 50, 33.33$, and 25 m. Maximum (Max), minimum (Min), and contour interval (Cint) values are on each plot. The bold dashed line is the 0.2 K perturbation potential temperature contour of the Set A O17, 25 m reference solution interpolated to each grid resolution. Only left side of sub-domain from $x = -6.7$ to -2.7 km and $z = 3.6$ to 7.6 km is shown.

FIGURE 5. Set A perturbation potential temperature ($T - T_b$; K) fields at $t = 1000$ s for simulations made with odd order O3, 5, 9, 13, and 17 upwind-biased constant grid advective flux schemes, comparable order interpolations and pressure gradient / divergence, same O18 spatial filter, same Courant number, and same constant eddy mixing coefficient of $K_m = 10$ m^2 s^{-1}. From top to bottom the resolutions are $\Delta x = \Delta z = 133.33$, 100, 66.67, and 33.33 m. Maximum (Max), minimum (Min), and contour interval (Cint) values are on each plot. The bold dashed line is the 0.2 K perturbation potential temperature contour of the Set A O17, 25 m reference solution interpolated to each grid resolution. Only a zoomed in sub-domain from $x = -5.2$ to -3.6 km and $z = 6.4$ to 7.6 km on the left side of the simulation domain is shown. Bottom row shows cross-sections of perturbation potential temperature (K; left) and differences from the reference (REF; O17, 25 m) solution (K; right) for $\Delta x = \Delta z = 100$ m solutions. Cross-sections for the various orders of accuracy (legend) are taken from $x = -6.0$ to -3.2 km across the span of the left rotor at $z = 6850$ m, indicated by the line on the inset subplot in the right-most column, with the REF perturbation potential temperature solution denoted by the thin solid black line. Vertical lines in the cross-section panels (bottom row) at $x = -5.2$ km and $x = -3.6$ km show the x-axis extent of the contour panels (rows one through

four). Notice the larger differences in the O3–5 solutions compared to the ≥O9 solutions, especially at intermediate and coarser resolutions.
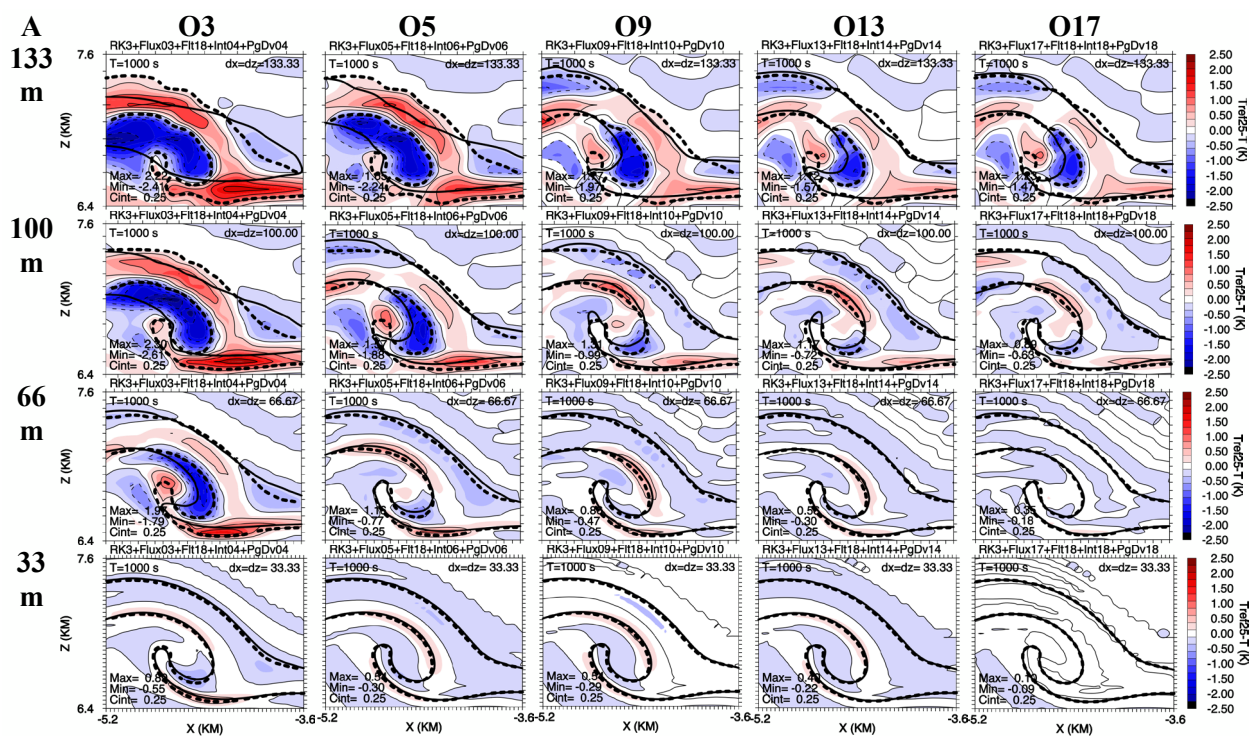
FIGURE 6. Set A perturbation potential temperature difference fields between the reference (Set A O17, 25 m) solution (T_{Ref}) and test solutions ($\Delta T_R = T_{Ref} - T$; K) at $t = 1000$ s for simulations made with odd order O3, 5, 9, 13, and 17 upwind-biased constant grid advective flux schemes, comparable order interpolations and pressure gradient / divergence, same O18 filter, same Courant number, and same constant eddy mixing coefficient of $K_m = 10$ m^2 s^{-1}. From top to bottom the resolutions are $\Delta x = \Delta z = 133.33$, 100, 66.67, and 33.33 m. Maximum (Max), minimum (Min), and contour interval (Cint) values are on each plot. The bold dashed line is the 0.2 K perturbation potential temperature contour of the Set A O17, 25 m reference solution interpolated to each grid resolution. The bold solid line is the 0.2 K perturbation potential temperature contour of the solution in the plot. Only a zoomed in sub-domain from $x = -5.2$ to -3.6 km and $z = 6.4$ to 7.6 km on the left side of the simulation domain is shown. Notice the larger differences in the O3–5 solutions compared to the $\geq$O9 solutions, especially at intermediate and coarser resolutions.

Suggestion for shorter caption:
FIGURE 6. As in Fig. 5, except for Set A perturbation potential temperature difference fields between the reference (Set A O17, 25 m) solution (T_{Ref}) and test solutions ($\Delta T_R = T_{Ref} - T$; K) and no cross-sections. The bold dashed line is the 0.2 K perturbation potential temperature contour of the Set A O17, 25 m reference solution interpolated to each grid resolution. Notice the larger differences in the O3–5 solutions compared to the $\geq$O9 solutions, especially at intermediate and coarser resolutions.
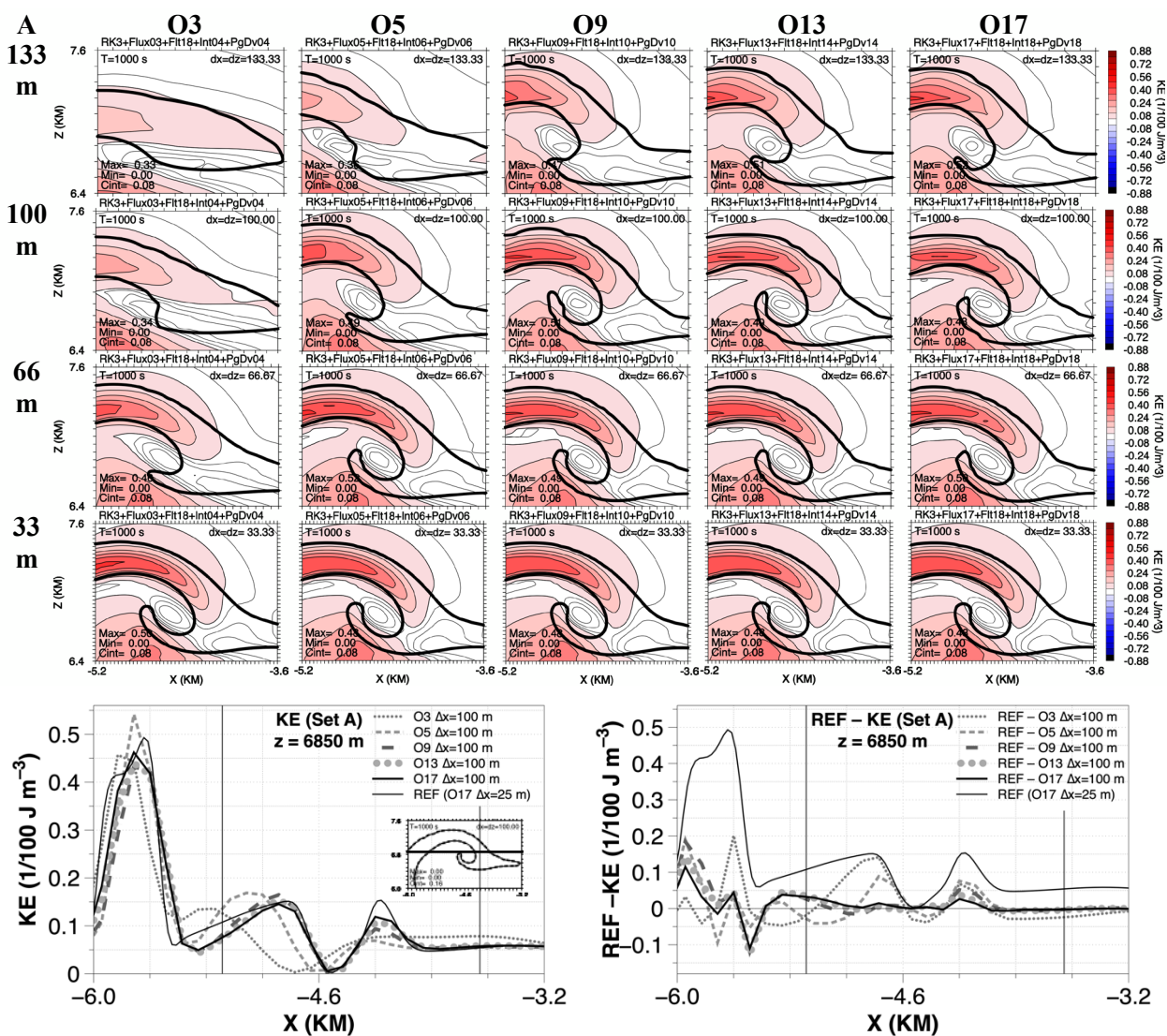
FIGURE 7. Set A Kinetic Energy per unit volume (KE; 1/100 J m^{-3}) fields at $t = 1000$ s for simulations made with odd order O3, 5, 9, 13, and 17 upwind-biased constant grid advective flux schemes, comparable order interpolations and pressure gradient / divergence, same O18 spatial filter, same Courant number, and same constant eddy mixing coefficient of $K_m = 10$ m^2 s^{-1}. From top to bottom the resolutions are $\Delta x = \Delta z =$ 133.33, 100, 66.67, and 33.33 m. Maximum (Max), minimum (Min), and contour interval (Cint) values are on each plot. The bold solid line is the 0.2 K perturbation potential temperature contour of the simulation in the plot. Only a zoomed in sub-domain from $x = -5.2$ to -3.6 km and $z = 6.4$ to 7.6 km on the left side of the simulation domain is shown. Bottom row shows cross-sections of KE (1/100 J m^{-3}; left) and differences from the reference (REF; O17, 25 m) solution (1/100 J m^{-3}; right) for $\Delta x = \Delta z = 100$ m solutions. Cross-sections for the various orders of accuracy (legend) are taken from $x = -6.0$ to -3.2 km across the span of the left rotor at $z = 6850$ m, indicated by the line on the inset subplot in the right-most column, with the REF KE solution denoted by the thin solid black line. Vertical lines in the cross-section panels (bottom row) at $x = -5.2$ km and $x = -3.6$ km show the x-axis extent of the contour

panels (rows one through four). Notice the larger, lesser, and least differences in the O3–5, O9, and O13–17 solutions, respectively, especially at intermediate and coarser resolutions.

Suggestion for shorter caption:
FIGURE 7. As in Fig. 5, except for Set A Kinetic Energy per unit volume (KE; $1/100$ J m^{-3}) fields. The bold contour is for the 0.2 K perturbation potential temperature contour of the simulation in the plot. Notice the larger, lesser, and least differences in the O3–5, O9, and O13–17 solutions, respectively.
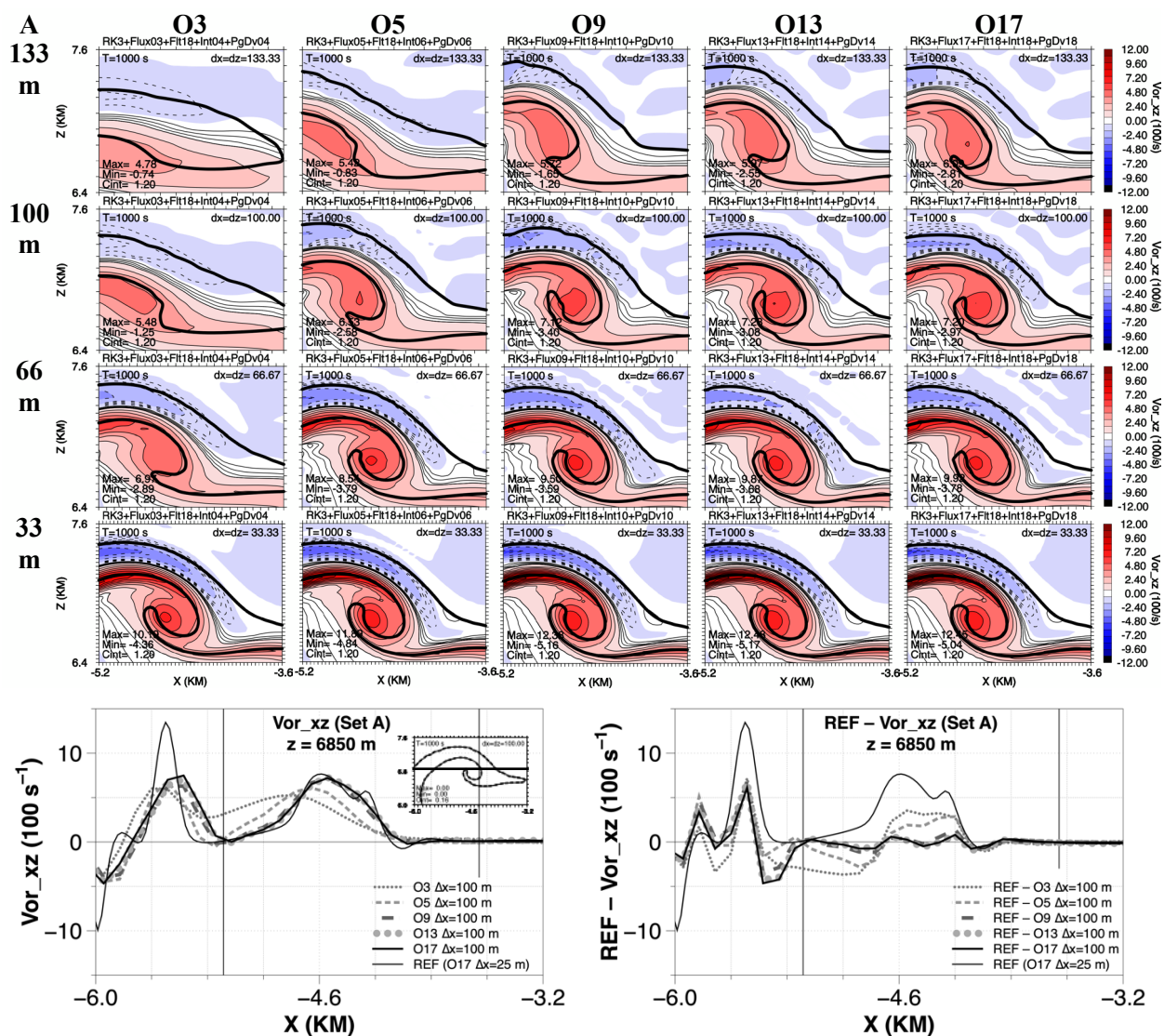
FIGURE 8. Set A Vorticity (Vor_xz; 100 s^{-1}) fields at t = 1000 s for simulations in Set A made with odd order O3, 5, 9, 13, and 17 upwind-biased constant grid advective flux schemes, comparable order interpolations and pressure gradient / divergence, same O18 spatial filter, same Courant number, and same constant eddy mixing coefficient of K_m = 10 m^2 s^{-1}. From top to bottom the resolutions are $\Delta x = \Delta z$ = 133.33, 100, 66.67, and 33.33 m. Maximum (Max), minimum (Min), and contour interval (Cint) values are on each plot. The bold solid line is the 0.2 K perturbation potential temperature contour of the simulation in the plot. Only a zoomed in sub-domain from x = −5.2 to −3.6 km and z = 6.4 to 7.6 km on the left side of the simulation domain is shown. Bottom row shows cross-sections of vorticity (Vor_xz; 100 s^{-1}; left) and differences from the reference (REF; O17, 25 m) solution (100 s^{-1}; right) for $\Delta x = \Delta z$ = 100 m solutions. Cross-sections for the various orders of accuracy (legend) are taken from x = −6.0 to −3.2 km across the span of the left rotor at z = 6850 m, indicated by the line on the inset subplot in the right-most column, with the REF vorticity solution denoted by the thin solid black line. Vertical lines in the cross-section panels (bottom row) at x = −5.2 km and x = −3.6 km show the x-axis extent of the contour panels (rows

one through four). Notice the larger differences in the O3–5 solutions compared to the ≥O9 solutions, especially at intermediate and coarser resolutions.
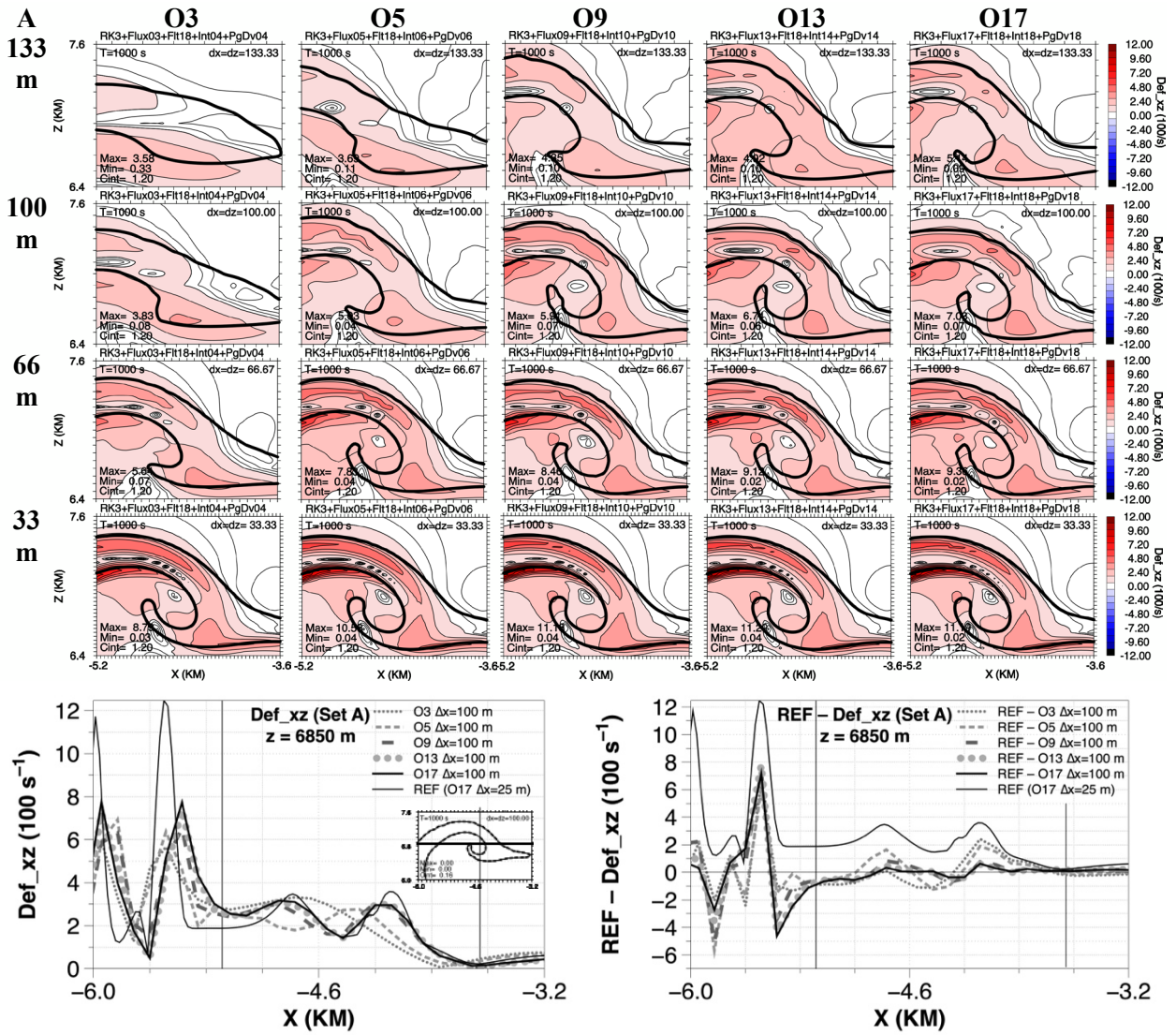

Suggestion for shorter caption:
FIGURE 8. As in Fig. 5, except for Set A Vorticity (Vor_xz; 100 s^{-1}) fields. The bold solid line is the 0.2 K perturbation potential temperature contour of the simulation in the plot. Notice the larger differences in the O3–5 solutions compared to the ≥O9 solutions, especially at intermediate and coarser resolutions.

FIGURE 9. Set A Deformation (Def_xz; 100 s^{-1}) fields at $t = 1000$ s for simulations in Set A made with odd order O3, 5, 9, 13, and 17 upwind-biased flux advection schemes, comparable order interpolations and pressure gradient / divergence, same O18 spatial filter, same Courant number, and same constant eddy mixing coefficient of $K_m = 10$ m^2 s^{-1}. From top to bottom the resolutions are $\Delta x = \Delta z = 133.33$, 100, 66.67, and 33.33 m. Maximum (Max), minimum (Min), and contour interval (Cint) values are on each plot. The bold solid line is the 0.2 K perturbation potential temperature contour of the simulation in the plot. Only a zoomed in sub-domain from $x = -5.2$ to -3.6 km and $z = 6.4$ to 7.6 km on the left side of the simulation domain is shown. Bottom row shows cross-sections of deformation (Def_xz; 100 s^{-1}; left) and differences from the reference (REF; O17, 25 m) solution (100 s^{-1}; right) for $\Delta x = \Delta z = 100$ m solutions. Cross-sections for the various orders of accuracy (legend) are taken from $x = -6.0$ to -3.2 km across the span of the left rotor at $z = 6850$ m, indicated by the line on the inset subplot in the right-most column, with the REF deformation solution denoted by the thin solid black line. Vertical lines in the cross-section panels (bottom row) at $x = -5.2$ km and $x = -3.6$ km show the x-axis extent of the contour panels

(rows one through four). Notice the larger differences in the O3–5 solutions compared to the ≥O9 solutions, especially at intermediate and coarser resolutions.

Suggestion for shorter caption:
FIGURE 9. As in Fig. 5, except for Set A Deformation (magnitude of deformation; Def_xz; 100 s^{-1}) fields. The bold solid line is the 0.2 K perturbation potential temperature contour of the simulation in the plot. Notice the larger differences in the O3–5 solutions compared to the ≥O9 solutions, especially at intermediate and coarser resolutions.
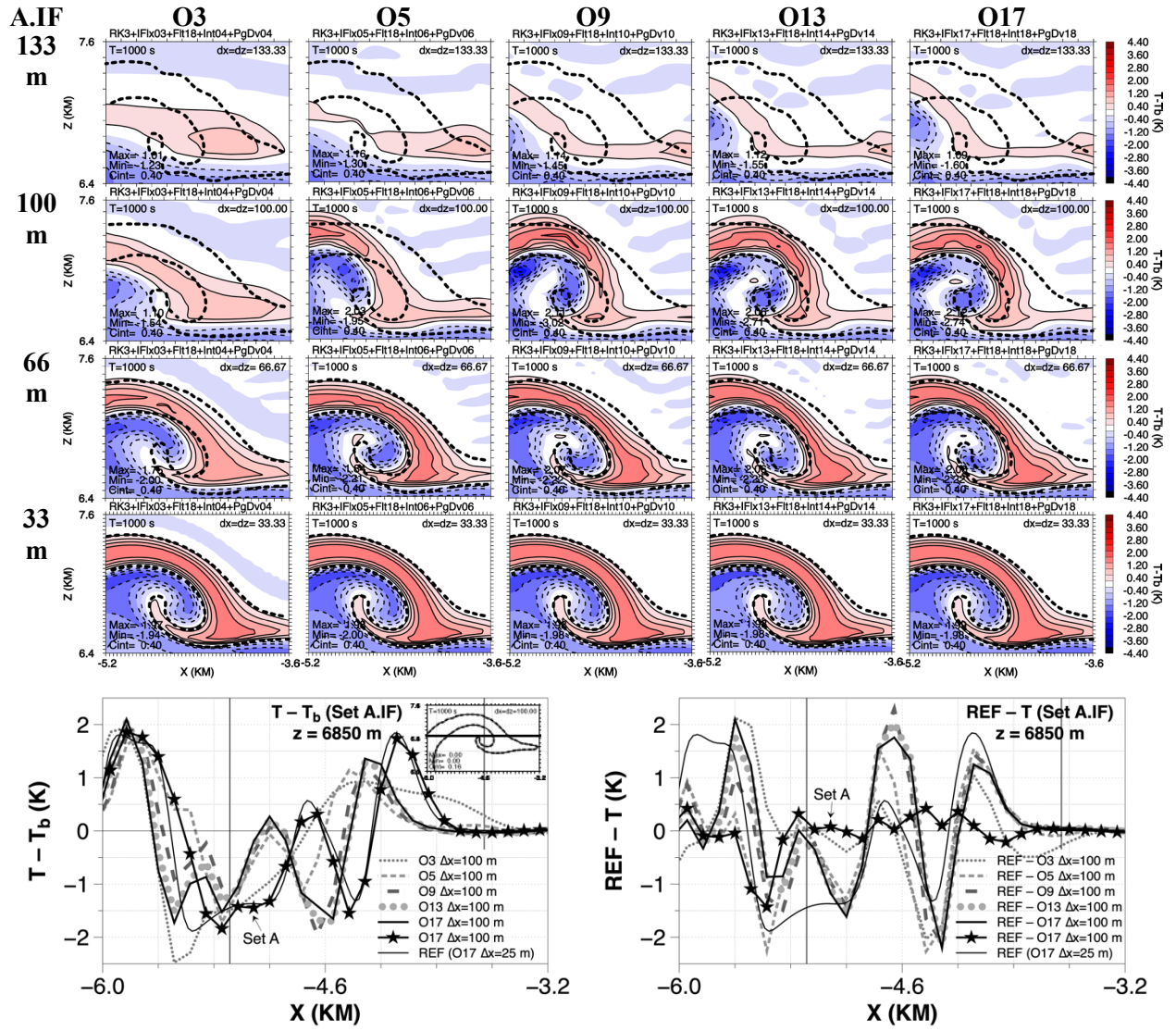
FIGURE 10. Set A.IF perturbation potential temperature ($T - T_b$; K) fields at t = 1000 s for simulations made with odd order O3, 5, 9, 13, and 17 upwind-biased integrated advective flux schemes, comparable order interpolations and pressure gradient / divergence, same O18 spatial filter, same Courant number, and same constant eddy mixing coefficient of K_m = 10 m² s⁻¹. From top to bottom the resolutions are $\Delta x = \Delta z$ = 133.33, 100, 66.67, and 33.33 m. Maximum (Max), minimum (Min), and contour interval (Cint) values are on each plot. The bold dashed line is the 0.2 K perturbation potential temperature contour of the Set A O17, 25 m reference solution interpolated to each grid resolution. Only a zoomed in sub-domain from x = −5.2 to −3.6 km and z = 6.4 to 7.6 km on the left side of the simulation domain is shown. Bottom row shows cross-sections of perturbation potential temperature (K; left) and differences from the reference (REF; O17, 25 m) solution (K; right) for $\Delta x = \Delta z$ = 100 m solutions. Cross-sections for the various orders of accuracy (legend) are taken from x = −6.0 to −3.2 km across the span of the left rotor at z = 6850 m, indicated by the line on the inset subplot in the right-most column, with the REF perturbation

potential temperature solution denoted by the thin solid black line. The Set A, O17, 100 m solution is indicated with bold stars. Vertical lines in the cross-section panels (bottom row) at $x = -5.2$ km and $x = -3.6$ km show the x-axis extent of the contour panels (rows one through four). Notice all solutions have substantial overshoots and undershoots, as well as more significant shape differences and larger perturbation potential temperature deviations in the maximums and minimums from the reference simulation as compared to constant grid advective flux solutions shown in Fig. 5.

Suggestion for shorter caption:
FIGURE 10. As in Fig. 5, except for Set A.IF (integrated advective flux instead of constant grid advective flux schemes) perturbation potential temperature ($T - T_b$; K) fields. The bold dashed line is the 0.2 K perturbation potential temperature contour of the Set A O17, 25 m reference solution interpolated to each grid resolution. Bottom row shows cross-sections of perturbation potential temperature (K; left) and differences from the reference (REF; O17, 25 m) solution (K; right) for $\Delta x = \Delta z = 100$ m solutions taken at $z = 6850$ m indicated by line in sub-plot in the right-most column, for the various orders (legend), with the REF perturbation potential temperature solution denoted by the thin solid black line and the Set A, O17, 100 m solution is indicated with bold stars. Notice all solutions have substantial overshoots and undershoots, as well as more significant shape differences and larger perturbation potential temperature deviations in the maximums and minimums from the reference simulation as compared to constant grid advective flux solutions shown in Fig. 5.
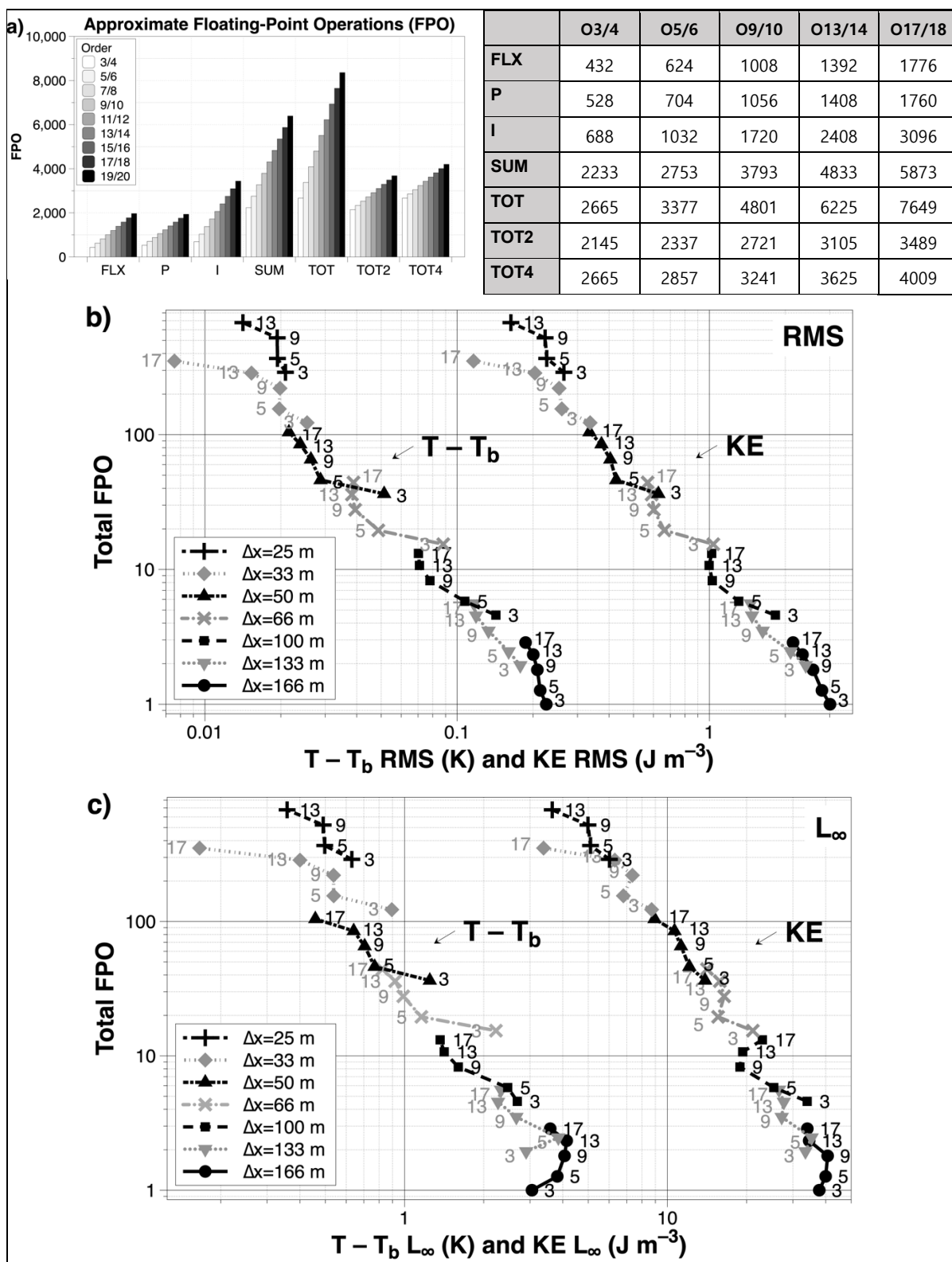
a) **Approximate Floating-Point Operations (FPO)**

	O3/4	O5/6	O9/10	O13/14	O17/18
FLX	432	624	1008	1392	1776
P	528	704	1056	1408	1760
I	688	1032	1720	2408	3096
SUM	2233	2753	3793	4833	5873
TOT	2665	3377	4801	6225	7649
TOT2	2145	2337	2721	3105	3489
TOT4	2665	2857	3241	3625	4009

FIGURE 11. Set A computational cost and errors. a) Approximate floating-point operations (FPO; a measure of computational cost) per grid point per time step for three stage RK3 time integration. The x-axis labels in a) and the row headings in the upper-right table are: FLX = O3, 5, 9, 13, and 17 odd order constant grid advective flux schemes; P = O4–18 pressure gradient / divergence terms; I = O4–18 interpolation; SUM = sum of P and I; TOT = O3, 5, 9, 13, and 17 FLX plus comparable order P and I; TOT2 = O3, 5, 9, 13, and 17 FLX; O2 P, and O2 I; and TOT4 = O3, 5, 9, 13, and 17 FLX, O4 P, and O4 I. (For example, the O3/4 in the legend of a) implies O3 FLX and O4 P and I.) b) and c) Log-log plots of the normalised approximate FPOs versus Root Mean Square (RMS) error for various grid resolutions and odd order flux schemes for $t = 1000$ s of simulation. Specifically, the total FPOs (for all grid points and for all time steps (i.e., the entire simulation) normalised by the total FPO value for the O3, $\Delta x = \Delta z = 166.67$ m simulation is plotted versus RMS errors calculated against the O17, 25 m reference solution for a) perturbation potential temperature ($T - T_b$; K; left cluster of curves) and Kinetic Energy per unit volume (KE; J m^{-3}; right cluster of curves), and in c) L$_\infty$ error norm for perturbation potential temperature ($T - T_b$; K; left cluster of curves) and L$_\infty$ error norm for KE (J m^{-3}; right cluster of curves).
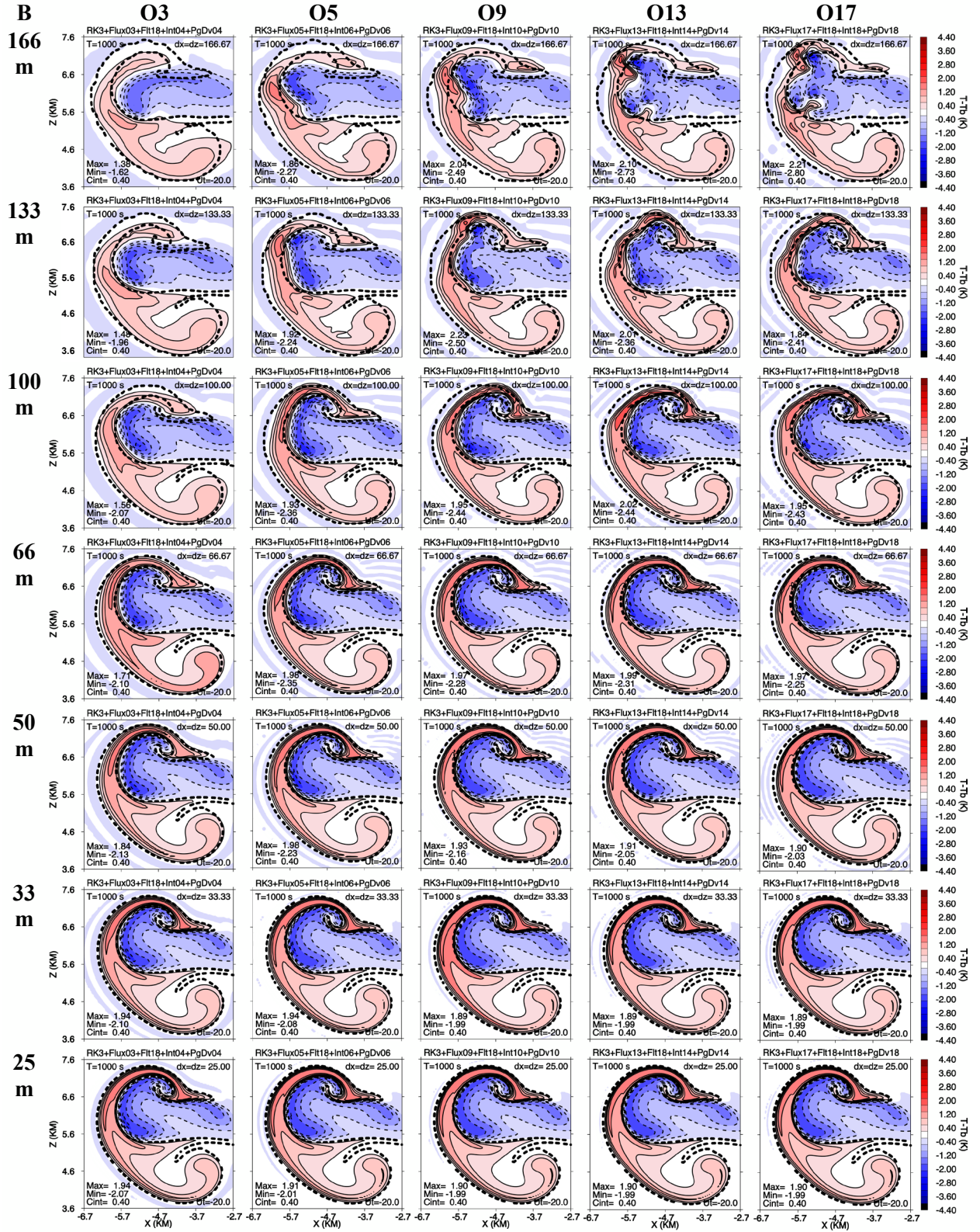
FIGURE 12. Set B perturbation potential temperature ($T - T_b$; K) fields at $t = 1000$ s for simulations made with an added mean wind of $U_t = -20$ m s^{-1}, odd order O3, 5, 9, 13, and 17 upwind-biased

constant grid advective flux schemes, comparable order interpolations and pressure gradient / divergence, same O18 spatial filter, same Courant number, and same constant eddy mixing coefficient of $K_m = 10$ m^2 s^{-1}. From top to bottom the resolutions are $\Delta x = \Delta z = 166.67$, 133.33, 100, 66.67, 50, 33.33, and 25 m. Maximum (Max), minimum (Min), and contour interval (Cint) values are on each plot. The bold dashed line is the 0.2 K perturbation potential temperature contour of the Set A O17, 25 m reference solution (with no wind; Set A) interpolated to each grid. Only left side of sub-domain from $x = -6.7$ to -2.7 km and $z = 3.6$ to 7.6 km is shown.

Suggestion for shorter caption:
FIGURE 12. As in Fig. 4, except for Set B (added mean wind of $U_t = -20$ m s^{-1}) perturbation potential temperature ($T - T_b$; K) fields. The bold dashed line is the 0.2 K perturbation potential temperature contour of the Set A O17, 25 m reference solution (with no wind; Set A) interpolated to each grid.
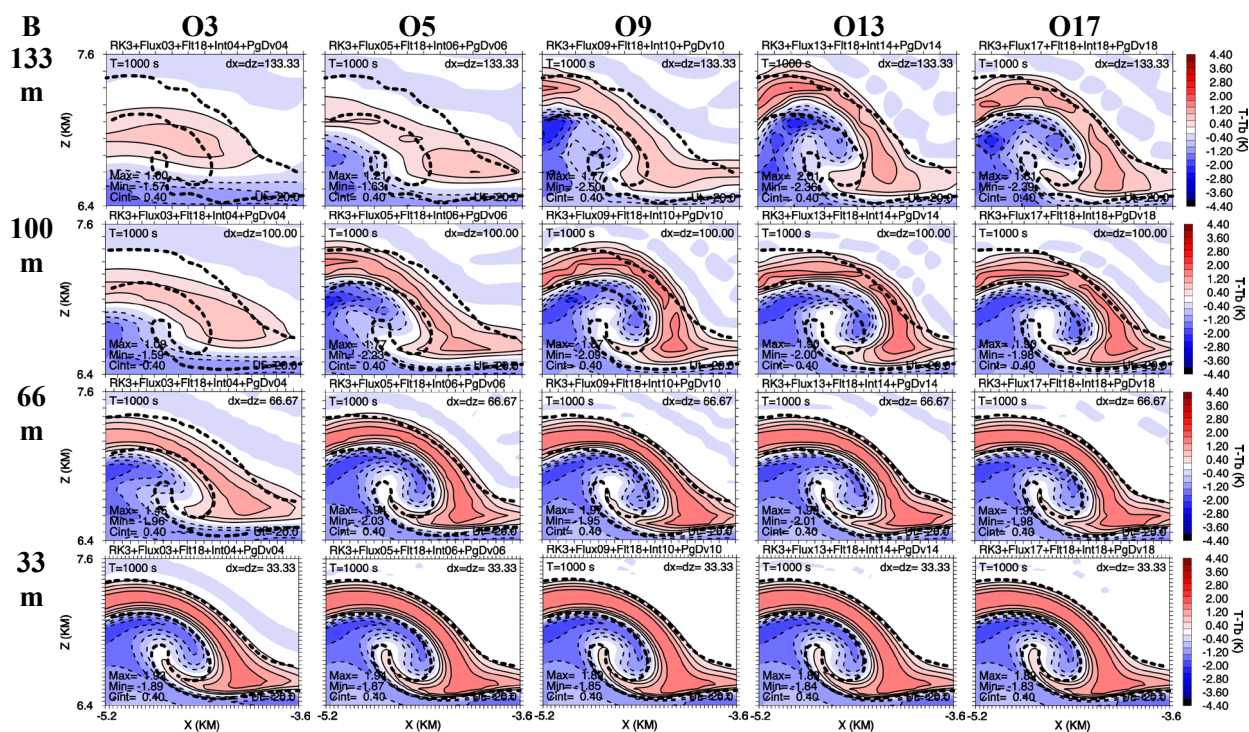
FIGURE 13. Set B perturbation potential temperature ($T - T_b$; K) fields at $t = 1000$ s for simulations made with an added mean wind of $U_t = -20$ m s^{-1}, odd order O3, 5, 9, 13, and 17 upwind-biased constant grid advective flux schemes, comparable order interpolations and pressure gradient / divergence, same O18 spatial filter, same Courant number, and same constant eddy mixing coefficient of $K_m = 10$ m^2 s^{-1}. From top to bottom the resolutions are $\Delta x = \Delta z = 133.33$, 100, 66.67, and 33.33 m. Maximum (Max), minimum (Min), and contour interval (Cint) values are on each plot. The bold dashed line is the 0.2 K perturbation potential temperature contour of the Set A O17, 25 m reference solution (with no wind; Set A) interpolated to each grid resolution. Only a zoomed in sub-domain from $x = -5.2$ to -3.6 km and $z = 6.4$ to 7.6 km on the left side of the simulation domain is shown.

Suggestion for shorter caption:
FIGURE 13. As in Fig. 5, except for Set B (added mean wind of $U_t = -20$ m s^{-1}) perturbation potential temperature ($T - T_b$; K) fields. There are no cross-sections. The bold dashed line is the 0.2 K perturbation potential temperature contour of the Set A O17, 25 m reference solution (with no wind; Set A) interpolated to each grid resolution.
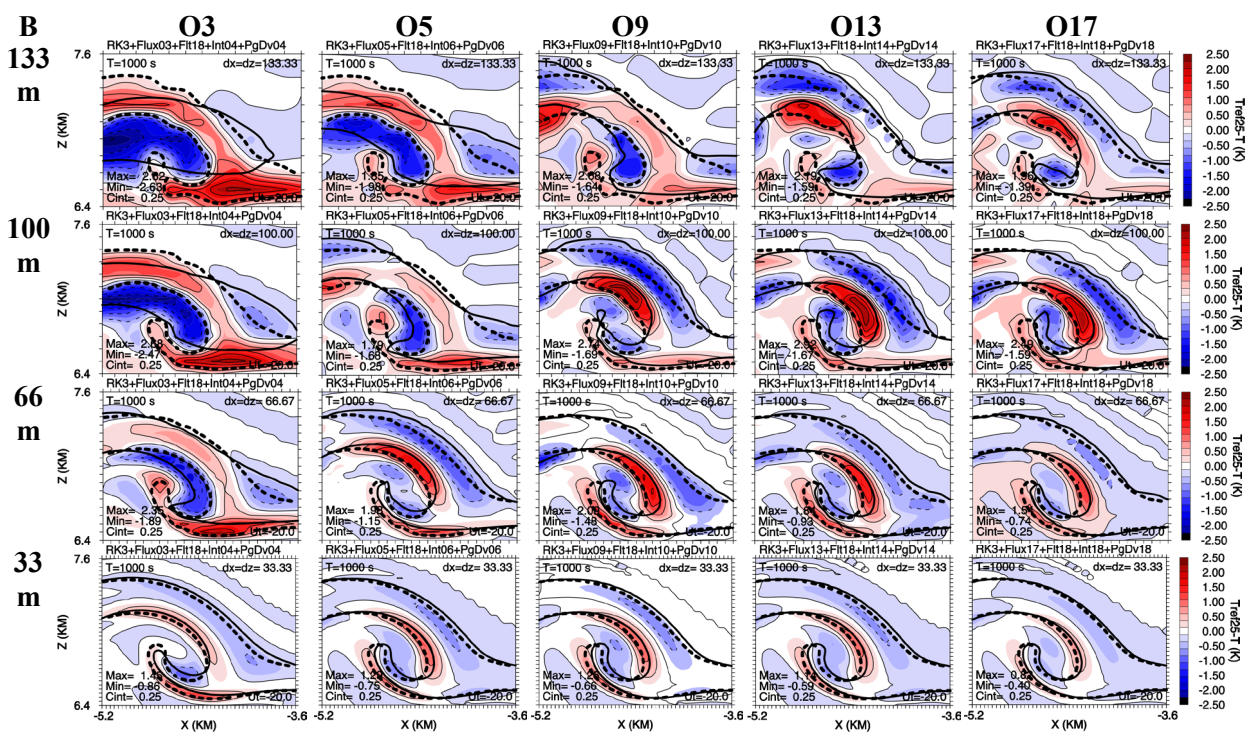
FIGURE 14. Set B (added mean wind of $U_t = -20$ m s^{-1}) perturbation potential temperature difference fields between the reference (Set B O17, 25 m) solution (T_{Ref}) and test solutions ($\Delta T_R = T_{Ref} - T$; K) at $t = 1000$ s for simulations made with odd order O3, 5, 9, 13, and 17 upwind-biased constant grid advective flux schemes, comparable order interpolations and pressure gradient / divergence, same O18 filter, same Courant number, and same constant eddy mixing coefficient of $K_m = 10$ m^2 s^{-1}. From top to bottom the resolutions are $\Delta x = \Delta z = 133.33$, 100, 66.67, and 33.33 m. Maximum (Max), minimum (Min), and contour interval (Cint) values are on each plot. The bold dashed line is the 0.2 K perturbation potential temperature contour of the Set A O17, 25 m reference solution interpolated to each grid resolution. The bold solid line is the 0.2 K perturbation potential temperature contour of the solution in the plot. Only a zoomed in sub-domain from $x = -5.2$ to -3.6 km and $z = 6.4$ to 7.6 km on the left side of the simulation domain is shown. Notice the larger differences, which show up as much larger positive and negative dipoles than those in Fig. 6, especially at intermediate and coarser resolutions and for lower orders of accuracy.

Suggestion for shorter caption:
FIGURE 14. As in Fig. 6, except for Set B (added mean wind of $U_t = -20$ m s^{-1}) perturbation potential temperature difference fields between the reference (Set A O17, 25 m) solution (T_{Ref}) and test solutions ($\Delta T_R = T_{Ref} - T$; K). There are no cross-sections. The bold dashed line is the 0.2 K perturbation potential temperature contour of the Set A O17, 25 m reference solution interpolated to each grid resolution. Notice the larger differences, which show up as much larger positive and negative dipoles than those in Fig. 6, especially at intermediate and coarser resolutions and for lower orders of accuracy.
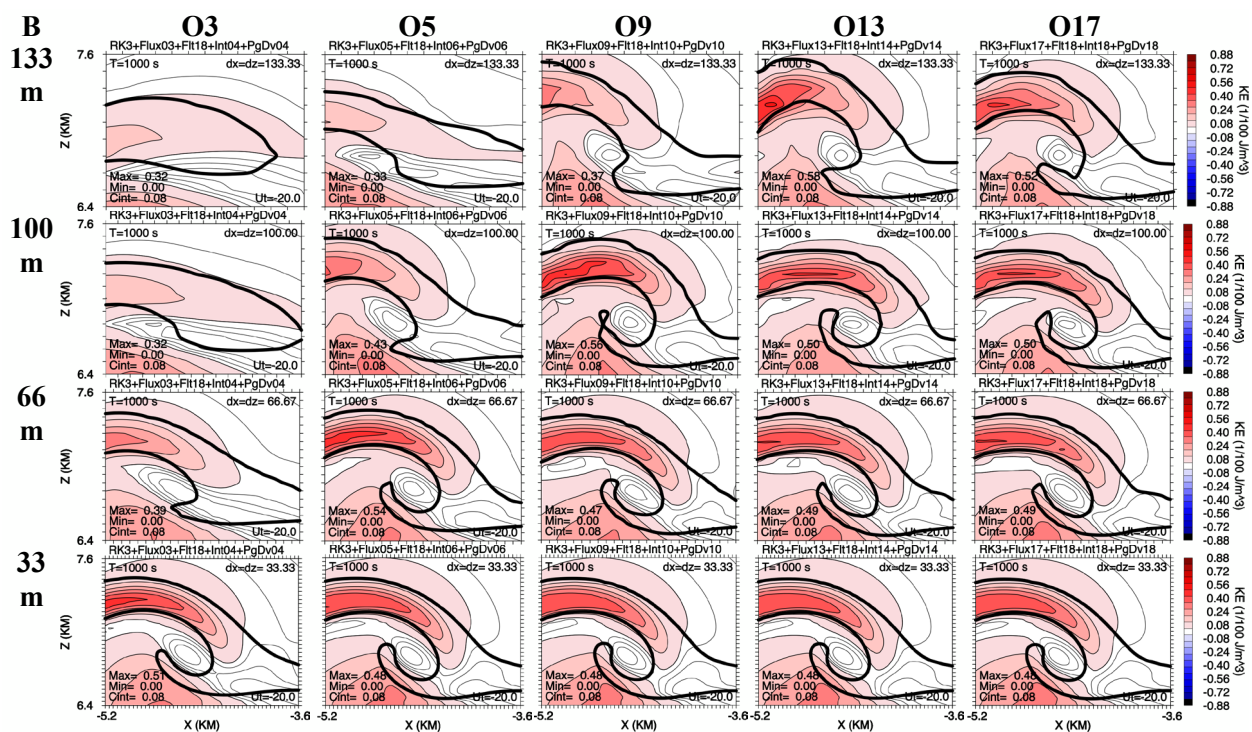
FIGURE 15. Set B (added mean wind of $U_t = -20$ m s^{-1}) Kinetic Energy per unit volume (KE; 1/100 J m^{-3}) fields at $t = 1000$ s for simulations made with odd order O3, 5, 9, 13, and 17 upwind-biased constant grid advective flux schemes, comparable order interpolations and pressure gradient / divergence, same O18 filter, same Courant number, and same constant eddy mixing coefficient of $K_m = 10$ m^2 s^{-1}. From top to bottom the resolutions are $\Delta x = \Delta z = 133.33$, 100, 66.67, and 33.33 m. Maximum (Max), minimum (Min), and contour interval (Cint) values are on each plot. The bold solid line is the 0.2 K perturbation potential temperature contour of the simulation in the plot. Only a zoomed in sub-domain from $x = -5.2$ to -3.6 km and $z = 6.4$ to 7.6 km on the left side of the simulation domain is shown.

Suggestion for shorter caption:
FIGURE 15. As in Fig. 7, except for Set B (added mean wind of $U_t = -20$ m s^{-1}) Kinetic Energy per unit volume (KE; 1/100 J m^{-3}) fields. There are no cross-sections. The bold solid line is the 0.2 K perturbation potential temperature contour of the simulation in the plot.
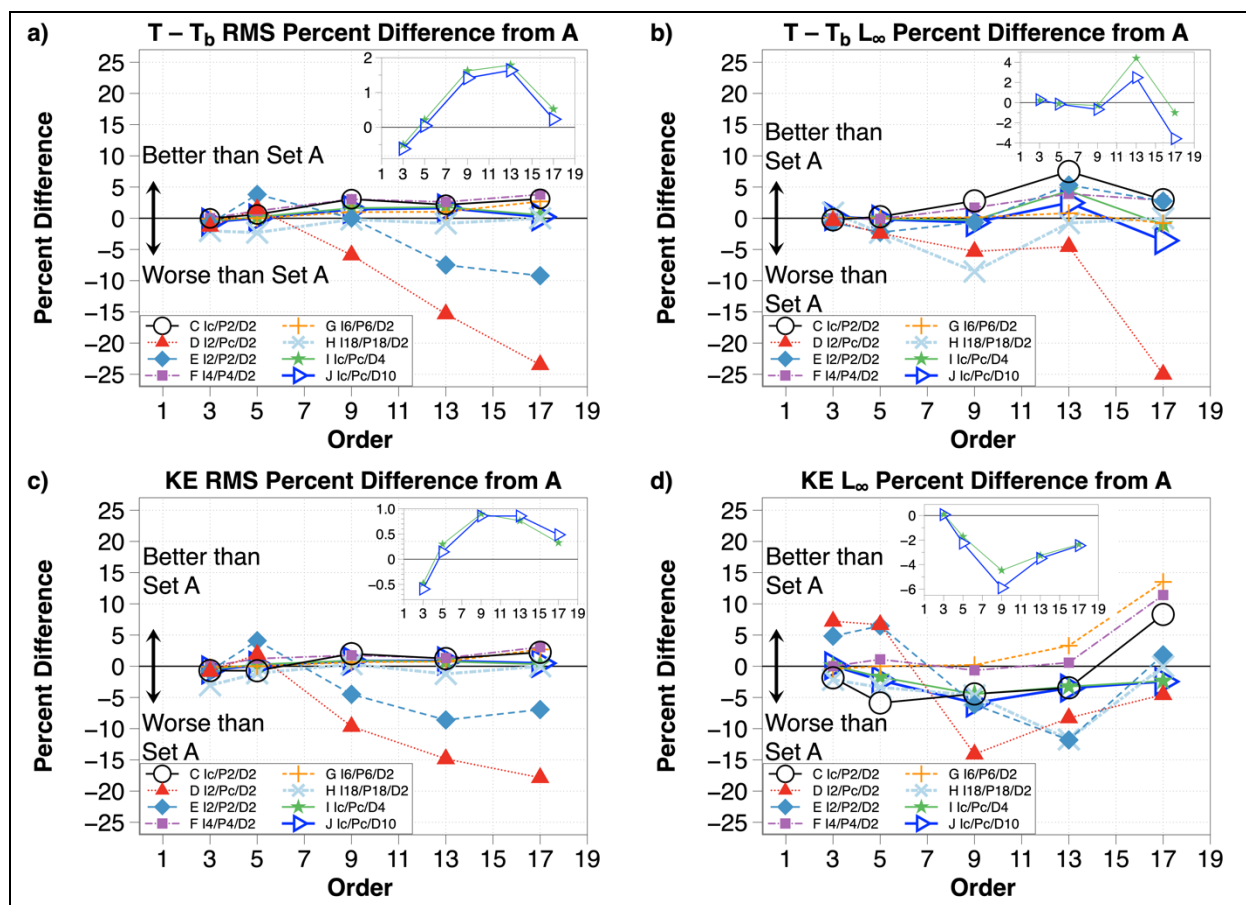
FIGURE 16. Sets C–J perturbation potential temperature ($T - T_b$; K; top) and Kinetic Energy per unit volume (KE; J m^{-3}; bottom) percent difference from Set A values [percent difference = (Set A value − test value) / Set A value • 100] of RMS error (left) and L$_\infty$ error norm (right) for test solutions with $\Delta x = \Delta z = 100$ m calculated against the O17, 25 m reference solution; values less (greater) than zero denote solutions that have larger (smaller) errors than Set A. Insets show enlarged solutions for Sets I and J for clarity. Experiment set orders of accuracy are shown in the legend (and also in Table II), where abbreviations are P = pressure gradient / divergence, I = interpolations, D = diffusion (subgrid-scale flux), and c = comparable order.
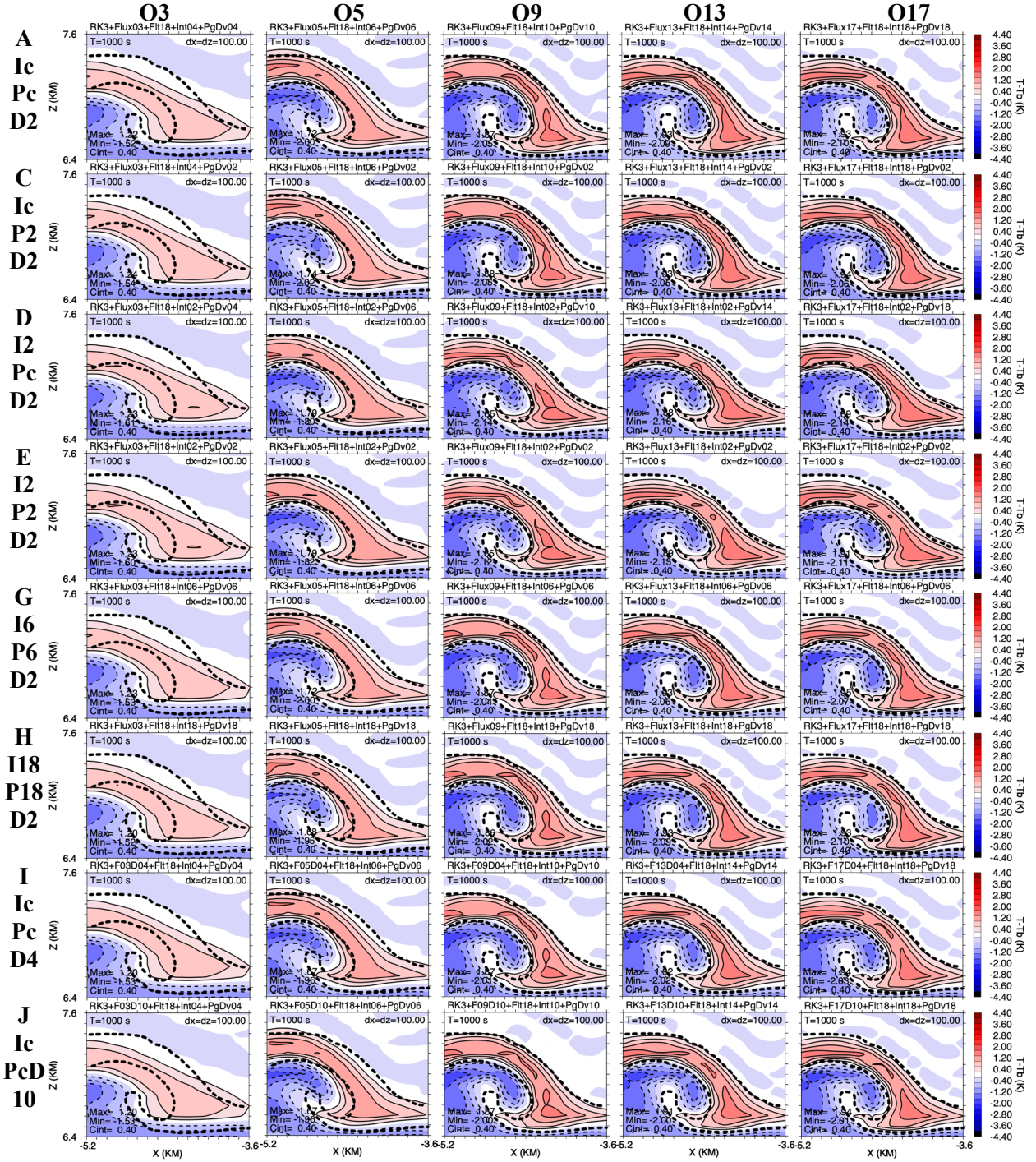
FIGURE 17. Sets A–J (without Sets A.IF, B, and F) perturbation potential temperature ($T - T_b$; K) fields at $t = 1000$ s using $\Delta x = \Delta z = 100$ m for simulations made with odd order O3, 5, 9, 13, and 17 upwind-biased constant grid advective flux schemes, comparable order interpolations and pressure gradient / divergence, same O18 spatial filter, same Courant number, and same constant eddy mixing coefficient of $K_m = 10$ m s^{-1}. Abbreviations are P = pressure gradient / divergence, I = interpolations, D = diffusion, and c = comparable order. (Experiment set orders of accuracy are defined in Table II.) Row one shows Set A (Ic/Pc/D2); row two is Set C (Ic/P2/D2); row three is

Set D (I2/Pc/D2); row four is Set E (I2/P2/D2); row five is Set G (I6/P6/D2); Row six is Set H (I18/P18/D2); row seven is Set I (Ic/Pc/D4); and bottom row is Set J (Ic/Pc/D10). Maximum (Max), minimum (Min), and contour interval (Cint) values are on each plot. The bold dashed line is the 0.2 K perturbation potential temperature contour of the Set A O17, 25 m reference solution interpolated to each grid resolution. Only a zoomed in sub-domain from $x = -5.2$ to -3.6 km and $z = 6.4$ to 7.6 km on the left side of the simulation domain is shown. Notice Sets D and E perform the least favorably, overall, compared to most Sets.
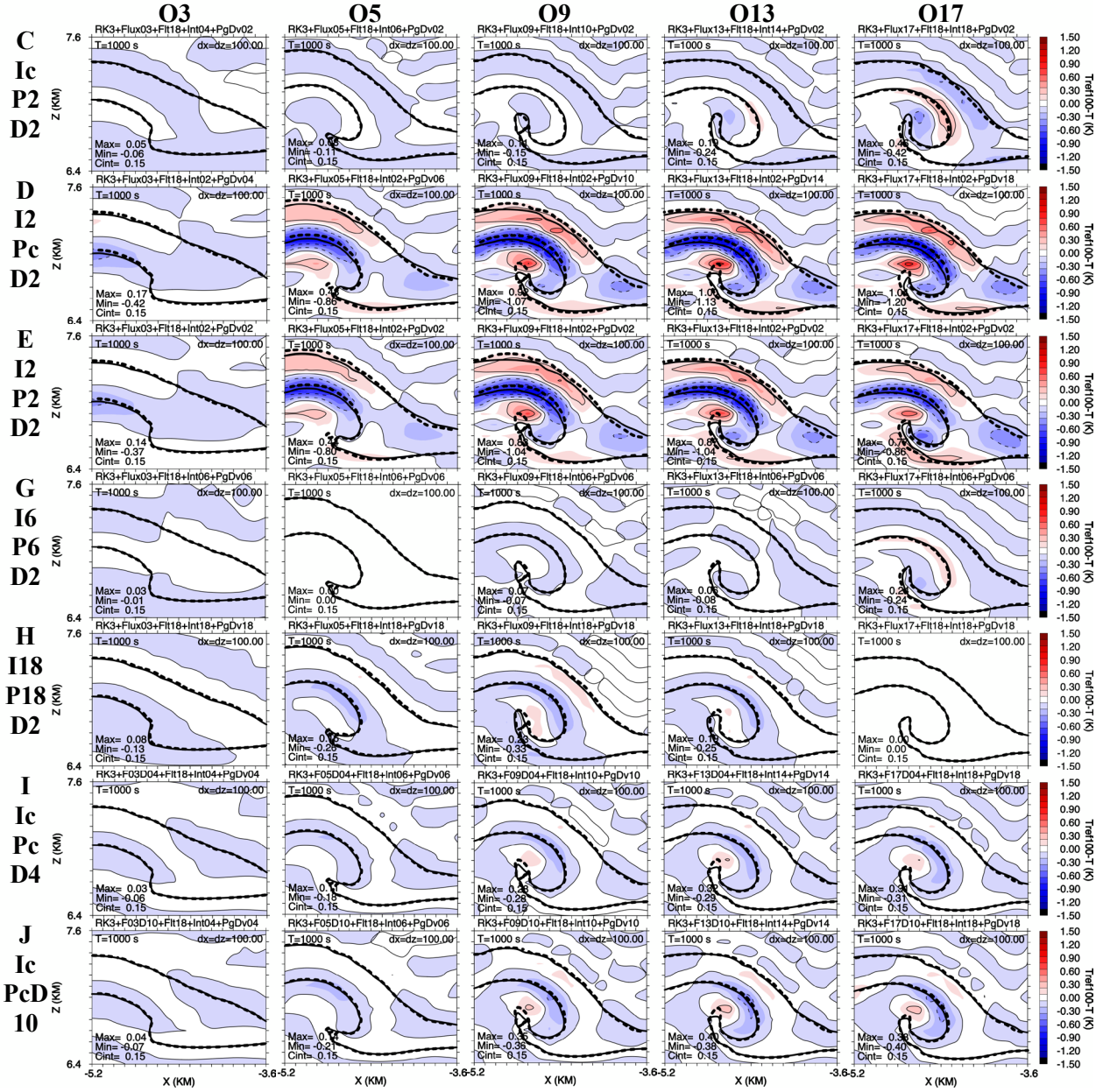
FIGURE 18. Sets C–J (without Sets A, A.IF, B, and F) perturbation potential temperature difference fields between the original (Set A) $\Delta x = \Delta z = 100$ m solution with same order of accuracy (T_{SetA}) and test solutions using $\Delta x = \Delta z = 100$ m ($\Delta T_A = T_{SetA} - T$; K) at $t = 1000$ s for simulations made with odd order O3, 5, 9, 13, and 17 upwind-biased constant grid advective flux schemes, comparable order interpolations and pressure gradient / divergence, same O18 spatial filter, same Courant number, and same constant eddy mixing coefficient of $K_m = 10$ m s^{-1}. Abbreviations are P = pressure gradient / divergence, I = interpolations, D = diffusion, and c = comparable order. (Experiment set orders of accuracy are defined in Table II.) Row one is Set C (Ic/P2/D2); row two is Set D (I2/Pc/D2); row three is Set E (I2/P2/D2); row four is Set G (I6/P6/and D2); Row five is Set H (I18/P18/D2); row six is Set I (Ic/Pc/D4); and bottom row is Set J (Ic/Pc/D10). Maximum (Max), minimum (Min), and contour interval (Cint) values are on

each plot. In this figure only, the bold dashed line is the 0.2 K perturbation potential temperature contour of the Set A 100 m solution with the same order of accuracy as the test solution. The bold solid line is the 0.2 K perturbation potential temperature contour of the simulation in the plot. Only a zoomed in sub-domain from $x = -5.2$ to -3.6 km and $z = 6.4$ to 7.6 km on the left side of the simulation domain is shown. Note that set G O5 and Set H O17 should have zero fields as shown. Notice Sets D and E perform the least favorably, overall, compared to most Sets.

Suggestion for shorter figure caption:

FIGURE 18. As in Fig. 17, except for Sets C–J (without Sets A, A.IF, B, and F) perturbation potential temperature difference fields between the original (Set A) $\Delta x = \Delta z = 100$ m solution with same order of accuracy (T_{SetA}) and test solutions using $\Delta x = \Delta z = 100$ m ($\Delta T_A = T_{SetA} - T$; K). In this figure only, the bold dashed line is the 0.2 K perturbation potential temperature contour of the Set A 100 m solution with the same order of accuracy as the test solution. The bold solid line is the 0.2 K perturbation potential temperature contour of the simulation in the plot. Notice Sets D and E perform the least favorably, overall, compared to most Sets.
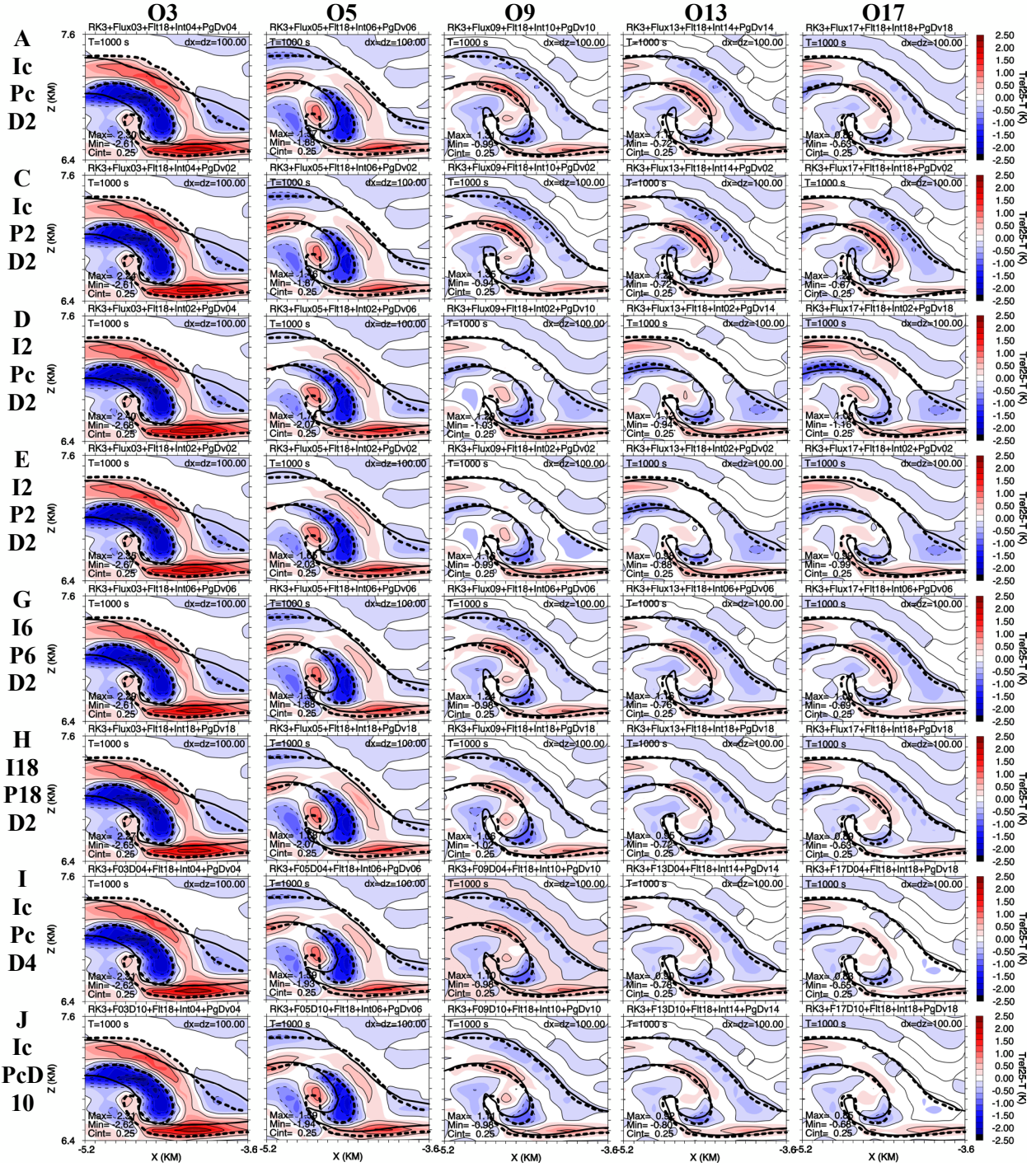
FIGURE 19. Sets A–J (without Sets A.IF, B, and F) difference fields between the reference and test perturbation potential temperatures ($\Delta T_R = T_{Ref} - T$; K) at $t = 1000$ s using $\Delta x = \Delta z = 100$ m for simulations made with odd order O3, 5, 9, 13, and 17 upwind-biased constant grid advective flux schemes, comparable order interpolations and pressure gradient / divergence, same O18 spatial filter, same Courant number, and same constant eddy mixing coefficient of $K_m = 10$ m s^{-1}. Abbreviations are P = pressure gradient / divergence, I = interpolations, D = diffusion, and c = comparable order. (Experiment set orders of accuracy are defined in Table II.) Row one shows Set

A (Ic/Pc/D2); row two is Set C (Ic/P2/D2); row three is Set D (I2/Pc/D2); row four is Set E (I2/P2/D2); row five is Set G (I6/P6/D2); Row six is Set H (I18/P18/D2); row seven is Set I (Ic/Pc/D4); and bottom row is Set J (Ic/Pc/D10). Maximum (Max), minimum (Min), and contour interval (Cint) values are on each plot. The bold dashed line is the 0.2 K perturbation potential temperature contour of the Set A O17, 25 m reference solution interpolated to each grid resolution. The bold solid line is the 0.2 K perturbation potential temperature contour of the simulation in the plot. Only a zoomed in sub-domain from $x = -5.2$ to -3.6 km and $z = 6.4$ to 7.6 km on the left side of the simulation domain is shown. Notice Sets D and E perform the least favorably, overall, compared to most Sets.

Suggestion for shorter figure caption:

FIGURE 19. As in Fig. 17, except for Sets A–J (without Sets A.IF, B, and F) difference fields between the reference and test perturbation potential temperatures ($\Delta T_R = T_{Ref} - T$; K). The bold dashed line is the 0.2 K perturbation potential temperature contour of the Set A O17, 25 m reference solution interpolated to each grid resolution. The bold solid line is the 0.2 K perturbation potential temperature contour of the simulation in the plot. Notice Sets D and E perform the least favorably, overall, compared to most Sets.
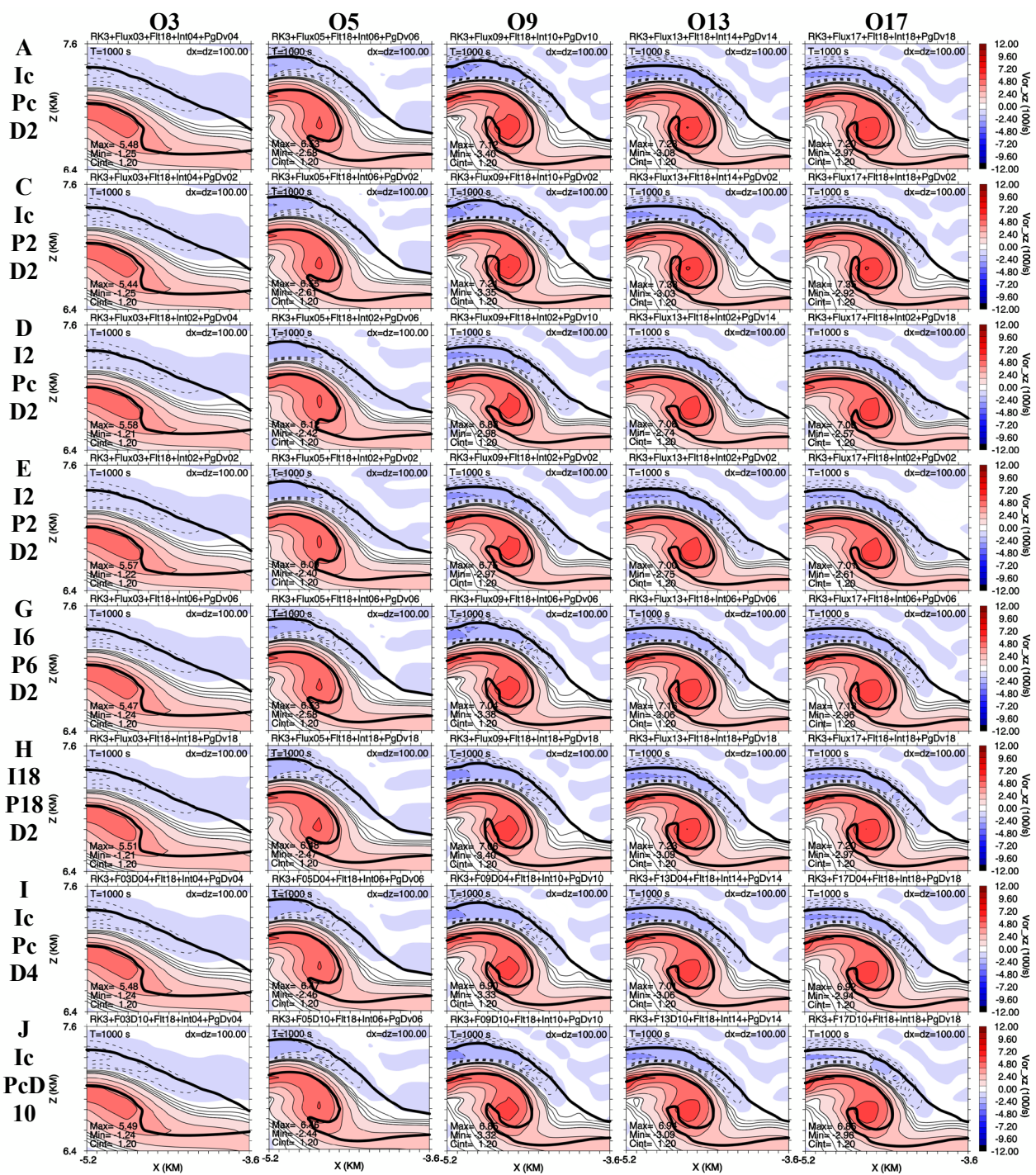
FIGURE 20. Sets A–J (without Sets A.IF, B, and F) Vorticity (Vor_xz; 100 s^{-1}) fields at $t = 1000$ s using $\Delta x = \Delta z = 100$ m for simulations made with odd order O3, 5, 9, 13, and 17 upwind-biased constant grid advective flux schemes, comparable order interpolations and pressure gradient / divergence, same O18 spatial filter, same Courant number, and same constant eddy mixing coefficient of $K_m = 10$ m s^{-1}. Abbreviations are P = pressure gradient / divergence, I = interpolations, D = diffusion, and c = comparable order. (Experiment set orders of accuracy are defined in Table II.) Row one shows Set A (Ic/Pc/D2); row two is Set C (Ic/P2/D2); row three is

Set D (I2/Pc/D2); row four is Set E (I2/P2/D2); row five is Set G (I6/P6/and D2); Row six is Set H (I18/P18/D2); row seven is Set I (Ic/Pc/D4); and bottom row is Set J (Ic/Pc/D10). Maximum (Max), minimum (Min), and contour interval (Cint) values are on each plot. The bold solid line is the 0.2 K perturbation potential temperature contour of the simulation in the plot. Only a zoomed in sub-domain from $x = -5.2$ to -3.6 km and $z = 6.4$ to 7.6 km on the left side of the simulation domain is shown. Notice Sets D and E perform the least favorably, overall, compared to most Sets.

Suggestion for shorter figure caption:
FIGURE 20. As in Fig. 17, except for Sets C–J (without Sets A.IF, B, and F) Vorticity (Vor_xz; 100 s^{-1}) fields. The bold solid line is the 0.2 K perturbation potential temperature contour of the simulation in the plot. Notice Sets D and E perform the least favorably, overall, compared to most Sets.
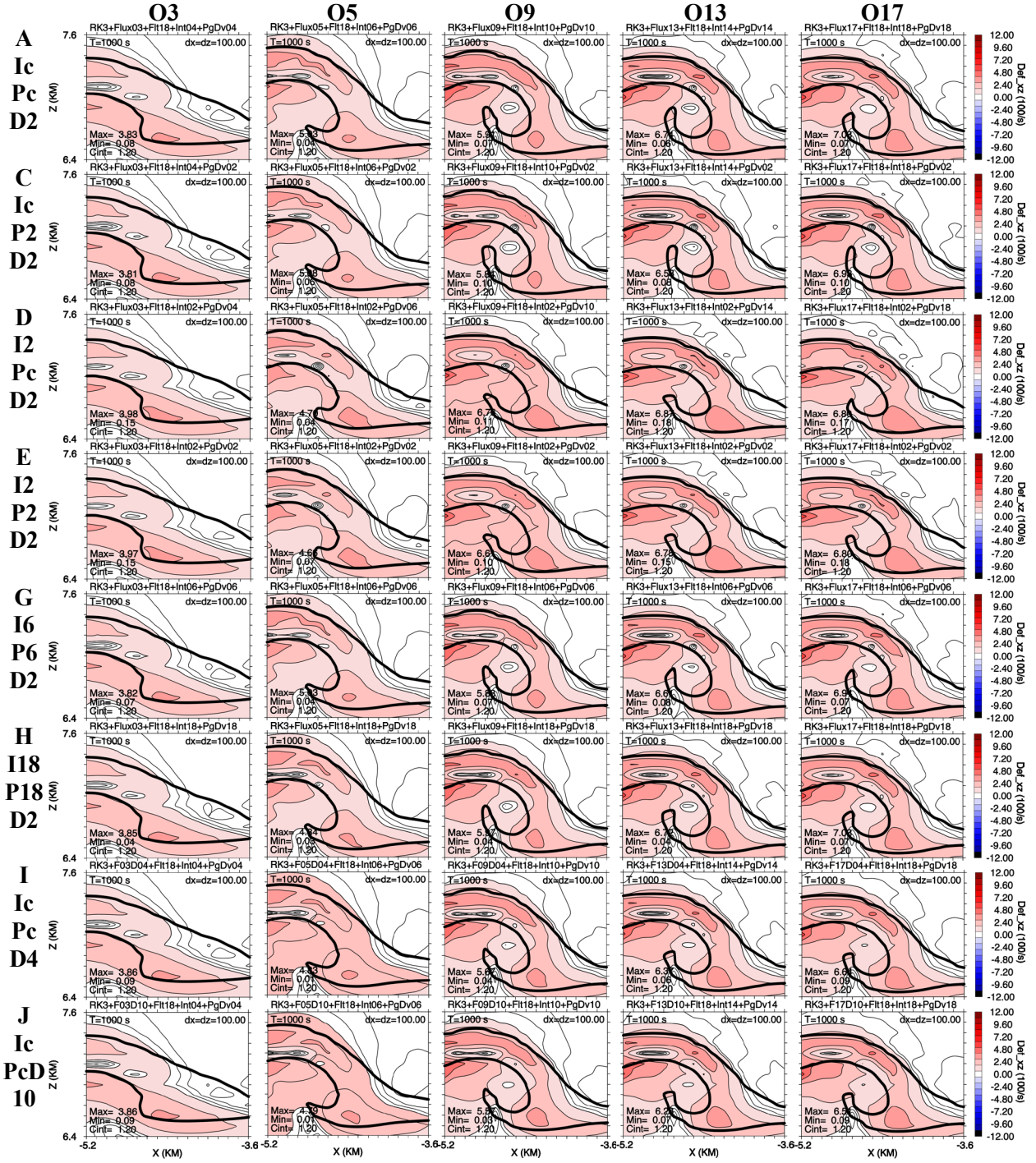
FIGURE 21. Sets A–J (without Sets A.IF, B, and F) Deformation (Def_xz; 100 s^{-1}) fields at $t =$ 1000 s using $\Delta x = \Delta z = 100$ m for simulations made with odd order O3, 5, 9, 13, and 17 upwind-biased constant grid advective flux schemes, comparable order interpolations and pressure gradient / divergence, same O18 spatial filter, same Courant number, and same constant eddy mixing coefficient of $K_m = 10$ m s^{-1}. Abbreviations are P = pressure gradient / divergence, I = interpolations, D = diffusion, and c = comparable order. (Experiment set orders of accuracy are defined in Table II.) Row one shows Set A (Ic/Pc/D2); row two is Set C (Ic/P2/D2); row three is

Set D (I2/Pc/D2); row four is Set E (I2/P2/D2); row five is Set G (I6/P6/and D2); Row six is Set H (I18/P18/D2); row seven is Set I (Ic/Pc/D4); and bottom row is Set J (Ic/Pc/D10). Maximum (Max), minimum (Min), and contour interval (Cint) values are on each plot. The bold solid line is the 0.2 K perturbation potential temperature contour of the simulation in the plot. Only a zoomed in sub-domain from x = –5.2 to –3.6 km and z = 6.4 to 7.6 km on the left side of the simulation domain is shown. Notice Sets D and E perform the least favorably, overall, compared to most Sets.

Suggestion for shorter figure caption:
FIGURE 21. As in Fig. 17, except for Sets A–J (without Sets A.IF, B and F) Deformation (Def_xz; 100 s^{-1}) fields. The bold solid line is the 0.2 K perturbation potential temperature contour of the simulation in the plot. Notice Sets D and E perform the least favorably, overall, compared to most Sets.

TABLE I. Domain and time step parameters. N_x (N_z) is equal to the number of scalar grid points in x- (z-) directions for a staggered grid. The total number of grid points = $N_x \cdot N_z$, and N_t is the number of time steps for 1000 s of integration. The x-direction velocity (u) has one extra point in the x-direction, and the z-direction velocity (w) has one extra point in the z-direction for the staggered C-grid. The time steps for each resolution are found using $\Delta t = C \cdot \Delta x / V_{max}$ (s), where Courant number $C = 0.046875$, values of Δx are grid resolutions, and approximate maximum velocity $V_{max} = 15$ m s^{-1}.

Δx (m)	Δz (m)	Lx (m)	Lz (m)	N_x	N_z	$N_x \cdot N_z$	N_t	Δt (s)
200.00	200.00	20000	10000	101	51	5151	1600	0.625
166.66…	166.66…	20000	10000	121	61	7381	1920	0.520833…
133.33…	133.33…	20000	10000	151	76	11476	2400	0.4166…
100.00	100.00	20000	10000	201	101	20301	3200	0.3125
66.66…	66.66…	20000	10000	301	151	45451	4800	0.20833…
50.00	50.00	20000	10000	401	201	80601	6400	0.15625
33.33…	33.33…	20000	10000	601	301	180901	9600	0.104166…
25	25	20000	10000	801	401	321201	12800	0.078125

TABLE II. Orders of accuracy for all odd order upwind-biased constant grid advective flux (FLX; Sets A–J) and integrated advective flux (IFLX; Set A.IF). Abbreviations are P = pressure gradient / divergence, I = interpolations, D = diffusion (all O2 for Sets A–H and O4 and O10 for Set I and J, respectively), SF = spatial filter (all O18 for Sets A–J and Set A.IF), and c = comparable order. Note U_t is the added wind, which is $U_t = 0$ m s^{-1} for all experiments, except Set B which has $U_t = -20$ m s^{-1}. The meaning of Oc is comparable order (one order higher than used for odd order advective flux); for example, in Set A, O3 fluxes are coupled with comparable order (next order higher) O4 interpolations, O4 pressure gradient / divergence, O18 spatial filter, and O2 subgrid-scale (SGS) turbulent fluxes.

Sets	Expt. Name	$\Delta x = \Delta z$ (m)	FLX (IFLX)	I / P / D	SF
A	Ic / Pc / D2	25, 33.33…, 50, 66.66…, 100, 133.33…, 166.66…, 200	O3,5,9,13,17	Oc/Oc/O2	O18
A.IF	Integrated flux Ic / Pc / D2	25, 33.33…, 50, 66.66…, 100, 133.33…, 166.66…, 200	O3,5,9,13,17	Oc/Oc/O2	O18
B	Set A with mean wind $U_t = -20$ m s^{-1}	25, 33.33…, 50, 66.66…, 100, 133.33…, 166.66…, 200	O3,5,9,13,17	Oc/Oc/O2	O18
C	Ic / P2 / D2	100	O3,5,9,13,17	Oc/O2/O2	O18
D	I2 / Pc / D2	100	O3,5,9,13,17	O2/Oc/O2	O18
E	I2 / P2 / D2	100	O3,5,9,13,17	O2/O2/O2	O18
F	I4 / P4 / D2	100	O3,5,9,13,17	O4/O4/O2	O18
G	I6 / P6 / D2	100	O3,5,9,13,17	O6/O6/O2	O18
H	I18 / P18 / D2	100	O3,5,9,13,17	O18/O18/O2	O18
I	Ic / Pc / D4	100	O3,5,9,13,17	Oc/Oc/O4	O18
J	Ic / Pc / D10	100	O3,5,9,13,17	Oc/Oc/O10	O18